

# UNIVERSITÀ DEGLI STUDI DI PADOVA

Dipartimento di Fisica e Astronomia “Galileo Galilei”  
Master Degree in Astrophysics and Cosmology

## Final dissertation

### Investigating Deuterium Destruction in BBN with Felsenkeller Accelerator

Thesis supervisor  
**Prof. Dr. Antonio Caciolli**  
Thesis co-supervisor  
**Dr. Eliana Masha**

Candidate  
**Aravind Remesan Sreekala**

Academic Year 2022/23

# Contents

<b>Contents</b>	<b>i</b>
<b>List of Figures</b>	<b>iii</b>
<b>List of Tables</b>	<b>v</b>
<b>Abstract</b>	<b>vi</b>
<b>Introduction</b>	<b>vii</b>
<b>1 Nuclear Astrophysics</b>	<b>1</b>
1.1 Thermonuclear Reaction Rate . . . . .	1
1.1.1 Non-resonant reactions induced by charged particles . . . . .	4
<b>2 Big Bang Nucleosynthesis</b>	<b>9</b>
2.1 Standard Model . . . . .	9
2.2 Primordial Nucleosynthesis . . . . .	13
2.3 Baryon-to-photon ratio, $\eta$ . . . . .	18
2.4 Primordial D/H . . . . .	19
2.5 $^2\text{H}(\text{p}, \gamma)^3\text{He}$ - State of the art . . . . .	21
2.6 Physical Motivation for this Work . . . . .	24
<b>3 <math>^2\text{H}(\text{p}, \gamma)^3\text{He}</math> at Felsenkeller</b>	<b>26</b>
3.1 Felsenkeller Laboratory . . . . .	26
3.2 Experimental Setup . . . . .	27
<b>4 Data Analysis</b>	<b>31</b>
4.1 Efficiency Calibration . . . . .	31
4.1.1 $^{137}\text{Cs}$ . . . . .	31
4.1.2 $^{60}\text{Co}$ . . . . .	32
4.1.3 $^{22}\text{Na}$ . . . . .	33
4.1.4 $^{88}\text{Y}$ . . . . .	33
4.1.5 $^{27}\text{Al}(\text{p}, \gamma)^{28}\text{Si}$ . . . . .	34
4.1.6 Net Counts from $\gamma$ spectra . . . . .	34

4.1.7	Multi-Parametric Approach . . . . .	35
4.1.8	Efficiency Calibration Results . . . . .	37
4.1.9	Doppler and Recoil Correction . . . . .	42
4.2	Target Analysis . . . . .	42
4.3	S Factor . . . . .	44
4.3.1	Calculation of Net Area . . . . .	44
4.3.2	Yield of $^2\text{H}(\text{p}, \gamma)^3\text{He}$ . . . . .	44
4.3.3	Angular Correction of Yield . . . . .	49
4.3.4	Calculation of S Factor . . . . .	50
<b>5</b>	<b>Results and Discussion</b>	<b>56</b>
5.1	Efficiency . . . . .	56
5.2	Angular Distribution of Yield . . . . .	57
5.3	S Factor . . . . .	57
5.3.1	Comparison with LUNA and HZDR . . . . .	58
	<b>Conclusions</b>	<b>64</b>
	<b>References</b>	<b>65</b>

# List of Figures

1.1	Maxwell Boltzmann Distribution of nuclei in stellar plasma. . . . .	3
1.2	Schematic of the tunnelling of Coulomb barrier[3]. . . . .	4
1.3	Tunnelling Probability v Energy. . . . .	5
1.4	Cross-section for charged particle induced reactions. Top panel: Cross-section reduces rapidly at low energy, making extrapolation difficult. Bottom panel: The astrophysical S-factor on the other hand varies smoothly with energy and hence an extrapolation to lower energies is possible [1]. . . . .	6
1.5	The Gamow peak: A convolution between Maxwell Boltzmann distribution of energies and tunnelling probability through the Coulomb barrier[4]. . . . .	7
2.1	The time-temperature evolution of the neutron-to-proton ( $n/p$ ) ratio. The solid red curve indicates the true variation. The steep decline at a few hundred seconds is the result of the onset of BBN. The dashed blue curve indicates the equilibrium $n/p$ ratio $e^{-\frac{\Delta m}{T}}$ , and the dotted grey curve indicates free-neutron decay $e^{-\frac{t}{\tau_n}}$ [14]. . . . .	15
2.2	Photon and neutrino temperatures during the $e^\pm$ annihilation[17]. . . . .	16
2.3	Big Bang Nucleosynthesis nuclear reaction chain. . . . .	17
2.4	Mass fraction of nuclei as a function of time and temperature during the BBN. . . . .	18
2.5	$^4\text{He}$ , $^2\text{H}$ , $^3\text{He}$ and $^7\text{Li}$ abundances plotted against the baryon-to-photon ratio. The yellow regions represent the observed abundances. Primordial deuterium abundance observed closely agrees with BBN theory, while primordial $^3\text{He}$ has not been observed [20]. $^7\text{Li}$ on the other hand is observed at a much lower abundance, which is the famous cosmological lithium problem[21]. . . . .	20
2.6	LUNA result (red points and red line)[39] for S-Factor for $^2\text{H}(p, \gamma)^3\text{He}$ in comparison with previous measurements. . . . .	24
2.7	S-factor fit of $^2\text{H}(p, \gamma)^3\text{He}$ reported in Turkat et al[40] in comparison with previous studies. . . . .	25
3.1	$\gamma$ -background on the Earth's surface, at Felsenkeller and LUNA in Gran Sasso. . . . .	27
3.2	Overview of the Felsenkeller laboratory in Dresden, Germany. . . . .	28
3.3	Detector Setup (View from Top). . . . .	29
3.4	Part of the experimental setup can be seen. . . . .	30
4.1	Decay level scheme of $^{137}\text{Cs}$ . . . . .	32
4.2	Decay level scheme of $^{60}\text{Co}$ . . . . .	32

4.3	Decay level scheme of $^{22}\text{Na}$ . . . . .	33
4.4	Decay level scheme of $^{88}\text{Y}$ . . . . .	33
4.5	$\gamma$ -peaks for $^{137}\text{Cs}$ and $^{60}\text{Co}$ in EB18G ( $90^\circ$ ) detector. . . . .	35
4.6	$\gamma$ -peaks for $^{22}\text{Na}$ and $^{88}\text{Y}$ in EB18G ( $90^\circ$ ) detector. . . . .	35
4.7	$^{27}\text{Al}(\text{p}, \gamma)^{28}\text{Si}$ peaks obtained in the EB18G ( $90^\circ$ ) detector. . . . .	36
4.8	Experimental yield and residuals for EB18G ( $90^\circ$ ) detector. See details in the text (section 4.1.8). . . . .	38
4.9	Efficiency curve for EB18G ( $90^\circ$ ) detector. . . . .	39
4.10	Efficiency curve for Can60 ( $89^\circ$ ) detector. . . . .	39
4.11	Efficiency curve for MB13 ( $118^\circ$ ) detector. . . . .	40
4.12	Efficiency curve for MB23 ( $36^\circ$ ) detector. . . . .	40
4.13	Efficiency curve for Ron100 ( $143.5^\circ$ ) detector. . . . .	41
4.14	Efficiency curve for EB17G ( $39^\circ$ ) detector. . . . .	41
4.15	Schematic diagram of the ERDA geometry. . . . .	43
4.16	Depth profiles extracted from the measurements. . . . .	43
4.17	Two zoom in the region of interest for the gamma spectrum acquired at 800 keV with the EB18G ( $90^\circ$ ) detector. The region of interest is shown delimited in panel (b) and the fluorine peaks are underlined in panel (a). . . . .	45
4.18	Yield for EB18G detector at $90^\circ$ . . . . .	46
4.19	Yield for Can60 detector at $89^\circ$ . . . . .	46
4.20	Yield for Ron100 detector at $143.5^\circ$ . . . . .	47
4.21	Yield for MB13 detector at $118^\circ$ . . . . .	47
4.22	Yield for MB23 detector at $36^\circ$ . . . . .	48
4.23	Yield for EB17G detector at $39^\circ$ . . . . .	48
4.24	Variation of $\sigma(E)$ w.r.t. the energy. . . . .	51
4.25	S Factor for EB18G detector at $90^\circ$ . Uncertainty of 1 to 3.5% for the energy range. .	52
4.26	S Factor for Can60 detector at $89^\circ$ . Uncertainty of 2 to 3.5% for the energy range. .	53
4.27	S Factor for Ron100 detector at $143.5^\circ$ . Uncertainty of 3 to 4% for the energy range. .	53
4.28	S Factor for MB13 detector at $118^\circ$ . Uncertainty of 3 to 5% for the energy range. .	54
4.29	S Factor for MB23 detector at $36^\circ$ . Uncertainty of 3 to 5% for the energy range. .	54
4.30	S Factor for EB17G detector at $39^\circ$ . Uncertainty of 3 to 7.5% for the energy range.	55
5.1	Summary of efficiency plots for all detectors. . . . .	56
5.2	Angular distribution of yield at 608 keV. . . . .	57
5.3	Summary of S Factors for all detectors. . . . .	58
5.4	S Factor obtained for EB18G ( $90^\circ$ ) detector in comparison to LUNA and HZDR data and fit. . . . .	59
5.5	S Factor obtained for Can60 ( $89^\circ$ ) detector in comparison to LUNA and HZDR data and fit. . . . .	60
5.6	S Factor obtained for Ron100 ( $143.5^\circ$ ) detector in comparison to LUNA and HZDR data and fit. . . . .	61
5.7	S Factor obtained for MB13 ( $118^\circ$ ) detector in comparison to LUNA and HZDR data and fit. . . . .	62

# List of Tables

3.1	Detector positions at Felsenkeller.	30
4.1	Radioactive Sources for Calibration.	31
4.2	Major $\gamma$ -peaks of $^{27}\text{Al}(\text{p}, \gamma)^{28}\text{Si}$ [43].	34
4.3	Summing corrections for all detectors for $^{60}\text{Co}$ and $^{22}\text{Na}$ .	38
4.4	Expected $\gamma$ -peaks for the different detectors in units of keV.	42
4.5	Depth Profile of and Deuterium thickness of LNL_125_1a.	44
4.6	Coefficients for Legendre Polynomials $a_i$ .	49
4.7	Angular Correction factor $W(\theta)$ for all energies for each detector.	50
4.8	Astrophysical S Factor all energies for each detector. Uncertainties are also shown (systematic + statistical).	52
5.1	EB18G detector ( $90^\circ$ ): S factor and discrepancy with LUNA and HZDR S factor fits.	59
5.2	Can60 detector ( $89^\circ$ ): S factor and discrepancy with LUNA and HZDR S factor fits.	60
5.3	Ron100 detector ( $143.5^\circ$ ): S factor and discrepancy with LUNA and HZDR S factor fits.	61
5.4	MB13 detector ( $118^\circ$ ): S factor and discrepancy with LUNA and HZDR S factor fits.	62

# Abstract

The Big Bang Nucleosynthesis (BBN) began as the universe cooled below 0.1 MeV, about 3 seconds after the Big Bang, creating the first light elements in the universe. The primordial deuterium formed in this process is highly sensitive to the baryon density of the early universe and is therefore an excellent indicator of the same. Direct observations of the Cosmic Microwave Background (CMB) by PLANCK have constrained the baryon density at high precision ( $< 1\%$ ). The observations of primordial clouds provide an independent approach to constrain the cosmological parameters, but this requires accurate knowledge about the reaction rates affecting the primordial deuterium abundance.

In this thesis, the focus is on the  $^2\text{H}(\text{p},\gamma)^3\text{He}$  reaction which is the dominant reaction that destroys the primordial deuterium. Previous studies of the reaction by the LUNA collaboration at LNGS in the BBN energy range (30 to 260 keV) found the S factor at high precision ( $\approx 1\%$ ). A follow-up experiment at HZDR in the higher energy range (265 to 1094 keV) found a 10% discrepancy with the LUNA S factor fit. The new  $^2\text{H}(\text{p},\gamma)^3\text{He}$  campaign described in this thesis aims to confirm the findings of LUNA as well as the constrain the existing tension in the S factor between these two previous measurements using an independent setup.

The experiment is performed in the energy range 300 to 800 keV (lab energy) using a proton beam, solid deuterated targets and a High Purity Germanium (HPGe) detector setup. The photons produced in the reaction ( $Q = 5.493$  MeV) are measured by the HPGe detectors, which are placed at different angles around the target chamber to facilitate a study of the angular distribution of the cross-section as well.

In this thesis, all the steps performed for the measurement of the preliminary S factor for the  $^2\text{H}(\text{p},\gamma)^3\text{He}$  reaction are described, starting from the detector characterization, target analysis and finally the analysis of the  $^2\text{H}(\text{p},\gamma)^3\text{He}$  spectra to arrive at the S factor of the reaction. The preliminary results are shown, in comparison with the LUNA and HZDR measurements and the angular distribution is also discussed.

Keywords: BBN, CMB, S factor, Felsenkeller

# Introduction

The Big Bang Theory is one of the pillars of the standard model of cosmology, explaining the origin and evolution of the universe. The Big Bang theory proposes that approximately 13.8 billion years ago, the universe began as an extremely hot, dense and infinitely small singularity where all matter and energy were concentrated. In the fraction of a second that followed, the universe expanded rapidly from a point thereby creating the forces and particles that govern the cosmos. This rapid expansion is called cosmic inflation, which set the stage for forming the cosmic structures observed today.

All the structures observable today are made up of protons and neutrons in different nuclear configurations. The origin of these elements has been a question of many theoretical and experimental studies. One of the great successes of the standard model of cosmology, or the  $\Lambda$ CDM model is in its ability to explain the creation of the light elements through primordial nucleosynthesis. This process, which occurred in the first few minutes of the Big Bang, created all the Hydrogen and Helium in the universe.

This thesis focuses on the study of the  $^2\text{H}(\text{p}, \gamma)^3\text{He}$  reaction, which plays a pivotal role in Big Bang Nucleosynthesis (BBN) as it is one of the main processes through which deuterium is destroyed in the early universe, thereby altering its primordial abundance. Deuterium is the first nuclei formed in the universe which marked the beginning of the BBN reaction network. The primordial abundance of deuterium is an important parameter as it is highly sensitive to the baryon density of the universe  $\Omega_b h^2$ , as well as the number of neutrino species  $N_{\nu, \text{eff}}$ . Therefore, an accurate measurement of the primordial deuterium content will enable these cosmological parameters to be strongly constrained.

In this study, the  $^2\text{H}(\text{p}, \gamma)^3\text{He}$  reaction is studied in the energy range of 300 to 800 keV (in lab frame). This thesis is divided into five chapters: The first chapter will introduce the basic concepts of thermonuclear reactions in stars and focus specifically on charged particle-induced reactions.

In the second chapter, a summary of the evolution of the early universe leading up to the BBN, in the framework of the standard model will be discussed. The astrophysical relevance of the  $^2\text{H}(\text{p}, \gamma)^3\text{He}$  reaction will be detailed as well as the existing state of the art of the reaction.

The third chapter is focused on the experimental setup for the  $^2\text{H}(\text{p}, \gamma)^3\text{He}$  reaction at the Felsenkeller accelerator. In the fourth chapter, the data analysis is described in detail including the detector and target characterization as well as the steps followed in the analysis of the  $\gamma$  spectra of the  $^2\text{H}(\text{p}, \gamma)^3\text{He}$  reaction to obtain the S factor of the reaction.

The fifth and final chapter discusses the relevant results obtained and the comparison with the literature data.

# Chapter 1

## Nuclear Astrophysics

Nuclear astrophysics is a branch of astrophysics devoted to understanding the behaviour of atomic nuclei and their interactions inside stars and other celestial objects. It aims to provide an explanation for the mechanisms underlying nuclear reactions, element synthesis, and energy production in a variety of astrophysical settings, from the star's core to the explosions of supernovae.

In this chapter, an overview of the basic concepts of nuclear reactions with particular emphasis on thermonuclear reactions in stars, is shown.

### 1.1 Thermonuclear Reaction Rate

Thermonuclear reactions are the sources of energy production in stars as well as the nucleosynthesis of elements. The most important parameters determining the elements' abundance and energy production are the Q value and the reaction rates [1].

Most of the reactions happening in stars are two body problems which can be described as  $A + x \rightarrow B + y$ , where A is the target nucleus, x the projectile and B and y the products. The energy conservation for these types of reactions is given by 1.1:

$$m_A c^2 + m_x c^2 + E_x + E_A = m_B c^2 + m_y c^2 + E_B + E_y \quad (1.1)$$

where m is the rest mass and E is the kinetic energy for each particle. We can now define the Q - value as

$$Q = m_A c^2 + m_x c^2 - m_B c^2 - m_y c^2 = E_x + E_A - E_B - E_y \quad (1.2)$$

If  $Q > 0$ , the reaction is exothermic and Q represents the net energy production. Conversely, if  $Q < 0$ , the reaction is endothermic and Q represents the addition of energy needed for the reaction to occur.

While the Q value can be easily measured for all reactions, calculating the probability for a nuclear reaction to occur is not as straightforward.

For each target nucleus, we can associate a geometrical area that relates to the probability that the projectile interacts with the nucleus. This area is the cross-section  $\sigma$  of the nuclear reaction. In classical physics, this area can be written as the total geometrical area of the target nucleus and

the projectile,  $\sigma = \pi(R_t + R_p)^2$ , where  $R_t$  and  $R_p$  are the radii [2] of the target and the projectile respectively. This dependence on energy leads to a velocity dependence of the cross-section,  $\sigma = \sigma(v)$ . If we have 2 species A and B, of number density  $N_A$  and  $N_B$  and relative velocity  $v$ , the reaction rate is given by:

$$r = v\sigma(v)N_AN_B \quad (1.3)$$

The nuclei can have a wide range of velocities with a probability distribution  $\phi(v)$ . From equation 1.3,

$$r = N_AN_B \int_0^\infty v\sigma(v)\phi(v)dv = N_AN_B \langle \sigma v \rangle \quad (1.4)$$

In a non-degenerate and non-relativistic stellar plasma, the probability distribution of velocity is given by Maxwell-Boltzmann distribution (1.5)

$$\phi(v) = 4\pi v^2 \left( \frac{m}{2\pi k_B T} \right)^{\frac{3}{2}} e^{-\frac{mv^2}{2k_B T}} \quad (1.5)$$

where T is the temperature of the plasma, m is the mass of the nucleus and  $k_B$  is the Boltzmann constant.

For the two nuclei A and B, the velocity distribution is given by equations 1.6 and 1.7 as

$$\phi(v) = 4\pi v_A^2 \left( \frac{m_A}{2\pi k_B T} \right)^{\frac{3}{2}} e^{-\frac{m_A v_A^2}{2k_B T}} \quad (1.6)$$

$$\phi(v) = 4\pi v_B^2 \left( \frac{m_B}{2\pi k_B T} \right)^{\frac{3}{2}} e^{-\frac{m_B v_B^2}{2k_B T}} \quad (1.7)$$

Considering the kinetic energy,  $E = \frac{mv^2}{2}$ , the velocity distribution can be written as:

$$\phi(E) \propto E e^{\frac{-E}{k_B T}} \quad (1.8)$$

At very low energies,  $E \ll k_B T$  the  $\phi(E)$  increases with energy reaching a maximum at  $E = k_B T$  and decreases exponentially with energy at high energies ( $E \gg k_B T$ ), as shown in figure 1.1. Using the equations derived above, for the pair of nuclei A and B, the reaction rate per particle pair is:

$$\langle \sigma v \rangle = \int_0^\infty \int_0^\infty \phi(v_A)\phi(v_B)\sigma(v)v dv dv_A dv_B \quad (1.9)$$

where  $v_A$  and  $v_B$  are the relative velocities,  $v$  and the velocity of the centre of mass, V.

$$\phi(v) = 4\pi v^2 \left( \frac{\mu}{2\pi k_B T} \right)^{\frac{3}{2}} e^{-\frac{\mu v^2}{2k_B T}} \quad (1.10)$$

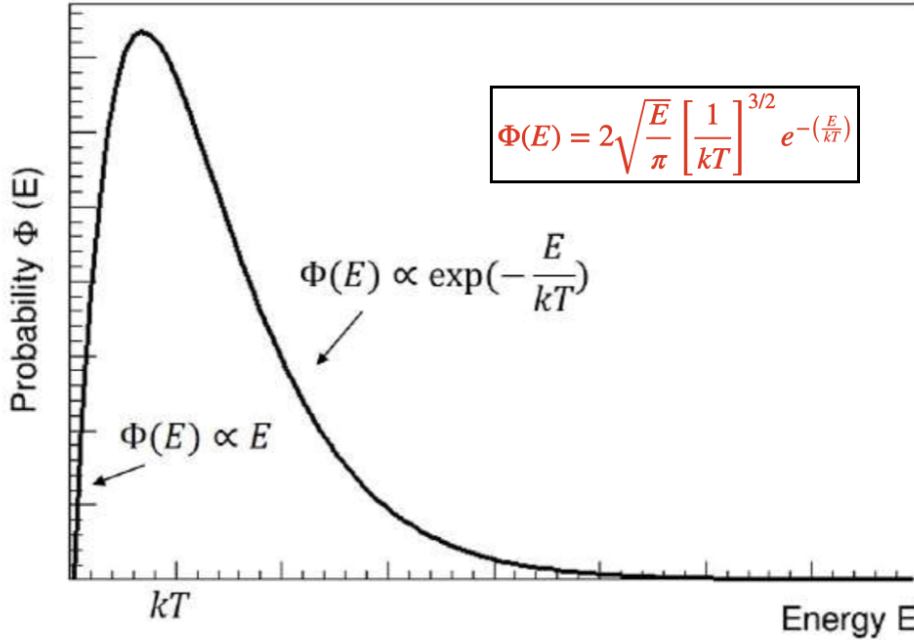


Figure 1.1: Maxwell Boltzmann Distribution of nuclei in stellar plasma.

$$\phi(V) = 4\pi V^2 \left( \frac{M}{2\pi k_B T} \right)^{\frac{3}{2}} e^{-\frac{MV^2}{2k_B T}} \quad (1.11)$$

where  $\mu = \frac{m_A m_B}{m_A + m_B}$  is the reduced mass and  $M = m_A + m_B$  is the total mass of the system. The reaction rate in terms of  $v$  and  $V$  as:

$$\langle \sigma v \rangle = \int_0^\infty \phi(V) dV \int_0^\infty \phi(v) \sigma(v) v dv \quad (1.12)$$

The nuclear cross section  $\sigma(v)$  depends only on the relative velocity  $v$ . Therefore, we can first integrate equation 1.12 over  $V$  to get

$$\langle \sigma v \rangle = \int_0^\infty \phi(v) \sigma(v) v dv \quad (1.13)$$

Inserting equation 1.10 in 1.13,

$$\langle \sigma v \rangle = 4\pi \left( \frac{\mu}{2\pi k_B T} \right)^{\frac{3}{2}} \int_0^\infty v^3 \sigma(v) e^{-\frac{\mu v^2}{2k_B T}} dv \quad (1.14)$$

Finally, introducing the centre of mass energy,  $E = \frac{1}{2}\mu v^2$ , equation 1.14 becomes

$$\langle \sigma v \rangle = \left( \frac{8}{\pi \mu} \right)^{\frac{1}{2}} \left( \frac{1}{k_B T} \right)^{\frac{3}{2}} \int_0^\infty \sigma(E) E e^{\frac{-E}{k_B T}} dE \quad (1.15)$$

### 1.1.1 Non-resonant reactions induced by charged particles

If we consider the interaction between two nuclei, there are two forces in play: the electromagnetic force and the strong nuclear force. The strong nuclear force is an attractive, short-range force dominating at distances in the order of the size of atomic nuclei. For the two interacting nuclei A and B with atomic radius  $R_A$  and  $R_B$ , the strong nuclear force dominates in the distance range lower than  $R = R_A + R_B$ . At distances greater than R, the Coulomb force dominates and is repulsive.

Fusion occurs when the energy of the projectile crosses the Coulomb barrier,  $E_c = \frac{1}{4\pi\epsilon_0} \frac{Z_A Z_B e^2}{r}$ . The energy of the stellar plasma is given by  $E = k_B T$ . This energy is much lower than the Coulomb barrier. The additional factor in play is the quantum mechanical effect called tunnelling (see figure 1.2).

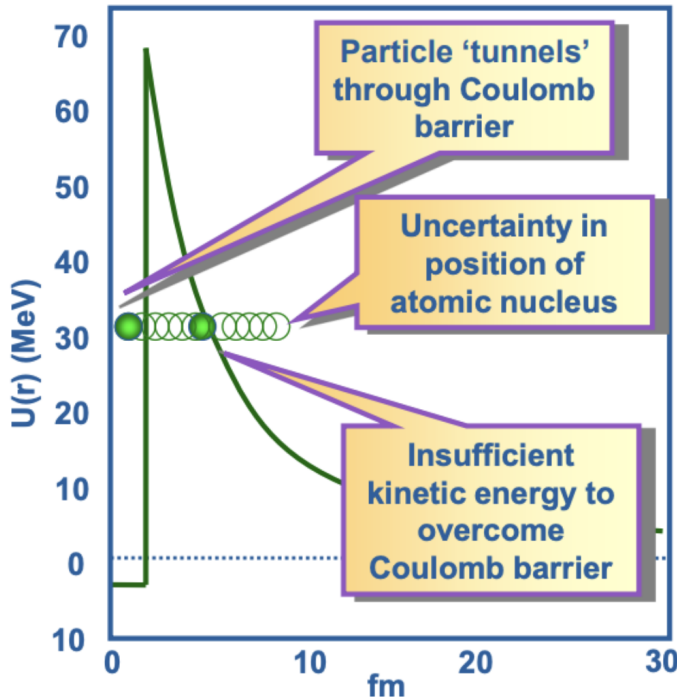


Figure 1.2: Schematic of the tunnelling of Coulomb barrier[3].

It states that even though the projectile has incident energy lower than the Coulomb barrier  $E_c$ ,

there exists a finite probability that the nuclear reaction can take place by crossing the barrier. At very low energies,  $E \ll E_c$ , the tunnelling probability can be approximated by the Gamow factor

$$P = e^{-2\pi\eta} \quad (1.16)$$

where  $\eta$  is the Sommerfeld parameter given by

$$\eta = \frac{Z_A Z_B e^2}{\hbar v} \quad (1.17)$$

As a result of the tunnelling effect, the cross-section falls rapidly at very low energies (Figure 1.3)

$$\sigma(E) \propto e^{-2\pi\eta} \quad (1.18)$$

The cross-section is also proportional to the de-Broglie wavelength

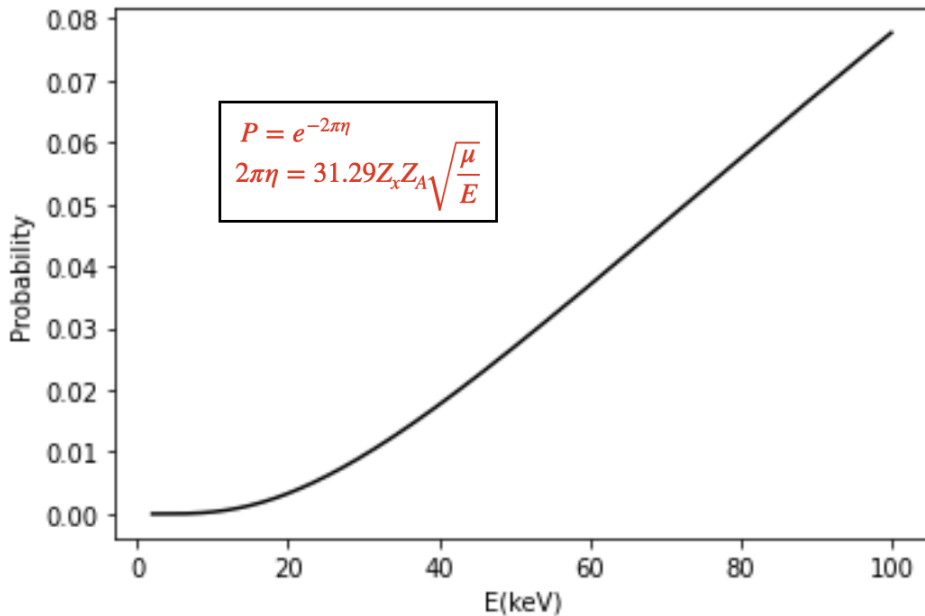


Figure 1.3: Tunnelling Probability v Energy.

$$\sigma(E) \propto \pi\lambda^2 \propto \frac{1}{E} \quad (1.19)$$

Combining equations 1.18 and 1.19, the cross-section can be written as

$$\sigma(E) = \frac{1}{E} e^{-2\pi\eta} S(E) \quad (1.20)$$

where  $S(E)$  is the astrophysical S-factor, which takes into account the nuclear properties of the involved reaction. For non-resonant reactions,  $S(E)$  is a slowly varying function of energy and is therefore very useful for extrapolation at low energies as shown in figure 1.4. Using equation 1.20 in 1.15, we get

$$\langle \sigma v \rangle = \left( \frac{8}{\pi \mu} \right)^{\frac{1}{2}} \left( \frac{1}{k_B T} \right)^{\frac{3}{2}} \int_0^\infty S(E) e^{\frac{-E}{k_B T} - \frac{b}{\sqrt{E}}} dE \quad (1.21)$$

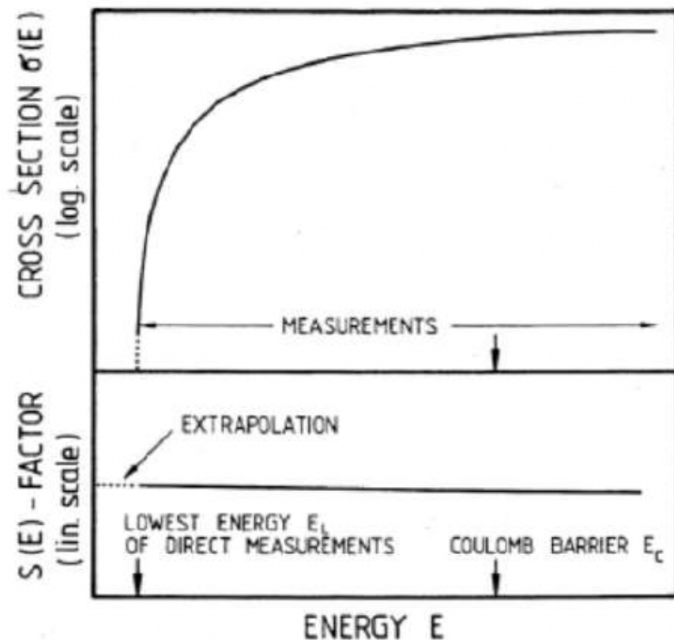


Figure 1.4: Cross-section for charged particle induced reactions. Top panel: Cross-section reduces rapidly at low energy, making extrapolation difficult. Bottom panel: The astrophysical S-factor on the other hand varies smoothly with energy and hence an extrapolation to lower energies is possible [1].

where the term  $b$  arises from the barrier penetrability.

$$b = \frac{\sqrt{2\mu} e^2 Z_A Z_B \pi}{\hbar} \quad (1.22)$$

The term  $b^2 = E_G$  is called the Gamow energy, which is the energy at which the fusion takes place inside stars.

As  $S(E)$  has a weak dependence on energy, the energy dependence in the integrand in equation 1.21 is governed by the two exponential terms,

- $e^{-\frac{b}{\sqrt{E}}}$  which arises from the penetration through the Coulomb barrier via tunnelling, that vanishes at low energies
- $e^{-\frac{E}{\sqrt{k_B T}}}$  which is a measure of the number of particles with energy E given by Maxwell-Boltzmann distribution, that vanishes at high energy.

The effect of the above two opposing terms leads to a peak at  $E_0 = \left(\frac{\sqrt{E_G k_B T}}{2}\right)^{\frac{2}{3}}$  known as the Gamow peak, which is illustrated in figure 1.5.

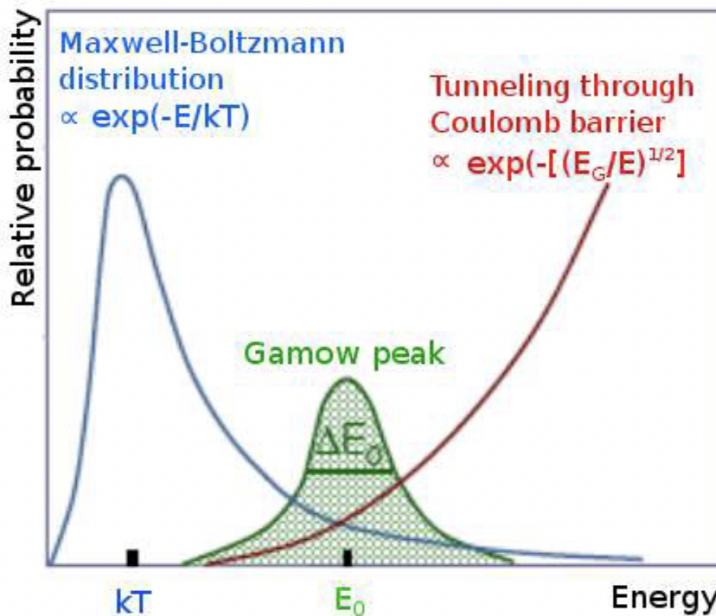


Figure 1.5: The Gamow peak: A convolution between Maxwell Boltzmann distribution of energies and tunnelling probability through the Coulomb barrier[4].

For a given temperature T, nuclear reactions take place in stars in an energy range  $\Delta E$ , which is the Gamow window, with a maximum at the Gamow peak,  $E_0$ . Substituting the value of  $E_0$  in equation 1.21, we get the maximum value of the integral

$$I_{max} = e^{-\frac{3E_0}{k_B T}} \quad (1.23)$$

For non-resonant reactions, Gamow peak can be defined by a Gaussian function.

$$e^{-\frac{E}{k_B T} - \frac{b}{\sqrt{E}}} = I_{max} e^{\left[-\left(\frac{E-E_0}{\Delta E/2}\right)^2\right]} \quad (1.24)$$

where  $\Delta E$  is the effective width of the peak

$$\Delta E = \frac{4}{\sqrt{3}} \sqrt{E_0 k_B T} \quad (1.25)$$

Nuclear fusion takes place in the energy range  $E_0 \pm \Delta E/2$ .  $E_0$  is lower than the Coulomb barrier and as a result, direct measurements of the cross-section are very difficult.

# Chapter 2

## Big Bang Nucleosynthesis

The Big Bang Nucleosynthesis is the source for the first light elements that were formed in the universe. The first half of this chapter will provide a brief theoretical background of cosmology, leading up to the BBN. In the second half, the significance of  $^2\text{H}(\text{p}, \gamma)^3\text{H}$  including a summary of the state of the art will be discussed.

### 2.1 Standard Model

The Standard Model of Cosmology, also known as the  $\Lambda\text{CDM}$  model, is the prevailing scientific framework that describes the structure and evolution of the universe on large scales. It combines the concepts of the Big Bang theory and general relativity to explain the origin, composition, and dynamics of the universe.

The Standard Model of Cosmology is based on the following key components [5]:

- **Big Bang Theory:** The model starts with the concept of the Big Bang, which suggests that the universe originated from an extremely hot and dense state about 13.8 billion years ago. It explains the expansion of the universe from a highly compact initial state to its current large-scale structure.
- **Primordial Nucleosynthesis:** The model predicts a period in the early universe where the conditions of temperature and density were suitable for the production of light elements such as the isotopes of H, He and Li (Section 2.2). This has been confirmed by observations of primordial clouds.
- **Expanding universe:** According to the model, the universe is continuously expanding. This expansion is supported by observational evidence, such as the redshift of distant galaxies, which indicates that they are moving away from us.
- **Cosmic Microwave Background (CMB):** The CMB is the faint radiation that permeates the entire universe. It is considered to be the afterglow of the Big Bang and provides crucial evidence for the early stages of the universe. The CMB is nearly uniform but has tiny temperature fluctuations that encode information about the structure of the early universe.

- **Dark Matter:** The Standard Model of Cosmology incorporates the existence of dark matter, which is an invisible and elusive form of matter that does not interact with light or other electromagnetic radiation. Dark matter is inferred from its gravitational effects on visible matter and its influence on the large-scale structure of the universe.
- **Dark Energy:** In addition to dark matter, the model posits the existence of dark energy, a mysterious form of energy that permeates space and is responsible for the accelerated expansion of the universe. Dark energy is thought to be associated with the cosmological constant or vacuum energy.
- **Large-Scale Structure:** The model explains the formation and evolution of the large-scale structure of the universe, including the distribution of galaxies, galaxy clusters, and cosmic filaments. Gravity plays a crucial role in driving the growth of structure from small initial density fluctuations.

While the Standard Model of Cosmology has been successful in explaining many observed phenomena and is supported by substantial observational evidence, there are still open questions and areas of ongoing research, such as the nature of dark matter and dark energy, the inflationary period of the early universe, and the ultimate fate of the cosmos.

The above features, along with the cosmological principle, that states the homogeneous and isotropic nature of the universe, form the cornerstones for the standard model. The principle implies that the metric itself is homogeneous and isotropic and is given by the Friedman Lemaitre Robertson Walker (FLRW) metric as follows [6]

$$ds^2 = g_{\mu\nu}dx^\mu dx^\nu = dt^2 - a^2(t) \left[ \frac{dr^2}{1-kr^2} + r^2(d\theta^2 + \sin^2\theta d\Phi^2) \right] \quad (2.1)$$

where  $g_{\mu\nu}$  is the metric tensor of four-dimensional spacetime,  $a(t)$  is the scale factor that describes the expansion and  $k$  describes the curvature of spaceime.  $k$  can take values -1, 0 and 1 that correspond to hyperbolic (open), Euclidean (flat) or elliptic (closed) geometries respectively.

The metric tensor  $g_{\mu\nu}$  is related to the Energy-Momentum Tensor  $T_{\mu\nu}$  through the Einstein equations

$$R_{\mu\nu} - \frac{R}{2}g_{\mu\nu} - \Lambda g_{\mu\nu} = 8\pi G T_{\mu\nu} \quad (2.2)$$

where  $R_{\mu\nu}$  is the Ricci tensor describing the tensor curvature,  $R$  is the Ricci scalar that describes the scalar curvature and  $\Lambda$  is the cosmological constant, originally introduced by Einstein to obtain a static cosmological model as the solution of the equation 2.2. Using equations 2.1 and 2.2, we obtain the First Friedmann equation

$$H^2 = \left( \frac{\dot{a}}{a} \right)^2 = \frac{8\pi G}{3}\rho - \frac{k}{a^2} + \frac{\Lambda}{3} \quad (2.3)$$

From the first law of thermodynamics,

$$dE + PdV = 0 \quad (2.4)$$

Assuming the universe is a perfect fluid,  $E = \frac{4\pi}{3}\rho a^3$  and  $V = \frac{4\pi}{3}a^3$  ( $c = 1$ ). The conservation of energy for the fluid is written as

$$\frac{4\pi}{3} \left( \frac{d}{dt}(\rho a^3) + P \frac{d}{dt}(a^3) \right) = 0 \quad (2.5)$$

$$0 = 3(\rho + P) \frac{da}{a} + d\rho \quad (2.6)$$

This is the Third Friedmann equation. Using 2.3 and 2.6, the Second Friedmann equation describing the evolution equation for the scale factor can be obtained:

$$\frac{\ddot{a}}{a} = -\frac{4\pi G}{3}(\rho + 3P) + \frac{\Lambda}{3} \quad (2.7)$$

Now we have to make an assumption: we will assume that the fluid is a barotropic perfect fluid. This means that the pressure is only dependent on the energy density,  $P = P(\rho)$ . Very often, this dependence is linear and the equation of state is given by

$$P = w\rho \quad (2.8)$$

where  $w$  is a dimensionless constant. Substituting equation 2.8 in 2.6, we can obtain

$$0 = 3(\rho + w\rho) \frac{da}{a} + d\rho \quad (2.9)$$

$$0 = 3\rho(1+w) \frac{da}{a} + d\rho \quad (2.10)$$

$$\frac{d\rho}{\rho} = -3(1+w) \frac{da}{a} \quad (2.11)$$

$$\log\rho = -3(1+w)\log a + \text{constant} \quad (2.12)$$

$$\log\rho a^{3(1+w)} = \text{constant} \quad (2.13)$$

$$\rho a^{3(1+w)} = \text{constant} \quad (2.14)$$

From 2.14, the dependence of the energy density on the scale factor can be obtained for matter, radiation and cosmological constant. For matter, radiation and the cosmological constant, pressure  $P$  is given by  $P_M = 0$ ,  $P_R = \rho_R/3$  and  $P_\Lambda = -\rho_\Lambda$  respectively, which corresponds to  $w$  values of  $w_M = 0$ ,  $w_R = 1/3$  and  $w_\Lambda = -1$ . Substituting these values of  $w$  in the equation 2.14, we get

$$\rho_M \propto a^{-3} \quad (2.15)$$

$$\rho_R \propto a^{-4} \quad (2.16)$$

$$\rho_\Lambda \propto \text{constant} \quad (2.17)$$

The present values of the energy densities for baryonic matter, dark matter, radiation and cosmological constant are expressed in terms of  $\Omega_i = \rho_i^0/\rho_{cr}$  where  $\rho_i^0$  represents the energy density for

matter, radiation and cosmological constant,  $\rho_{cr} = \frac{3H_0^2}{8\pi G}$  is the present value of the critical energy density and  $H_0 = 100h \text{ km s}^{-1} \text{ Mpc}^{-1}$  with  $h = 0.73^{+0.04}_{-0.03}$  [7]. Finally, the baryon density parameter,  $\omega_b = \Omega_b h^2$  and the baryon to photon ratio,  $\eta = n_B/n_\gamma$ . The ratio of present energy density to the critical density for matter, radiation and cosmological constant can be written as

$$\Omega_M = \frac{8\pi G\rho_M}{3H_0^2} \quad (2.18)$$

$$\Omega_R = \frac{8\pi G\rho_R}{3H_0^2} \quad (2.19)$$

$$\Omega_\Lambda = \frac{8\pi G\rho_\Lambda}{3H_0^2} = \frac{\Lambda}{3H_0^2} \quad (2.20)$$

Matter and radiation can be described in terms of a bath of particles and quantum fields. In particular, at high temperatures rapid interactions among them ensure thermodynamical equilibrium and each particle species is described by an equilibrium (homogeneous and isotropic) phase space distribution function

$$f_i(|p|, T) = \left[ e^{\left( \frac{E_i(|p|) - \mu_i}{T} \pm 1 \right)} \right]^{-1} \quad (2.21)$$

where  $E_i(|p|) = \sqrt{|p|^2 + m_i^2}$  is the energy, the  $\pm$  corresponds to Fermi-Dirac/Bose-Einstein statistics and  $\mu_i$  is the chemical potential. In a comoving frame, the number density, energy density and pressure of the particles can be written as [8]

$$n_i(T) = g_i \int \frac{d^3 p}{(2\pi)^3} f_i(|p|, T) \quad (2.22)$$

$$\rho_i(T) = g_i \int \frac{d^3 p}{(2\pi)^3} E_i(|p|, T) f_i(|p|, T) \quad (2.23)$$

$$P_i(T) = g_i \int \frac{d^3 p}{(2\pi)^3} \frac{|p|^2}{3E_i(|p|, T)} f_i(|p|, T) \quad (2.24)$$

where  $g_i$  is the number of internal degrees of freedom. The BBN occurred in the radiation-dominated phase and therefore the contribution to the energy density by the non-relativistic particles is negligible. The photon energy density is given by

$$\rho_\gamma = \frac{\pi^2 T^4}{15} \quad (2.25)$$

The total energy density can be written in terms of equation 2.25 as

$$\rho \sim \rho_R = g^* \frac{\rho_\gamma}{2} = g^* \frac{\pi^2}{30} \quad (2.26)$$

where  $g^*$  is defined as the number of relativistic degrees of freedom given by the equation

$$g^* = \sum_{B_i} g_i \left( \frac{T_i}{T} \right)^4 + \frac{7}{8} \sum_{F_i} g_i \left( \frac{T_i}{T} \right)^4 \quad (2.27)$$

where the first and second terms are due to all the boson and fermion species respectively.

## 2.2 Primordial Nucleosynthesis

The universe is theorized to have originated in a quantum gravity fluctuation in the Planck epoch (13.8 billion years ago [9] at  $10^{19}$  GeV). This was followed by a period of accelerated expansion of the universe called inflation. At the end of the inflationary period, the large energy density of the inflation was transformed into a plasma of short-lived and exotic particles and antiparticles at very high density, temperature and pressure. The collision rates were very high and the particles were in a state of thermal equilibrium [10]. This is when the universe became radiation-dominated. With the expansion, the universe cooled down and various particles diverged from the thermal equilibrium at different epochs, depending on the strength of their interactions. If we consider the universe at  $t = 0.1$  s [11], the temperature was in the order of  $\sim 3 \times 10^{10}$  K corresponding to an energy per photon of 10 MeV. Since this energy is much greater than the rest energy of electrons and positrons, there were positrons and electrons produced via pair production at  $t = 0.1$  s. During this phase, the protons and neutrons were in equilibrium via the reactions



While the protons and neutrons are in equilibrium, the number density of both species is provided by the Maxwell-Boltzmann equation as

$$n_p = g_p \left( \frac{m_p k_B T}{2\pi\hbar^2} \right)^{3/2} e^{-\frac{m_p c^2}{k_B T}} \quad (2.30)$$

$$n_n = g_n \left( \frac{m_n k_B T}{2\pi\hbar^2} \right)^{3/2} e^{-\frac{m_n c^2}{k_B T}} \quad (2.31)$$

The degrees of freedom for protons and neutrons are the same ( $g_p = g_n = 2$ ). So taking the ratio of the number densities in 2.31 and 2.30, we get

$$\frac{n_n}{n_p} = \left( \frac{m_n}{m_p} \right)^{3/2} e^{-\frac{(m_n - m_p)c^2}{k_B T}} \quad (2.32)$$

The ratio  $\frac{m_n}{m_p}$  can be approximated to one, and the difference in rest mass energies for a neutron and a proton,  $(m_n - m_p)c^2 = \Delta m = 1.29$  MeV. Using these two results in equation 2.32

$$\frac{n_n}{n_p} = e^{-\frac{\Delta m}{k_B T}} \quad (2.33)$$

For  $k_B T \gg \Delta m$ , corresponding to  $T \gg 1.5 \times 10^{10}$  K and  $t \ll 1$  s, the number of neutrons and protons is nearly the same. But as the temperature reduces due to the expansion of the universe, this equilibrium is broken and protons are strongly favoured. Thus the neutron-to-proton ratio drops exponentially.

In the early universe, the balance between the neutrons and protons is maintained through the interaction of the baryon with a neutrino or an anti-neutrino via the weak nuclear force. The interaction rate,  $\Gamma$  defined as

$$\Gamma = n\sigma|v| \quad (2.34)$$

where  $\sigma$  is the cross-section of the weak force which scales to  $T^2$  and  $n$  is the number density of massless particles that is proportional to  $T^3$  [12]. The interaction rate,  $\Gamma$  is proportional to  $T^5$ .

On the other hand, the Hubble parameter is proportional to  $T^2$ . Therefore, the interaction rate drops faster than the Hubble parameter as the universe expands and cools. The inverse of the Hubble parameter  $1/H$ , gives the age of the universe, while the inverse of the interaction rate  $1/\Gamma$  is the time taken for one interaction to happen. The high density and temperature conditions of the early universe mean that the average time for one interaction is much lower than the age of the universe ( $1/\Gamma > 1/H$ ). This is the condition that prevails at temperatures above 1 MeV and the neutrinos are in thermal equilibrium with the plasma through the reactions 2.28 and 2.29.

As the temperature drops below 1 MeV, the interaction rate becomes lower than the expansion rate and thus the neutrino interactions become too weak to keep them in thermal equilibrium. Therefore at  $\Gamma \sim H$ , the neutrinos decouple from the plasma and stop interacting with the baryons via reactions described in 2.28 and 2.29. This decoupling is not abrupt, and indeed the two-body reactions among neutrons, protons,  $e^\pm$  and  $\nu_e$  ( $\bar{\nu}_e$ ) continue to influence the  $n/p$  ratio, albeit not rapidly enough to allow the  $n/p$  ratio to track its equilibrium value (as shown in figure 2.1) of  $n/p = e^{-\frac{\Delta m}{T}}$ . Therefore, the  $n/p$  reduces from 1/6 at the time of decoupling, to a freeze-out value of 1/7[13] at the beginning of the BBN ( $\sim 200$  s).

The lack of neutrons for every proton explains why the BBN is so incomplete, as nearly 75 % of baryons remained as unfused protons at the end of the BBN. Despite the higher abundance, a proton fuses more readily with a neutron as interaction occurs via the strong force and also there is no Coulomb barrier for a proton and a neutron. This reaction produces a Deuterium atom and a photon. The fusion of two protons requires the Coulomb barrier to be overcome as well as the conversion of a proton into a neutron via the weak nuclear interaction whose cross-section is really low ( $\sim 10^{-43}$  cm $^2$ ). The probability for the fusion of two neutrons is extremely low due to their low abundance and the low cross-section of weak interaction.

Therefore, it can be assumed that the BBN proceeds till all the free neutrons are bounded into an atomic nucleus while the remaining protons remain as such. In this scenario, the mass fraction of  ${}^4\text{He}$  is found to be  $Y_p = 0.33$ [8]. In reality, this value is lower. From the freeze-out ratio of  $n/p = 1/7$ , the Helium mass fraction  $Y_p$  can be calculated as[13]:

$$Y_p = 4Y_{\text{He}}|_{fo} = \frac{2n_n}{n_p + n_n} = \frac{2n/p}{1 + n/p} = 0.25 \quad (2.35)$$

When the neutrinos decoupled from the plasma, the temperatures of photons, electrons and neutrinos are in equilibrium,  $T_\gamma = T_e = T_\nu$ . Shortly after decoupling, the temperature drops below the mass of an electron and thus the photons are unable to produce electron-positron pairs. However the electron-positron annihilation continues, adding energy density to the photons. This transfer of energy does not affect the neutrino temperature as they have already decoupled and a relation between the photon temperature after  $e^\pm$  annihilation and the neutrino temperature can be written

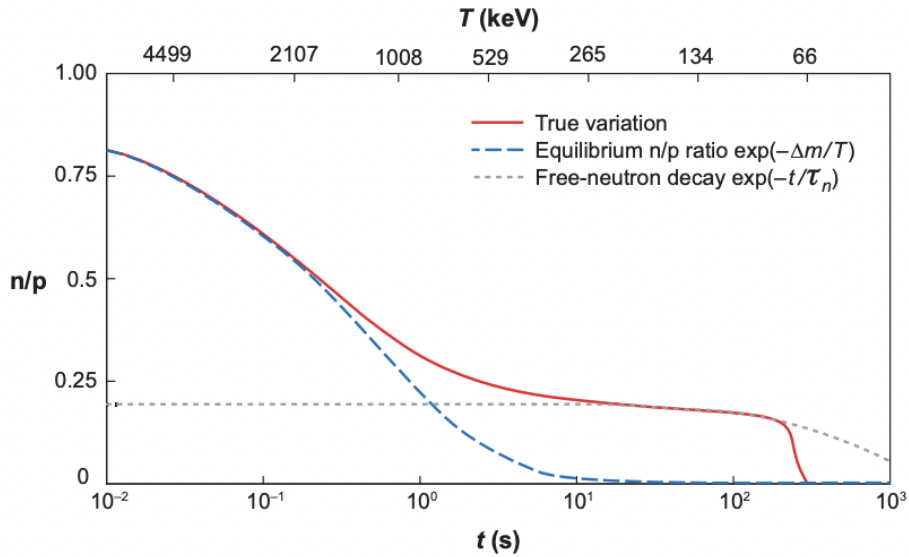


Figure 2.1: The time-temperature evolution of the neutron-to-proton (n/p) ratio. The solid red curve indicates the true variation. The steep decline at a few hundred seconds is the result of the onset of BBN. The dashed blue curve indicates the equilibrium  $n/p$  ratio  $e^{-\frac{\Delta m}{T}}$ , and the dotted grey curve indicates free-neutron decay  $e^{-\frac{t}{\tau_n}}$  [14].

as

$$\frac{T_\gamma}{T_\nu} = \left(\frac{11}{4}\right)^{1/3} \quad (2.36)$$

This is illustrated in figure 2.2 where the photon and neutrino temperatures coincide till  $T \sim 10^{10}$  K. Afterwards, due to the addition of energy from the  $e^\pm$  annihilation, the photon temperature is greater than the neutrino temperature by a factor of 1.4. In the next stage of the BBN, at  $t \sim 2$  s, the neutrinos are already decoupled while the photons are still coupled to the baryons. The Big Bang nucleosynthesis takes place through a series of two-body fusion reactions, building heavier nuclei progressively at each step. The first step, as discussed earlier, is the fusion of a proton and a neutron to form a Deuterium atom



with a Q-value of 2.22 MeV. This Q-value is also the binding energy of the Deuterium atom and therefore, any photon with energy higher than 2.22 MeV can dissociate into a proton and a neutron. This essentially makes the first step of the BBN a bottleneck, i.e., heavier nuclei than deuterium cannot form. This persists till the temperature drops below 2.22 MeV when there will be too few photons with enough energy to cause the dissociation and the production of Deuterium is favoured [16]. This transition occurs after the  $e^\pm$  annihilation at  $t \sim 3$  s when the temperature has dropped below 0.1 MeV.

Once a significant amount of Deuterium is formed, the BBN proceeds via the network of fusion

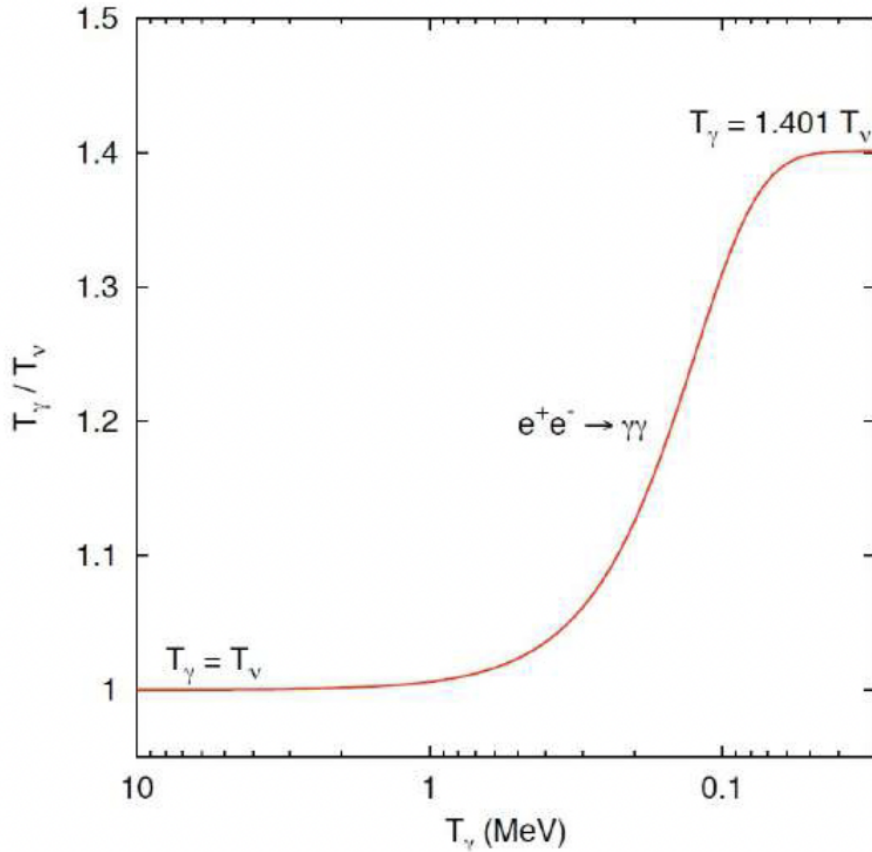
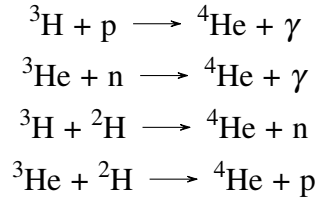


Figure 2.2: Photon and neutrino temperatures during the  $e^\pm$  annihilation[17].

reactions as shown in figure 2.3 and the heavier nuclei are formed. For example, the Deuterium formed can capture a proton to form  ${}^3\text{He}$  or capture a neutron to form tritium,  ${}^3\text{H}$ . Tritium is unstable and undergoes spontaneous  $\beta^-$  decay with a decay time of 18 years. But for the duration of the BBN ( $\sim 10$  mins[13]), tritium is quite stable and can undergo further reactions to form heavier nuclei.

Deuterium can also fuse to form tritium by emitting a proton or form  ${}^3\text{He}$  releasing a neutron. Although there are multiple channels for the creation of  ${}^3\text{He}$  and  ${}^3\text{H}$ , their respective concentrations during the BBN are always low as they are readily converted to  ${}^4\text{He}$  through the reaction channels



All these reactions proceed via the strong nuclear force and therefore have a high cross-section and a fast reaction rate. This aids the process of efficient conversion of  ${}^2\text{H}$ ,  ${}^3\text{H}$  and  ${}^3\text{He}$  to  ${}^4\text{He}$ .

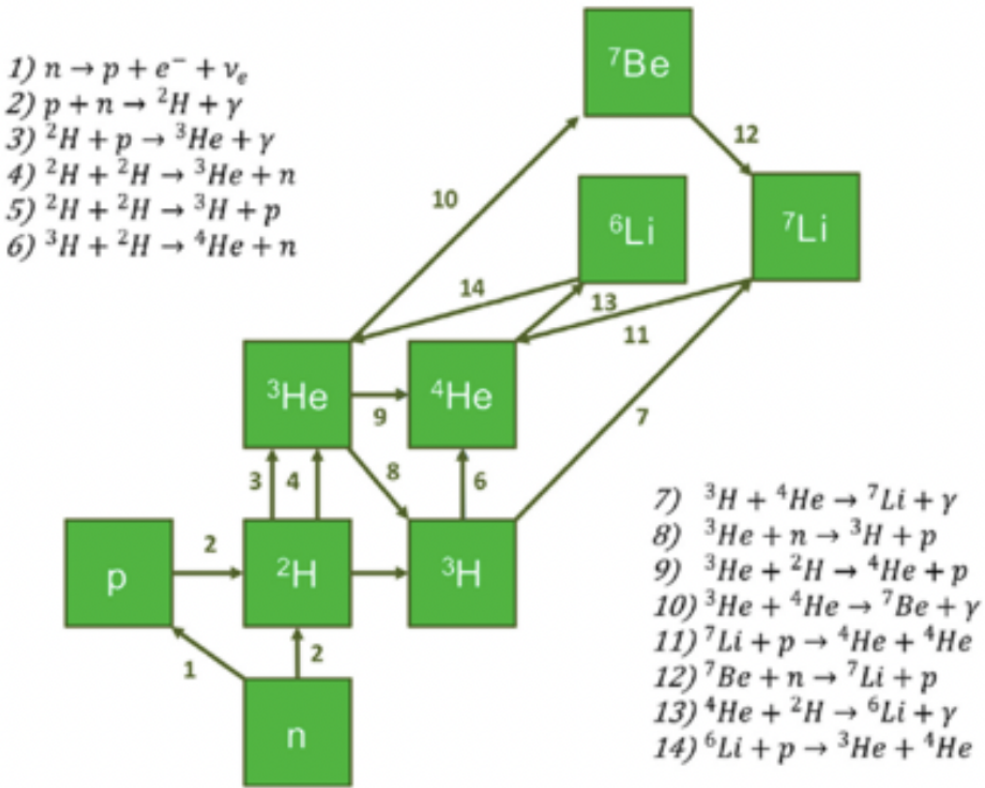
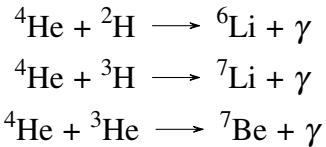


Figure 2.3: Big Bang Nucleosynthesis nuclear reaction chain.

After  $^4He$ , the formation of heavier nuclei is restricted by the fact that  $^4He$  is very tightly bound and stable. Moreover, there are no stable nuclei with mass number,  $A = 5$ . Due to this, a proton capture of  $^4He$  to form  $^5Li$  or a neutron capture to form  $^5He$  cannot work as neither  $^5Li$  nor  $^5He$  are stable. A small fraction of  $^6Li$ ,  $^7Li$  and  $^7Be$  are formed by the reactions



The absence of stable nuclei with  $A = 8$  halts the progression of BBN long enough that the temperature drops due to the expansion and the BBN stops by approximately 10 minutes[13] after the Big Bang. In figure 2.4, the chemical evolution of the nuclear species formed during the BBN is illustrated as a function of time and temperature.

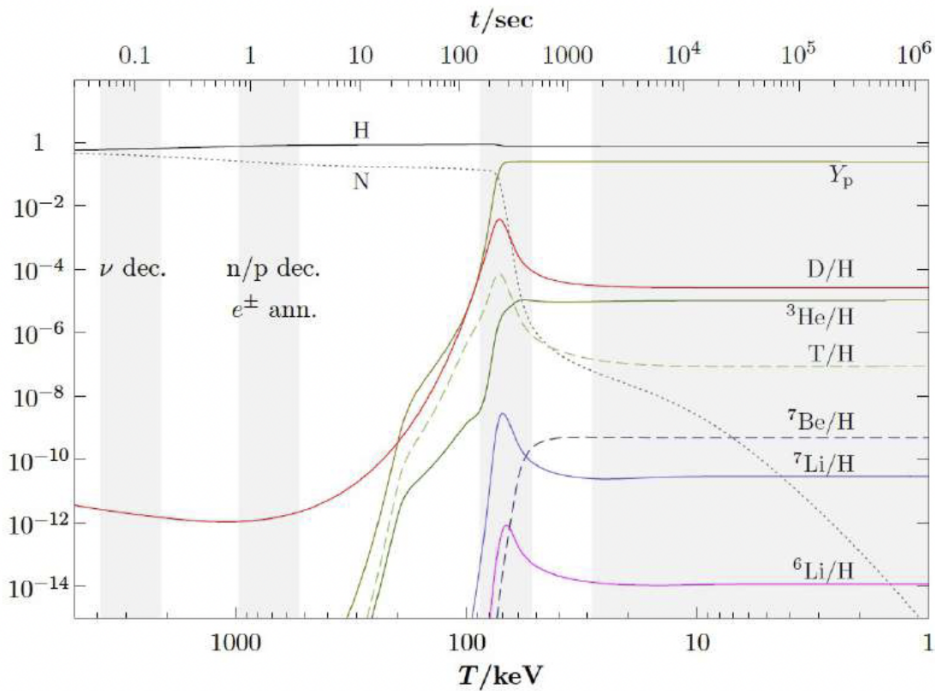


Figure 2.4: Mass fraction of nuclei as a function of time and temperature during the BBN.

## 2.3 Baryon-to-photon ratio, $\eta$

The yields of  $^2\text{H}$ ,  $^3\text{H}$ ,  $^3\text{He}$ ,  $^4\text{He}$ ,  $^6\text{Li}$ ,  $^7\text{Li}$  and  $^7\text{Be}$  depend on various parameters of which the most important is the baryon-to-photon ratio  $\eta$ . A higher  $\eta$  implies a larger baryon abundance, causing the BBN to commence at higher temperatures and hence an earlier start. As discussed earlier, the BBN is a race against time due to the expansion and cooling of the universe and thus, an earlier start to the BBN would imply a greater efficiency in converting all the neutrons into  $^4\text{He}$  nuclei, leaving a very low abundance of  $^2\text{H}$  and  $^3\text{He}$  behind. In figure 2.5, the variation of the mass fraction of different species produced in the BBN is plotted as a function of the baryon-to-photon ratio,  $\eta$  and the baryon density,  $\Omega_b h^2$ .

From the plot, it is clear that for larger values of  $\eta$ , the mass fraction of  $^4\text{He}$ ,  $Y_p$  increases and the deuterium abundance decreases, as explained above. For  $^7\text{Li}$ , the situation becomes a bit more complex. The production of  $^7\text{Li}$  through the fusion of  $^3\text{He}$  and  $^4\text{He}$  is a decreasing function of  $\eta$ , while the production of  $^7\text{Li}$  via electron capture of  $^7\text{Be}$  is an increasing function of  $\eta$ . This creates a minimum for the predicted primordial  $^7\text{Li}$  abundance at  $\eta \sim 3 \times 10^{-10}$ [18].

In general, if the baryon-to-photon ratio is as small as  $\eta \sim 10^{-12}$ , then the BBN would be extremely inefficient in producing  $^4\text{He}$  ( $Y_p \sim 0.01$ ). On the other side of the spectrum, if  $\eta$  is as large as  $10^{-7}$ [19], then the BBN would start early and the universe would essentially be deuterium and  $^3\text{He}$  free. In this scenario, the  $^4\text{He}$  mass fraction will be equal to its highest value of  $Y_p = 0.33$ .

Thus determining the value of  $\eta$  is very useful to calculate the primordial abundance of deuterium because the abundance is strongly dependent on the baryon-to-photon ratio in the range of interest

of 30 to 300 keV (during BBN). This means that finding the primordial abundance will allow us to estimate the value of the baryon-to-photon ratio  $\eta$ .

For a fixed  $\eta$ , the light element abundances relate to the Hubble expansion rate by

$$H^2 = 8\pi G\rho \sim g^* \frac{T^4}{m_{pl}} \quad (2.37)$$

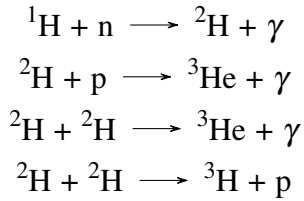
where  $m_{pl}$  is the Planck mass and  $g^*$  is the number of relativistic degrees of freedom. Thus by measuring the primordial abundance, it is possible to determine the number of relativistic species present during the BBN epoch, denoted by the number of neutrino species,  $N_{v,eff}$  [14]. Fixing the number of neutrino species to three, the primordial abundances depend only on the baryon-to-photon ratio,  $\eta$ . Relaxing this constraint, the primordial abundance calculation becomes a two-parameter theory: a function of  $\eta$  and  $N_{v,eff}$ .

## 2.4 Primordial D/H

As discussed above, the primordial deuterium abundance ratio (D/H) is a decreasing function of the baryon-to-photon ratio,  $\eta$ . The baryon-to-photon ratio can be related to the baryon density,  $\Omega_b h^2$  at present temperature of the Cosmic Microwave Background,  $T_{CMB} = 2.73$  K, as follows

$$\eta = \frac{n_b}{n_\gamma} = 5.4 \times 10^{-10} \left( \frac{\Omega_b h^2}{0.02} \right) \quad (2.38)$$

From 2.38, it is clear that D/H is a decreasing function of the baryon density  $\Omega_b h^2$ . Considering a slightly more general cosmological model with extra radiation, it grows as  $N_{v,eff}$  increases. Finally, it also depends on the cross-sections of the nuclear processes involved in the production of deuterium and subsequent synthesis to  $^3\text{H}$  and  $^3\text{He}$ . Specifically, the abundance depends on the reaction rate of the above-mentioned processes, obtained by the convolution of the energy-dependent cross-section of the reaction  $\sigma(E)$  and the thermal energy distribution of the incoming nuclei during the BBN. The main reactions involved in the altering of the primordial D/H ratio are



Among these reactions, the  $^2\text{H}(\text{p}, \gamma)^3\text{He}$  reaction, with  $Q = 5.493$  MeV is the most important channel for the destruction of Deuterium and therefore it affects the final deuterium abundance. The destruction of deuterium via  $^2\text{H}(\text{p}, \gamma)^3\text{He}$  depends on various physical parameters of which, the baryon-to-photon ratio  $\eta$  or equivalently (See Equation 2.38) the baryon density  $\Omega_b h^2$ , is the most important one.

The primordial deuterium abundance can be calculated using two independent approaches. The first method is through the direct observations of CMB anisotropies. The value of the baryon density

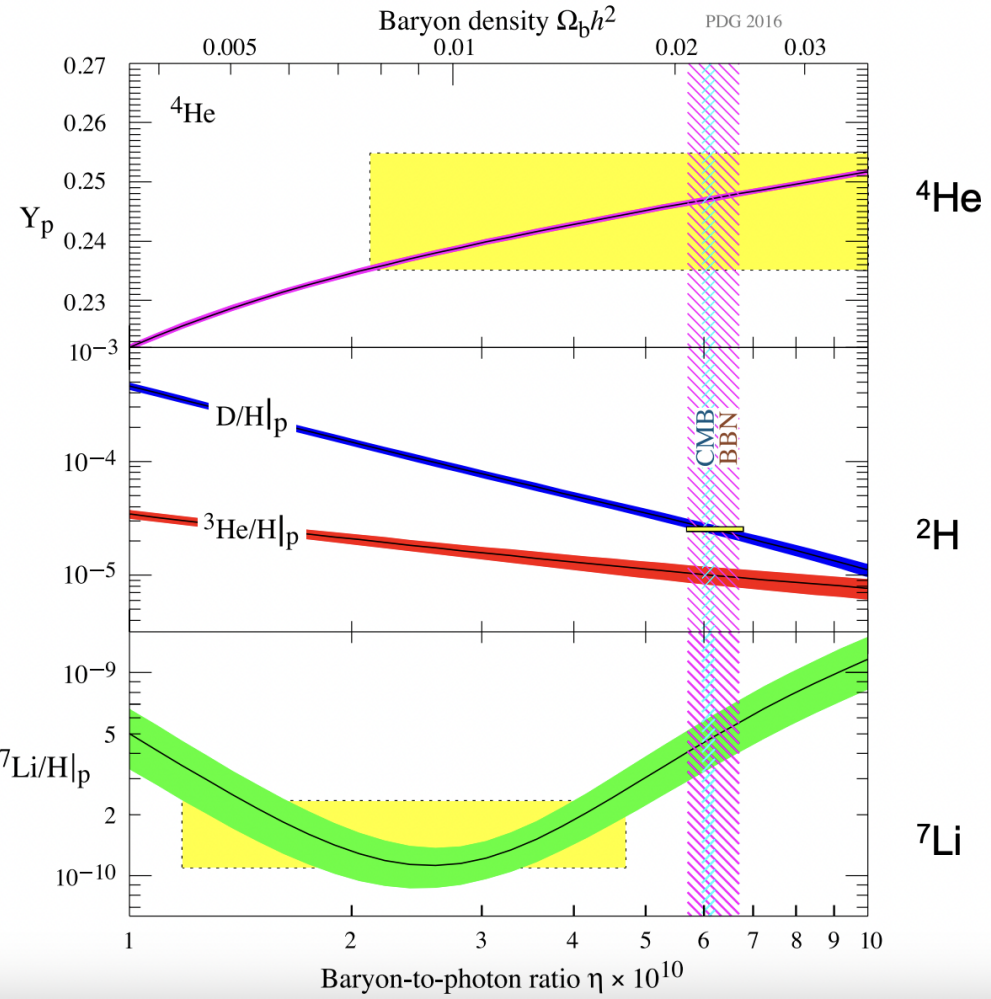


Figure 2.5:  $^4\text{He}$ ,  $^2\text{H}$ ,  $^3\text{He}$  and  $^7\text{Li}$  abundances plotted against the baryon-to-photon ratio. The yellow regions represent the observed abundances. Primordial deuterium abundance observed closely agrees with BBN theory, while primordial  $^3\text{He}$  has not been observed [20].  $^7\text{Li}$  on the other hand is observed at a much lower abundance, which is the famous cosmological lithium problem[21].

has been calculated by the PLANCK Collaboration [9] by studying the acoustic oscillations of the baryon-photon plasma in the CMB as

$$\Omega_b h^2 = 0.02242 \pm 0.00014 \quad (2.39)$$

at 0.7% precision. Using the public BBN codes [22], this value can be converted to a deuterium abundance ratio of

$$D/H = (2.51 \pm 0.07) 10^{-5} \quad (2.40)$$

Alternatively, the deuterium abundance can be obtained through BBN theory assuming the cosmological constants ( $\Omega_b h^2$  and  $N_{v,eff}$ ). The deuterium formed during the BBN is destroyed only through stellar evolution during the deuterium burning phase that precedes the main sequence

phase. Pristine clouds that have not undergone any stellar evolution will have the same deuterium abundance as the primordial abundance. Spectroscopic analysis of these clouds backlit by quasars can provide an accurate insight into the deuterium abundance. New data from very metal-poor Lyman-alpha systems at redshift  $z = 2.52564$ , visible in the spectrum of the quasar Q1243 + 307 [23] found the value at

$$D/H = (2.547 \pm 0.033)10^{-5} \quad (2.41)$$

with a 1.2 % precision.

This value obtained from BBN theory is less precise than the (indirect, model-dependent) cosmological determination from CMB data, with a smaller uncertainty. The structure of the absorption lines and the unfortunate level of unrelated contamination limit the accuracy with which the deuterium abundance has been measured in this system. These two deuterium abundance determinations, while broadly consistent, are off by 0.5 %. This small tension might be the result of experimental systematics due to the poor knowledge of the reactions cross-section of  $^2H(p, \gamma)^3He$ , as stated above.

## 2.5 $^2H(p, \gamma)^3He$ - State of the art

The  $^2H(p, \gamma)^3He$  reaction has been studied in different energy ranges in the past using different setups. Measurements at energies higher than 1 MeV (centre of mass energies) were measured by Berman et al. [24], Stewart et al. [25] and Fetisov et al. [26]. An overview of measurements below 1 MeV is provided below:

- **Griffiths 1962: The capture of protons by deuterons**[27].

The cross-section angular distributions have been measured at 275 keV to 1750 keV using ice targets produced by condensing  $D_2O$  vapour into a liquid air-cooled copper backing (gold backing to reduce the background) and a sodium iodide scintillation counter. The uncertainty has been given as a combination of statistical and systematical errors.

- **Griffiths 1963: The reaction  $^2H(p, \gamma)^3He$  below 50 keV**[28].

The reaction has been studied in the energy range from 24 keV to 48 keV, using heavy-ice targets on the liquid-air-cooled target and a Sodium iodine scintillation counter detector. The cross-section (equivalent S-factor) and differential cross-section have been measured. The main errors taken into account are statistical errors plus an error estimate for the extrapolation to the initial yield.

- **Bailey 1970:  $\gamma$ -ray yields from the reaction  $^2H(p, \gamma)^3He$  at low energies**[29].

Absolute cross-section and angular distribution in the energy range 57 to 1100 keV have been reported using a sodium iodide scintillation counter detector. The measurement was performed using the proton beam on a thin deuterated polyethene target deposited on a thin gold-plated, rotating copper disc. Furthermore, a gas target system was used for the normalization of the absolute cross-section.

- **Schmid 1997: The  $^2H(p, \gamma)^3He$  and  $^1H(d, \gamma)^3He$  reactions below 80 keV[30].**

Schmid et al. measured  $^2H(p, \gamma)^3He$  and  $^1H(d, \gamma)^3He$  at the centre of mass energies in the range 10 to 50 keV. In this work, both polarized and unpolarized incident beams have been used for measurements of cross-section and the astrophysical S-factor. Moreover, the  $\gamma$ -ray linear polarization P was measured for an unpolarized incident beam. For the  $^2H(p, \gamma)^3He$  reaction, the experiment was performed using a proton beam on a solid target of  $D_2O$  (99% pure) condensed on a cooled (80 K) Cu disc on an Al target chamber and an HPGe detector of 130% efficiency. The final uncertainties were calculated considering statistical and systematical components. The latter depends on beam current integration (1%), efficiency measurements at 5.5 MeV (6%), and stopping cross section (6%).

- **Ma 1997: Measurements of  $^1H(d, \gamma)^3He$  and  $^2H(p, \gamma)^3He$  at very low energies[31].**

Ma et al. measured the absolute differential cross sections, total cross section and the angular distribution of  $^2H(p, \gamma)^3H$  reaction in the energy range 70 to 210 keV. A thick layer of vapour-condensed heavy ice (high purity  $D_2O$ ) was used. The targets were periodically melted to reduce the neutron-induced background. The detection system consisted of two large HPGe detectors. For the final analysis, the systematic component of the uncertainty was estimated to be 9%. This systematic component was significantly less than the statistical uncertainty and was not included in the final uncertainty estimation.

- **LUNA 2002: First measurement of the  $^2H(p, \gamma)^3H$  cross-section down to the solar Gamow peak [32].**

The low energy range of the  $^2H(p, \gamma)^3H$  reaction is dominated by the measurements of the LUNA collaboration. The cross-section has been measured in the Solar Gamow peak (2.5 to 22 keV centre of mass energies) using a differentially pumped gas-target system and a BGO detector. The two primary sources of uncertainty were statistical uncertainties of 3.6-5.3%, very low compared to the systematical uncertainty ( $\approx 40\%$ ) due to the description of the reaction geometry in MC simulation, pressure profile, gas temperature, and the number of projectiles impinging on the calorimeter.

- **NACRE: A compilation of charged-particle induced thermonuclear reaction rates[33].**

It is not always possible to have experimental measurements for nuclear reactions at astrophysical energies. To overcome such a problem, different fitting procedures for the low-energy extrapolation have been performed. One of the fits done for the  $^2H(p, \gamma)^3He$  reaction has been performed by Angulo et al [33]. Because of the lack of experimental data down to very low energies and a discrepancy of 50% between [28] and [30] data, a unique extrapolation to zero energy was not possible. The astrophysical S-factor has been fitted with a polynomial function of degree 3, using [28] for lower limits and [30] for upper ones.

- **NACRE II: A compilation of charged-particle-induced thermonuclear reaction rates[34].**

Xu et al.[34] have performed a fit in which post-NACRE data [32] and [35] have been added, extending the energy range down to 2 keV.

- **SolarFusion II: Cross sections II: the pp chain and CNO cycles[36]**

Adelberger et al.[36] present one of the most important S-factor fit for the  $^2H(p, \gamma)^3He$  reac-

tion. It has been performed fitting the experimental data from [27],[30], [31] and [32] with a polynomial function of degree 3.

- **R-matrix: Compilation and R-matrix analysis of Big Bang nuclear reaction rates[37].**  
In Descouvemont et al., S-factor extrapolation at lower energies, where no experimental data is available, has been obtained by using the R-matrix technique in which the cross-section has been calculated using Coulomb functions. In other words, this technique can parametrize some experimentally known quantities such as the cross-sections or phase shifts, with a small number of parameters, which are then used to extrapolate the cross-section down to astrophysical energies.

- **Marcucci 2016: Implication of the Proton-Deuteron Radiative Capture for Big Bang Nucleosynthesis[38].**

$^2\text{H}(p, \gamma)^3\text{He}$  reaction is of high interest also for theoretical nuclear physics. The astrophysical S-factor in the BBN energy range is calculated using an ab initio approach. It consists of a quasi-exact solution of the Schrodinger equation determined by experimental measurements. This method has been improved over the years and its latest implementation is discussed by Marcucci et al. [38] In this last work particular attention is paid to the determination of the S-factor with an uncertainty of 1% or even less and its implication on the deuterium primordial abundance. Using the most recent determination of the baryon density of the Planck experiment, and with a standard number of relativistic degrees of freedom  $N_{V,eff} = 3.046$  during primordial nucleosynthesis, an excellent agreement between the predicted value and the experimental determination of the deuterium abundance is reached.

- **LUNA 2020: The baryon density of the universe from an improved rate of deuterium burning[39].**

In Mossa et al.,[39] the cross-section of  $^2\text{H}(p, \gamma)^3\text{He}$  is measured in the BBN energy range of 32 - 263 keV at the LUNA 400 kV accelerator at LNGS. A high-purity windowless Deuterium gas target, maintained at 0.3 mbar, was bombarded using an intense proton beam and the  $\gamma$ -rays produced were detected using a High Purity Germanium (HPGe) detector. The results obtained are shown in figure 2.6 along with previous measurements. The LUNA fit provided an improvement on the earlier estimates for the cross-section for  $^2\text{H}(p, \gamma)^3\text{He}$  and the corresponding baryon density calculated from the BBN codes[22] were found to be precise to a 1.6% level, and in excellent agreement with the measurement of  $\Omega_b h^2$  by the PLANCK Collaboration [9].

- **Turkat 2021: Measurement of the  $^2\text{H}(p, \gamma)^3\text{He}$  S-factor at 265–1094 keV[40].**

Turkat et al.[40] studied the cross-section of  $^2\text{H}(p, \gamma)^3\text{He}$  in the energy range 265 to 1094 keV, corresponding to an earlier phase of BBN at higher temperatures. The experiment was performed at the Ion Beam Center of Helmholtz-Zentrum Dresden-Rossendorf (HZDR), Dresden, Germany. The accelerator provided an intense proton beam of energy 265 to 1094 keV (in the centre-of-mass frame) at an intensity of 3 - 4  $\mu\text{A}$  intensity on a solid target. The solid Titanium Deuteride (TiD) was prepared using low-energy ion implantation at HZDR. The S factor obtained is shown in figure 2.7 along with previous measurements. The HZDR

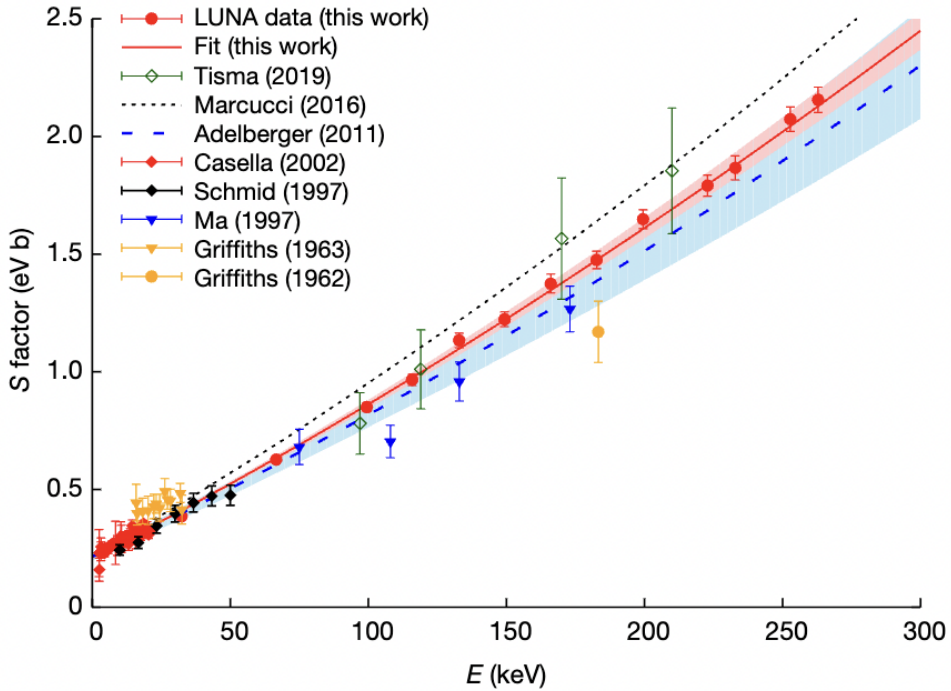


Figure 2.6: LUNA result (red points and red line)[39] for S-Factor for  ${}^2\text{H}(\text{p}, \gamma){}^3\text{He}$  in comparison with previous measurements.

measurement, when compared to the extrapolation of LUNA measurement [39], is higher by  $\sim 10\%$ . The new data support a higher S factor at Big Bang temperatures than previously assumed, reducing the predicted deuterium abundance.

## 2.6 Physical Motivation for this Work

Given the discrepancy between the high-energy Turkat et al.[40] data and the LUNA high-energy extrapolation[39], a new measurement for the cross-section of  ${}^2\text{H}(\text{p}, \gamma){}^3\text{He}$  is proposed. This measurement will be done in the energy range of 300 to 800 keV, overlapping with the LUNA measurement as well as the high-energy HZDR measurement, to contain the existing tension between the two. Since the LUNA measurement is the most precise measurement made to date in the BBN energy range, this new measurement will allow confirmation of the results of LUNA through a completely independent experiment (different accelerator, target and detector setup). Therefore, this thesis work will provide a new cross-section over a wide energy range. The combination of the present results with the previous LUNA data allows us to improve the existing theoretical models for primordial nucleosynthesis. The new proposed experiment will also explore the angular distribution measurement for the  ${}^2\text{H}(\text{p}, \gamma){}^3\text{He}$  reaction.

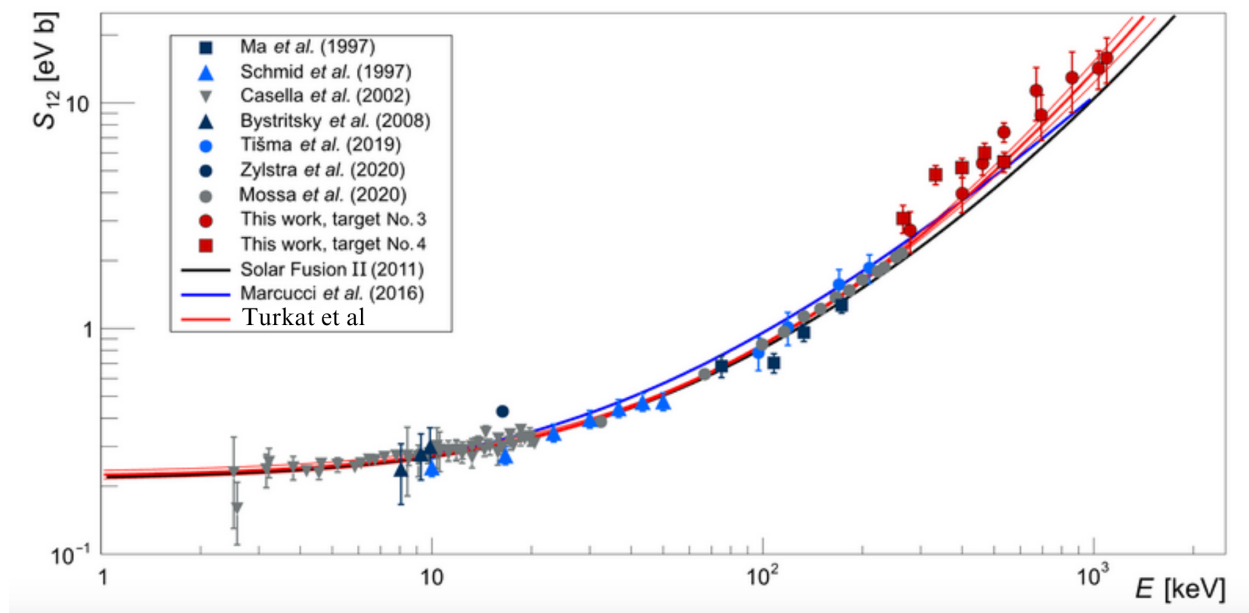


Figure 2.7: S-factor fit of  ${}^2\text{H}(\text{p}, \gamma){}^3\text{He}$  reported in Turkat et al[40] in comparison with previous studies.

# Chapter 3

## $^2\text{H}(\text{p}, \gamma)^3\text{He}$ at Felsenkeller

Proton captures induced by charged particles are studied through  $\gamma$ -ray spectroscopy. The  $^2\text{H}(\text{p}, \gamma)^3\text{He}$  reaction has been measured directly at the BBN energy range (30 to 300 keV) by the LUNA Collaboration[39] and at higher energies by Turkat et al.[40] in HZDR. In this chapter, a new experimental campaign of the  $^2\text{H}(\text{p}, \gamma)^3\text{He}$  reaction overlapping with both LUNA and HZDR data is reported.

This chapter will start with the description of the underground Felsenkeller laboratory followed by the experimental setup for the study of the  $^2\text{H}(\text{p}, \gamma)^3\text{He}$  reaction.

### 3.1 Felsenkeller Laboratory

Felsenkeller facility[41] has a 5 MV Pelletron accelerator installed in a shallow underground laboratory in Dresden, Germany. The accelerator is run in collaboration with the Helmholtz-Zentrum Dresden Rossendorf (HZDR) and the Technical University of Dresden (TUD). The facility is under 40 m of rock overburden, equivalent to 140 m of water, which reduces the muon background by a factor of 40 and the neutron background by a factor of 180. Overall, the cosmic ray effects are attenuated by 99% providing a high level of background suppression.

In figure 3.1, the  $\gamma$ -background at Felsenkeller compared with other laboratories is given. Felsenkeller, as described above, has a 99% reduction of the  $\gamma$  background which includes the natural radioactivity, which dominates below 3 MeV and cosmic ray and neutron-induced events which dominate above 3 MeV[42]. Such a background reduction is sufficient to study the  $^2\text{H}(\text{p}, \gamma)^3\text{He}$  reaction which has a relatively high cross-section in the order of micro barns ( $\approx 10^{-30}\text{cm}^2$ ) and the gammas of interest are above 3 MeV.

The laboratory consists of two connected tunnels dug into a cliff face (Figure 3.2). The 5 MV Pelletron tandem accelerator has been installed at the far end of the tunnels. The accelerator works in two modes: tandem and single-ended. In tandem mode, which is the original mode of operation, negatively charged ions are accelerated towards a positive terminal voltage, where an electron stripping system rids the ions of two or more electrons, thus converting them to positively charged ions. These positive ions are then once more accelerated to ground potential, to the high-energy side of the accelerator. On the other hand, in the single-ended mode, the positive ions are directly

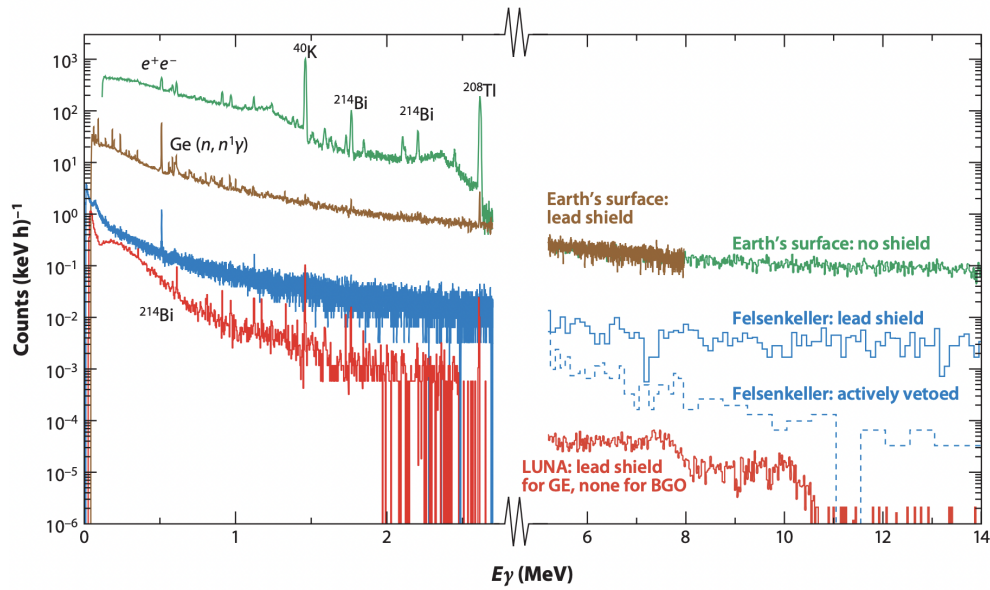


Figure 3.1:  $\gamma$ -background on the Earth’s surface, at Felsenkeller and LUNA in Gran Sasso.

produced at the voltage terminal and then accelerated. An internal ion source is installed and the ions are directly produced at the voltage and then accelerated. The internal ion source provides  $^4\text{H}$  and  $^2\text{H}$  beams.

Once accelerated, the ion beam is transported via evacuated beamlines to the high-energy electromagnet, and then to the target chamber for the proposed experiment. The magnet also acts as a filter, filtering out all unwanted particles in the beam with the wrong mass and charge.

The scientific experiments are carried out in two concrete bunkers, which are surrounded by a 40 cm layer of reinforced concrete. The cement, sand, and gravel had been analyzed before each load of concrete was mixed, to ensure a specific radioactivity of less than 20 Bq/kg both for the uranium and for the thorium chain of naturally occurring radioactive materials.

## 3.2 Experimental Setup

For the  $^2\text{H}(p, \gamma)^3\text{He}$  experiment, the accelerator provides a proton beam of 300 - 800 keV lab energy, at  $5 \mu\text{A}$  intensity. The beam energy is calibrated using the magnet scan approach and resonance scan of the well-known resonances of  $^{27}\text{Al}(p, \gamma)^{28}\text{Si}$ ,  $^{14}\text{N}(p, \gamma)^{15}\text{O}$  and  $^{13}\text{C}(p, \gamma)^{14}\text{N}$ .

The target is mounted at the end of the beamline in bunker 111. The target closes the beamline and works as a beamstopper. The beam current is acquired on the target by using the Faraday cup approach. In close vicinity around the target, 4 high purity germanium (HPGe) detector clusters and two single crystal HPGe detectors have been set up at various angles and distances to the target as displayed in figures 3.3 and 3.4. The euroball (EB) septuple cluster EB18 is set up looking vertically down onto the target, while euroball septuple cluster EB17 along with the miniball triple clusters MB1 and MB2 as well as the single cluster Ronald 100 (Ron100) and the single crystal

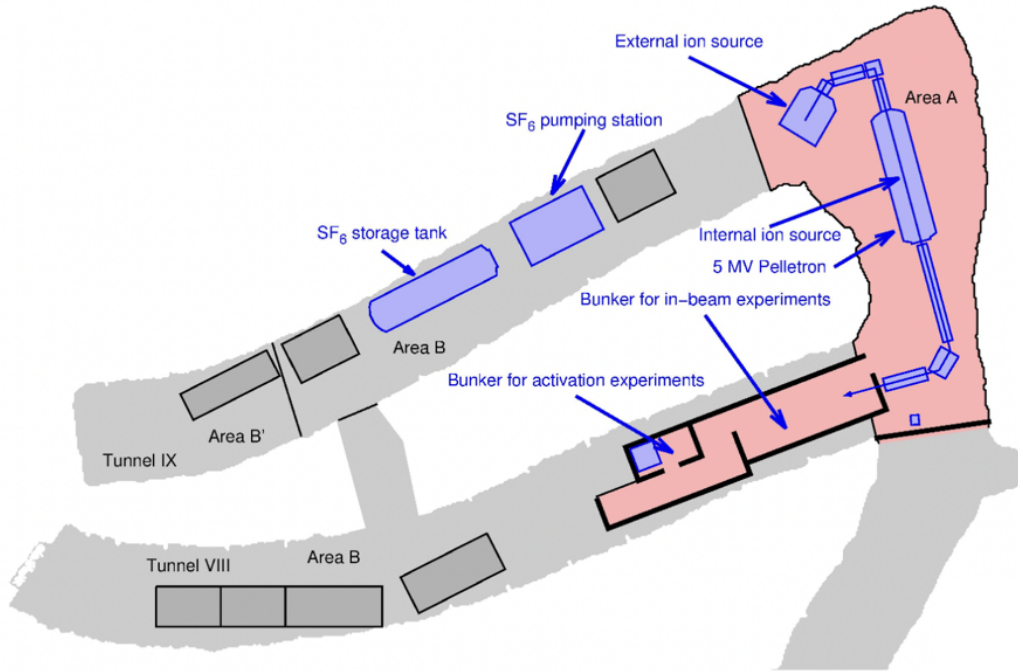


Figure 3.2: Overview of the Felsenkeller laboratory in Dresden, Germany.

detector Canberra60 (Can60) are all in the same horizontal plane as the target. To further reduce the effects of natural background in the  $\gamma$  spectra, a lead castle has been built around the entire detector setup providing further shielding. The cluster MB1 and the detector Can60 additionally each have a Bismuth-Germanate-Oxide-Detector (BGO) surrounding the HPGe detectors which function as a muon and Compton veto detector. If an event is detected in coincidence in the BGO and the germanium detector, then it is either unwanted radiation from outside of the detector set-up, such as a muon that has made it through the rock and lead or it is an escaping photon from Compton scattering. Either way, discarding this event reduces unwanted background or the Compton continuum, improving the peak-to-Compton and background ratios. It was not possible to equip every cluster with a BGO, as the space required for the BGOs would mean, that the clusters would have to be positioned at a further distance, which is detrimental to the detection efficiency.

Each detector cluster is divided into single crystals; in total the 6 HPGe detectors are partitioned into 22 crystals, each of which can be read out and analyzed separately. It is important to know the angles at which the detectors are positioned, to measure the angular distribution of the  $^2\text{H}(P, \gamma)^3\text{He}$  reaction. Furthermore, a detector that is not under  $90^\circ$  to the target can potentially see Doppler shifts in the spectrum (see section 4.1.9).

A summary of the detector positions is provided in table 3.1. These are preliminary measurements done with a protractor and a measuring tape in a complicated setup. To measure the angles, the

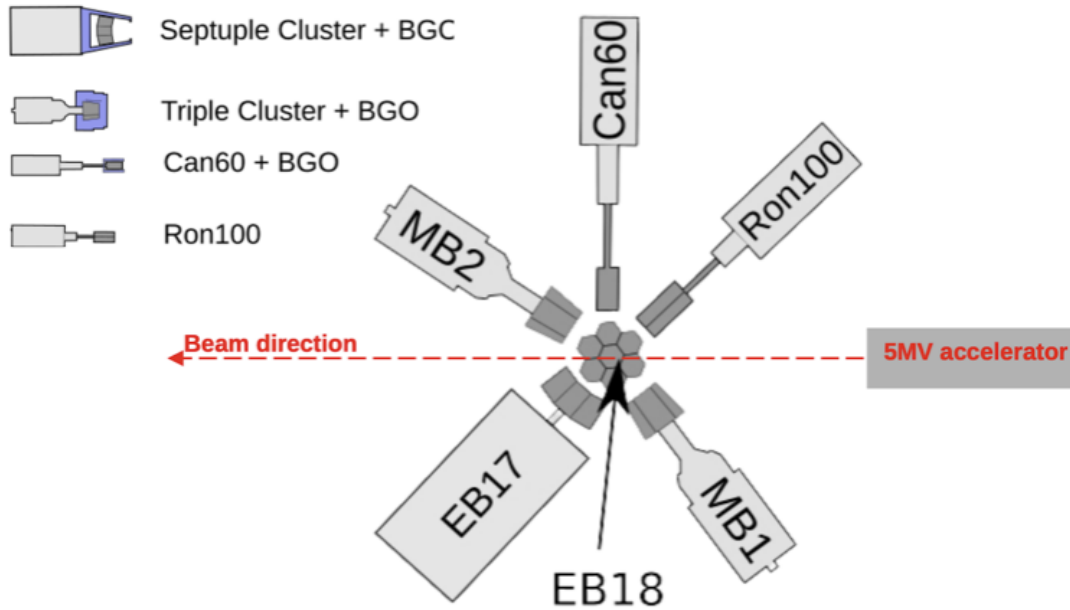


Figure 3.3: Detector Setup (View from Top).

target was taken as the centre point and then a laser was aligned through this point with the centre of the end cap of each detector. The angle was measured from the extension of the beamline to the centre of the end cap of each detector. Thus, detectors downstream of the target, such as MB2 are at small angles, whereas detectors upstream of the target such as MB1 are at large angles. The distances were measured with a measuring tape to the front of the end cap of the detectors. These preliminary measurements will be used for further analysis in this thesis.

The entire beamline and the target are enclosed within a steel pipe, which is constantly evacuated with multiple pumps. The target itself is held in place in the centre of the beamline by a copper target holder. This target holder extends from the back of the beamline to the position of the target. This means, that every detector in a position of less than  $\theta = 90^\circ$  is additionally shielded from the target by part of the target holder.

For the experiment, two types of solid targets were prepared: TiD and ZrD<sub>2</sub>. TiD was prepared at HZDR, Dresden through low energy ion implantation on Tantalum backings while ZrD<sub>2</sub> was prepared at INFN, Legnaro through reactive sputtering on Tantalum backings. The target chamber is cooled using LN<sub>2</sub> connected via the dewars as shown in figure 3.4.

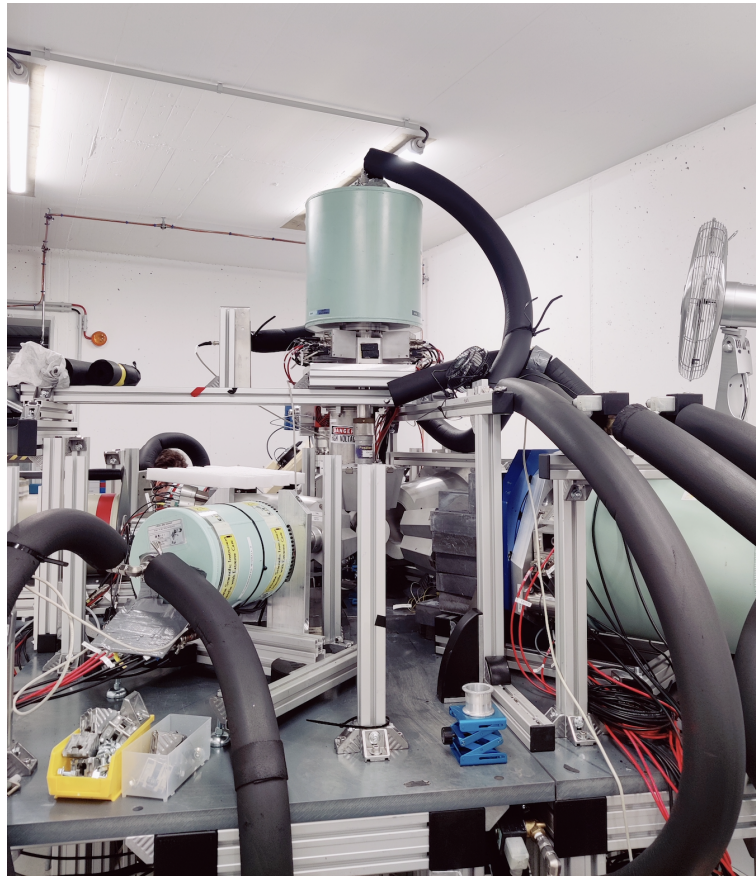


Figure 3.4: Part of the experimental setup can be seen.

Table 3.1: Detector positions at Felsenkeller.

Detector	Angle (wrt beamline) in $^\circ$	Distance from target (in cm)
EB18	90	5.0
EB17	39	20.1
MB1	118	18.5
MB2	36	18.4
Can60	89	19.0
Ron100	143.5	15.5

# Chapter 4

## Data Analysis

In this section, a detailed description of the data analysis carried out, starting with the calibration of the detectors, the calculation of the cross-section for  $^2\text{H}(\text{p}, \gamma)^3\text{He}$  and finally the angular distribution of the cross-section. In this thesis, the data analysis is performed on the  $\text{ZrD}_2$  solid target prepared at Legnaro (LNL\_125\_1)

### 4.1 Efficiency Calibration

For the first step in our analysis, we calibrate the efficiency of all the detectors. The efficiency of the detector is defined as the ratio of the number of  $\gamma$ -rays that are counted in the detector to the number of  $\gamma$ -rays produced from the target chamber.

This is done by using calibrated radioactive sources. In this campaign, we use  $^{60}\text{Co}$ ,  $^{137}\text{Cs}$ ,  $^{88}\text{Y}$  and  $^{22}\text{Na}$ . The activities of the samples are listed in table 4.1.

Table 4.1: Radioactive Sources for Calibration.

Sample	Calibration Date	Activity (kBq)
$^{60}\text{Co}$	1 Jan 2005	$260.7 \pm 1.9$
$^{137}\text{Cs}$	1 Jan 2005	$11.2 \pm 0.12$
$^{22}\text{Na}$	1 Jul 2020	$49.3 \pm 0.5$
$^{88}\text{Y}$	12 Jan 2022	$103.2 \pm 0.7$

#### 4.1.1 $^{137}\text{Cs}$

$^{137}\text{Cs}$  is a radioactive nucleus which has a half-life of 30.08 years. It undergoes  $\beta^-$  decay to reach the metastable state of  $^{137}\text{Ba}^m$ , before decaying to the ground state  $^{137}\text{Ba}$  by emitting a photon of 662 keV. The decay level scheme is shown in figure 4.1.

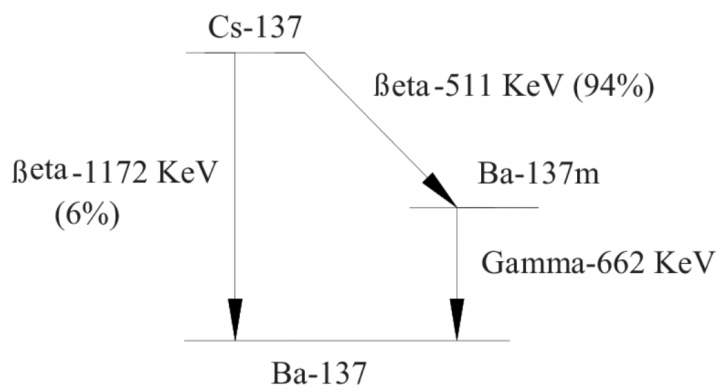


Figure 4.1: Decay level scheme of  $^{137}\text{Cs}$ .

#### 4.1.2 $^{60}\text{Co}$

The radioactive isotope  $^{60}\text{Co}$  has a half-life of 1925.28 days. The nucleus undergoes a  $\beta^-$  decay to form  $^{60}\text{Ni}$  by emitting two photons of energies 1173.23 keV and 1332.49 keV respectively, as shown in the decay level scheme in figure 4.2.

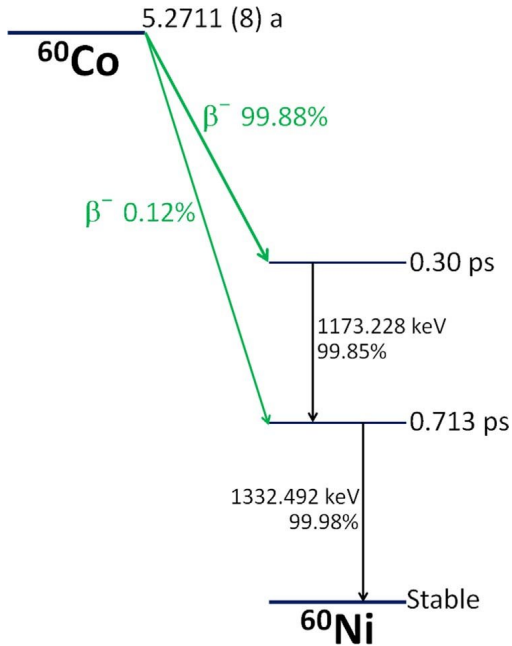


Figure 4.2: Decay level scheme of  $^{60}\text{Co}$ .

### 4.1.3 $^{22}\text{Na}$

The radioactive nuclei  $^{22}\text{Na}$  has a half-life of 2.6018 years. It undergoes a  $\beta^+$  decay to form  $^{22}\text{Ne}$  in the excited state before decaying to its ground state by emitting a photon of energy 1274.5 keV. The decay level scheme is shown below in figure 4.3.

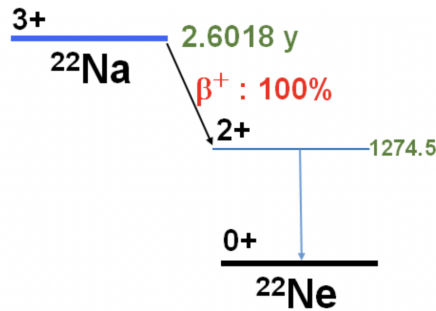


Figure 4.3: Decay level scheme of  $^{22}\text{Na}$ .

### 4.1.4 $^{88}\text{Y}$

$^{88}\text{Y}$  is a radioactive isotope of Y that has a half-life of 106.626 days. It undergoes a  $\beta^+$  decay to form  $^{88}\text{Sr}$  in the excited state before decaying to its ground state by emitting two photons of energies 898.04 keV and 1836.07 keV respectively. The decay level scheme is shown below in figure 4.4.

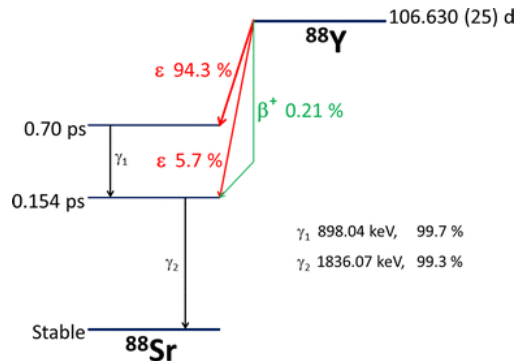


Figure 4.4: Decay level scheme of  $^{88}\text{Y}$ .

The radioactive sources above cover an energy range from 662 keV to 1836 keV. Since the Q-value of  $^2\text{H}(p, \gamma)^3\text{He}$  is at 5493 keV, it is necessary to extend the detection efficiency to higher energies. This is done by using the known resonance of  $^{27}\text{Al}(p, \gamma)^{28}\text{Si}$  at 992 keV. The efficiency for each detector is determined using a multi-parametric approach described in section 4.1.7.

### 4.1.5 $^{27}\text{Al}(\text{p}, \gamma)^{28}\text{Si}$

$^{27}\text{Al}$  captures a proton at the resonance energy,  $E_R = 992$  keV to form  $^{28}\text{Si}$  in the excited state with energy 12541.8 keV. The decay scheme from this level follows a very complicated process, with the dominant path being a decay into 1778.7 keV energy level releasing a  $\gamma$ -ray of energy 10762.9 keV followed by another photon of 1778.7 keV as  $^{28}\text{Si}$  falls to its ground state. These are the two prominent peaks of  $^{27}\text{Al}(\text{p}, \gamma)^{28}\text{Si}$ . But decays to other metastable states from the resonance states are possible, depending on the branching ratio and thus will result in a large number of  $\gamma$ -peaks along the energy range from 1778.9 keV to 10762.9 keV. A summary of some of the prominent peaks is shown in table 4.2, where r is the resonance energy state of  $^{28}\text{Si}$ . The  $\gamma$  spectra obtained

Table 4.2: Major  $\gamma$ -peaks of  $^{27}\text{Al}(\text{p}, \gamma)^{28}\text{Si}$ [43].

$E_\gamma$ (keV)	$E_i$ (keV)	$E_f$ (keV)	Branching Ratio
10762.9	r	1778.9	$76.6 \pm 1.5$
7933.4	7933.4	0	$3.7 \pm 0.4$
7924.0	r	4617.8	$4.3 \pm 0.4$
6019.9	7798.8	1778.9	$6.0 \pm 0.5$
4743	r	7798.8	$8.8 \pm 0.5$
4608.4	r	7933.4	$4.5 \pm 0.4$
4497.6	6276.5	1778.9	$4.8 \pm 0.3$
2838.9	4617.8	1778.9	$5.5 \pm 0.4$
1778.7	1778.9	0	$94.8 \pm 1.5$

for  $^{27}\text{Al}(\text{p}, \gamma)^{28}\text{Si}$  reaction at the resonance energy of 992 keV is shown in figure 4.7.

### 4.1.6 Net Counts from $\gamma$ spectra

As the activities of the radioactive sources are well-known, we can analyze the detector response to the emitted radiation over time to determine how efficient our detectors are. The recorded  $\gamma$  spectra are analyzed to get the net area counts of the  $\gamma$  peaks. This is done by taking the peak area and subtracting the background using the equation[44]:

$$A = \sum_{i=L}^U C_i - n \left( \sum_{i=L-m}^{L-1} C_i + \sum_{i=U+1}^{U+m} C_i \right) / 2m \quad (4.1)$$

where  $L$  and  $U$  are the lower and upper channels of the peak and  $C_i$  the counts for the  $i^{th}$  channel. The first term represents the peak counts, while the second term represents the subtraction of the background, which is done by averaging the background counts on either side of the peak for ' $m$ ' channels. The  $\gamma$ -peaks of all the radioactive sources are summarized below in figures 4.5 and 4.6.

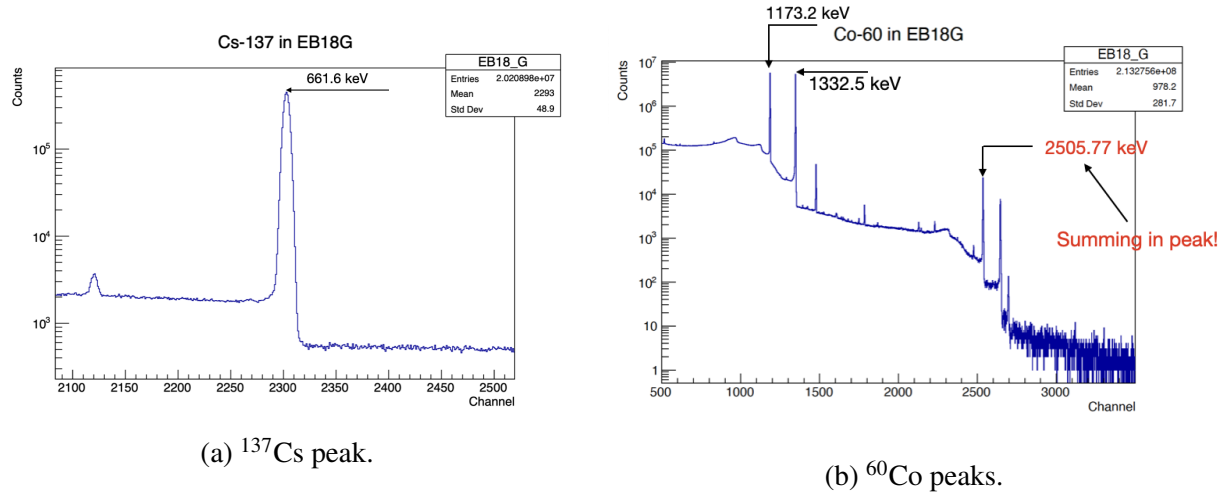


Figure 4.5:  $\gamma$ -peaks for  $^{137}\text{Cs}$  and  $^{60}\text{Co}$  in EB18G ( $90^\circ$ ) detector.

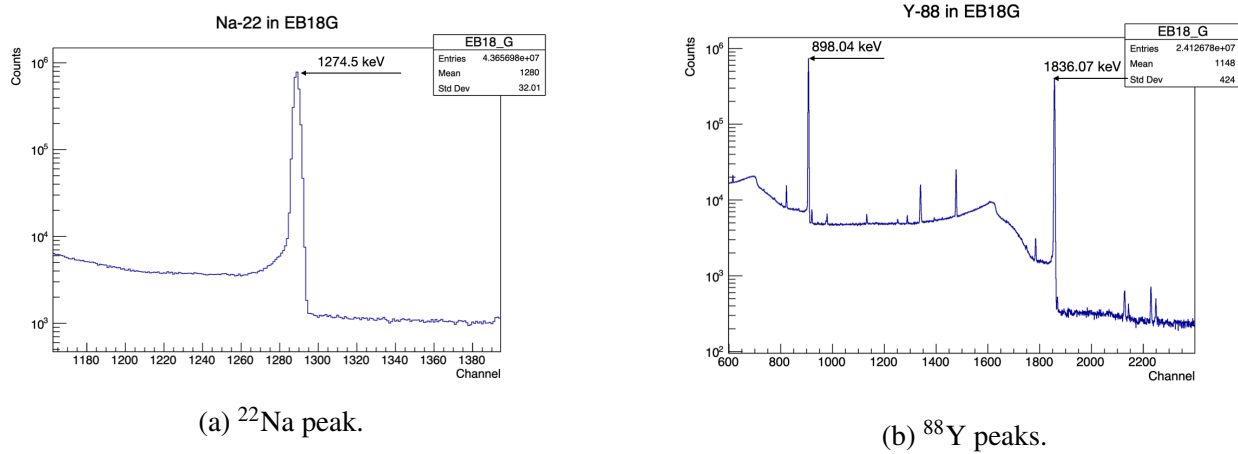


Figure 4.6:  $\gamma$ -peaks for  $^{22}\text{Na}$  and  $^{88}\text{Y}$  in EB18G ( $90^\circ$ ) detector.

### 4.1.7 Multi-Parametric Approach

The full-energy peak efficiency for a source like  $^{137}\text{Cs}$ , which emits only one  $\gamma$ -ray is given by

$$\eta_{ph}(E_i) = \frac{N(E_i)}{b_i At} \quad (4.2)$$

where  $N(E_i)$  is the number of counts of the  $\gamma$ -ray at energy  $E_i$ ,  $b_i$  is the branching ratio for the  $\gamma$ -ray,  $A$  is the activity of the radioactive source at the measurement time, and  $t$  is the acquisition time. Not all the sources decay emitting a mono-energetic  $\gamma$ -peak; very often the decay takes place through multiple excited states which introduces effects such as summing that should be taken into account.

For example, in the case of  $^{60}\text{Co}$  (Fig 4.5), we can see the effect of summing when the 1173.2 keV

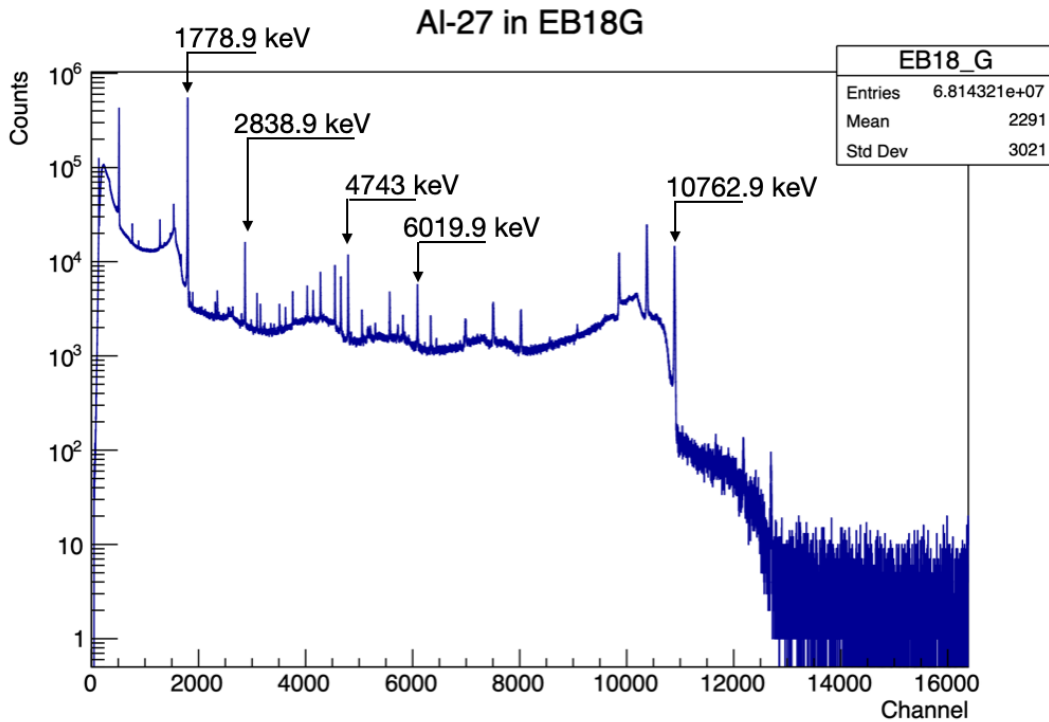


Figure 4.7:  $^{27}\text{Al}(\text{p}, \gamma)^{28}\text{Si}$  peaks obtained in the EB18G ( $90^\circ$ ) detector.

and 1332.5 keV arrive at the detector simultaneously. This causes a summing out of the  $\gamma$ -peaks at 1173.2 keV and 1332.5 keV and a summing in peak at 2505.77 keV.

To deal with the above effects, we need to parameterize the  $\gamma$ -rays adequately. The summing out and summing in effects reduce the number of counts at 1173.2 keV and 1332.5 keV respectively. Assuming the  $\gamma$ -peaks at 1173.2 keV and 1332.5 keV as  $E_{\gamma 1}$  and  $E_{\gamma 2}$  respectively, we can write the equations for the number of counts as

$$N(E_{\gamma 1}) = N_d b_1 \eta_{ph}(E_{\gamma 1}) (1 - b_2 \eta_{ph}(E_{\gamma 2})) \quad (4.3)$$

$$N(E_{\gamma 2}) = N_d b_1 b_2 \eta_{ph}(E_{\gamma 2}) (1 - \eta_{ph}(E_{\gamma 1})) \quad (4.4)$$

where  $N(E_{\gamma 1})$  and  $N(E_{\gamma 2})$  are the number of decays observed by the detector at  $E_{\gamma 1}$  and  $E_{\gamma 2}$  respectively,  $N_d$  is the number of decays given by  $N_d = At$ , where  $A$  is the activity and  $t$  is the time,  $b_1$  and  $b_2$  are the branching ratios for  $E_{\gamma 1}$  and  $E_{\gamma 2}$ ,  $\eta_{ph}$  is the photopeak efficiency and  $\eta_{tot}$  is the total efficiency.

To address these issues, we follow a multi-parametric approach to determine the detector efficiency, using the following system of equations that relate the photopeak energy,  $E_\gamma$  to the efficiency  $\eta$ .

$$\eta_{ph}(E_\gamma) = \exp [a + b \ln(E_\gamma) + c \ln^2(E_\gamma)] \quad (4.5)$$

$$\ln \left( \frac{\eta_{ph}}{\eta_{tot}} \right) = k_1 + k_2 \ln(E_\gamma) + k_3 \ln^2(E_\gamma) \quad (4.6)$$

where  $a, b, c, k_1, k_2$  and  $k_3$  are free parameters,  $\eta_{ph}$  is the photopeak efficiency, which we need to find,  $E_\gamma$  is the photopeak energy and  $\eta_{tot}$  is the total efficiency. The total efficiency refers to the ratio of total counts recorded in the spectrum above a threshold and the number of radiation quanta emitted by the source. Some incident quanta deposit their entire energy in the spectrum, corresponding to the observed sharp peak, while others deposit only a fraction of their energy giving rise to a continuum below the full-energy peak. The photopeak efficiency on the other hand is the ratio of counts recorded only in the full-energy peak and the number of quanta emitted by the source.

The steps followed in the multi-parametric approach are:

- Calculate the observed yield using the number of counts extracted from the  $\gamma$  spectra of the calibration sources.
- Make initial guesses for the free parameters and calculate the model yield using the equations 4.3, 4.4, 4.5 and 4.6.
- Fit the free parameters to minimize the  $\chi^2$  value.
- Using the final parameters, calculate the yield after summing corrections.

An important point to note is that for  $^{27}\text{Al}(\text{p}, \gamma)^{28}\text{Si}$ , instead of the number of decays  $N_d$ , we use resonance strength,  $R$ . This value is also assumed as a free parameter and fit through the  $\chi^2$  minimization. The results for the efficiency calibration for all the detectors are shown in section 4.1.8.

#### 4.1.8 Efficiency Calibration Results

We have used the  $\gamma$ -peaks of the radioactive sources and 4 of the peaks of  $^{27}\text{Al}(\text{p}, \gamma)^{28}\text{Si}$  (1778.9, 4743, 6019.9 and 10762.9) for the calibration. In addition, we also use the summing peak of  $^{60}\text{Co}$  at 2505.77 as well as the annihilation peak at 511 keV for the  $^{22}\text{Na}$  spectra. The  $^{88}\text{Y}$  peaks were not used for the calibration due to the  $\gamma$ -peaks being unstable as a result of the Al O-ring used in the target mount for  $^{88}\text{Y}$ . The efficiency curve obtained is shown in figures 4.9 to 4.14 as well as the free parameter values set after the  $\chi^2$  minimization. In figure 4.8, we plot the yield, which is the number of counts normalized to the accumulated charge and activity ( $\frac{N_c}{q*A}$ ) in the case of the radioactive sources and the number of counts normalized to the accumulated charge in case of  $^{27}\text{Al}(\text{p}, \gamma)^{28}\text{Si}$ . Figure 4.8 shows the observed yield, the model yield with the best-fit parameters and finally the yield after applying the summing corrections. A summary of the percentage change in efficiency due to summing effects is listed in table 4.3. The efficiency curves for all the detectors are shown in figures 4.9 to 4.14. From 4.3, the summing corrections applied can be seen. For  $^{60}\text{Co}$ , the summing out effect is highest for EB18G detector crystal at  $90^\circ$  as this detector is the closest to the target chamber (see table 3.1). On the other hand, EB17G shows the least summing corrections. The summing out effect for  $^{22}\text{Na}$  is caused by the coincidence of the 1274.55 keV photopeak with the 511 keV annihilation peak. The summing out effect seen for  $^{22}\text{Na}$  mirrors that seen for  $^{60}\text{Co}$ .

In figures 4.9 to 4.14, along with the efficiency curves, the efficiencies are also calculated without the summing corrections using

$$\eta = \frac{N_c}{A * t * b} \quad (4.7)$$

$N_c$  is the total peak counts, A is the activity of the source at the measurement time, t is the time of the data taking and b is the branching ratio. The plot shows the efficiencies before and after summing corrections.

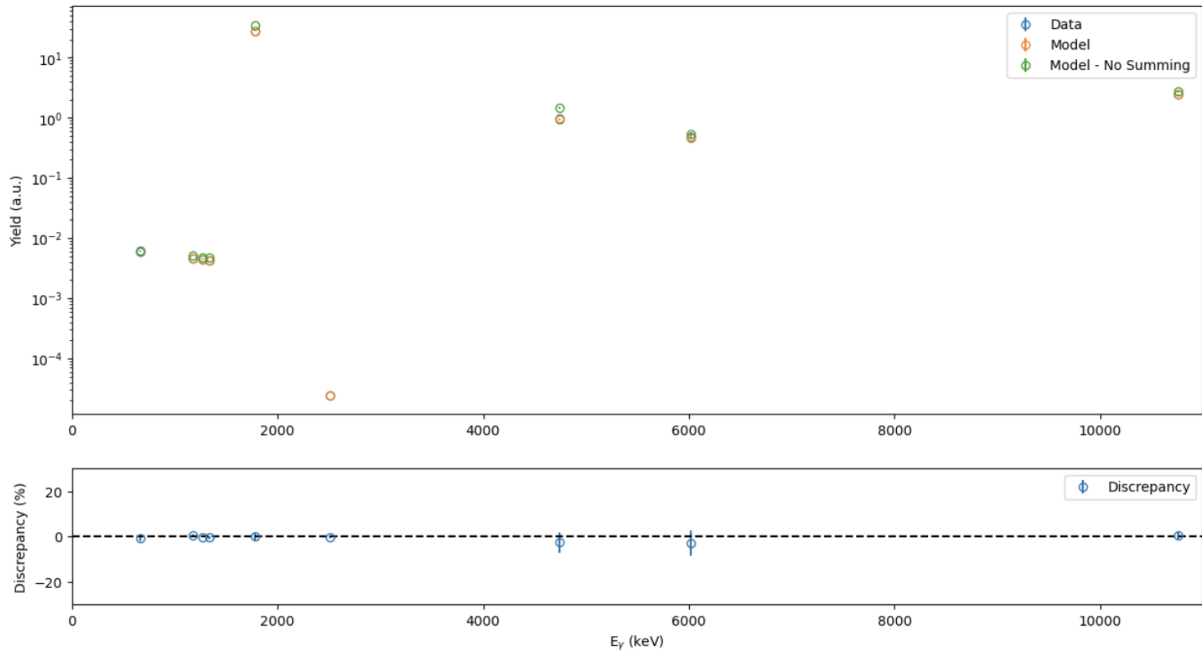
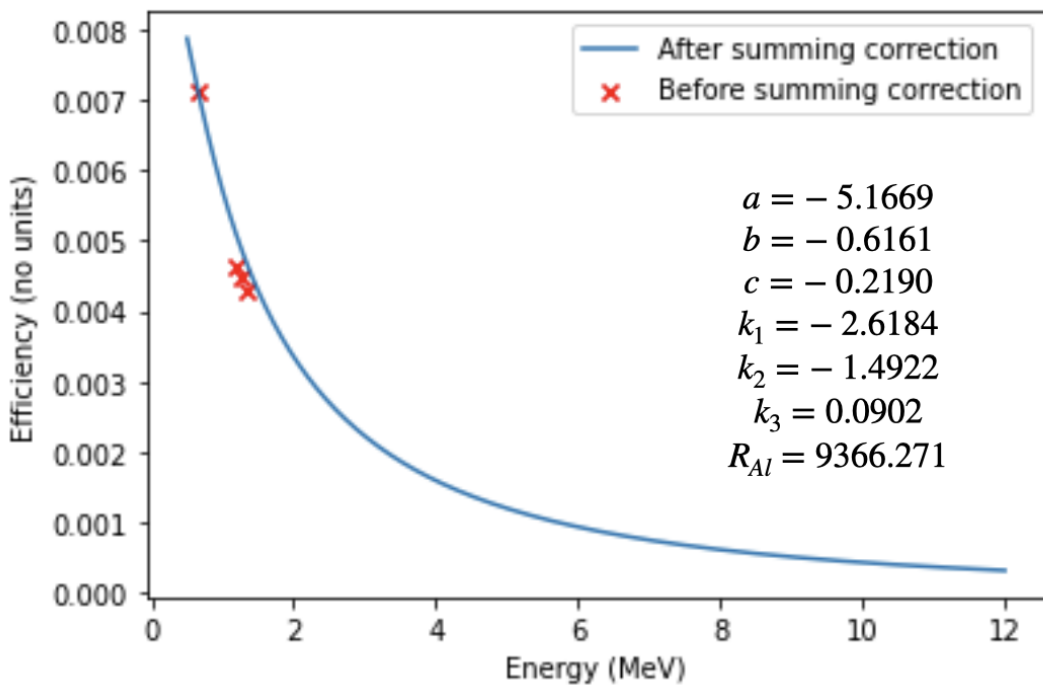
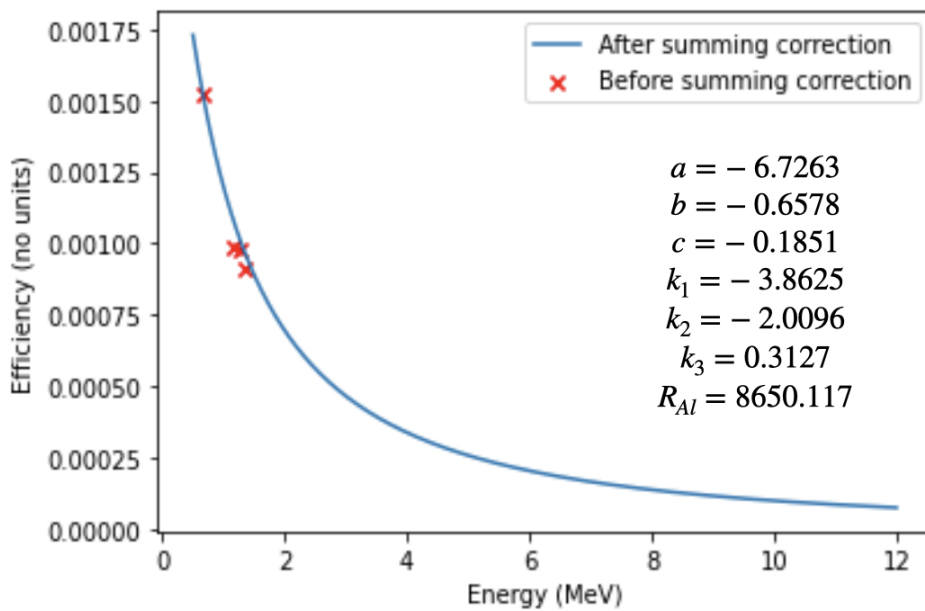


Figure 4.8: Experimental yield and residuals for EB18G ( $90^\circ$ ) detector. See details in the text (section 4.1.8).

Table 4.3: Summing corrections for all detectors for  $^{60}\text{Co}$  and  $^{22}\text{Na}$ .

E (in MeV)	EB18G (%)	Can60 (%)	Ron100 (%)	MB13 (%)	MB23 (%)	EB17G (%)
1.17323	11.2278	8.9542	7.9800	8.6708	12.1369	1.3977
1.27457	7.9641	3.4879	7.7436	8.7547	7.9330	0.0138
1.33249	9.3752	7.1968	9.0196	7.7732	10.6269	0.9977

Figure 4.9: Efficiency curve for EB18G ( $90^\circ$ ) detector.Figure 4.10: Efficiency curve for Can60 ( $89^\circ$ ) detector.

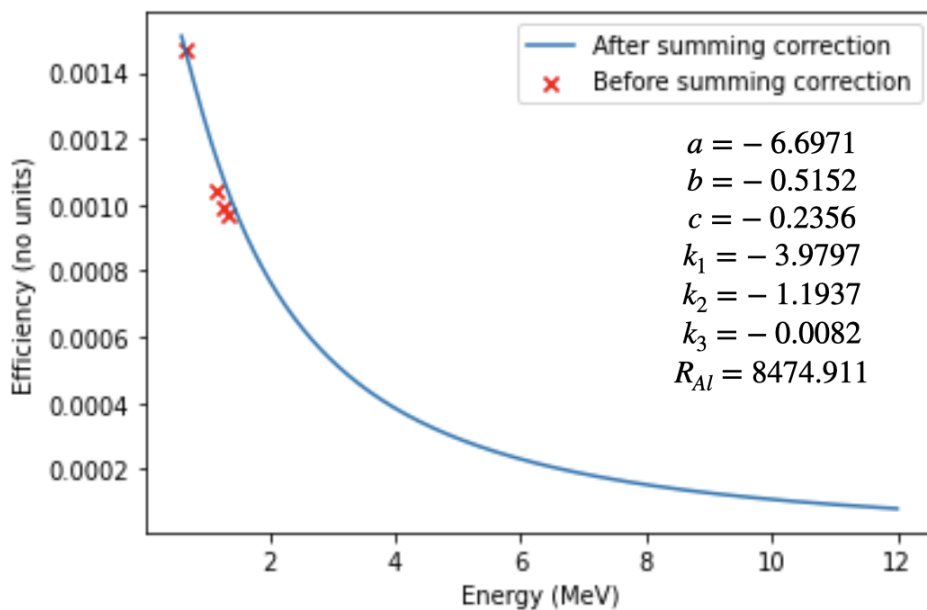


Figure 4.11: Efficiency curve for MB13 (118°) detector.

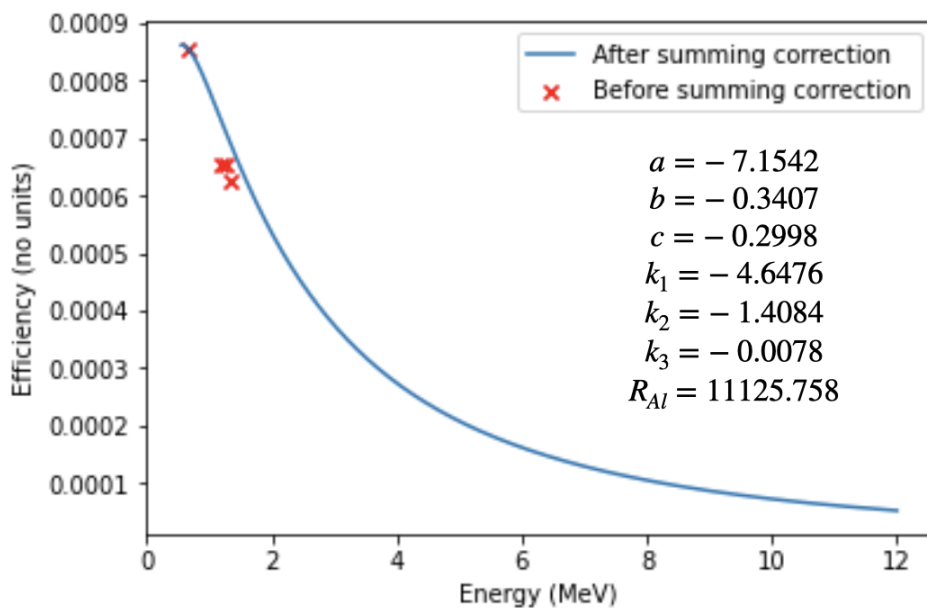


Figure 4.12: Efficiency curve for MB23 (36°) detector.

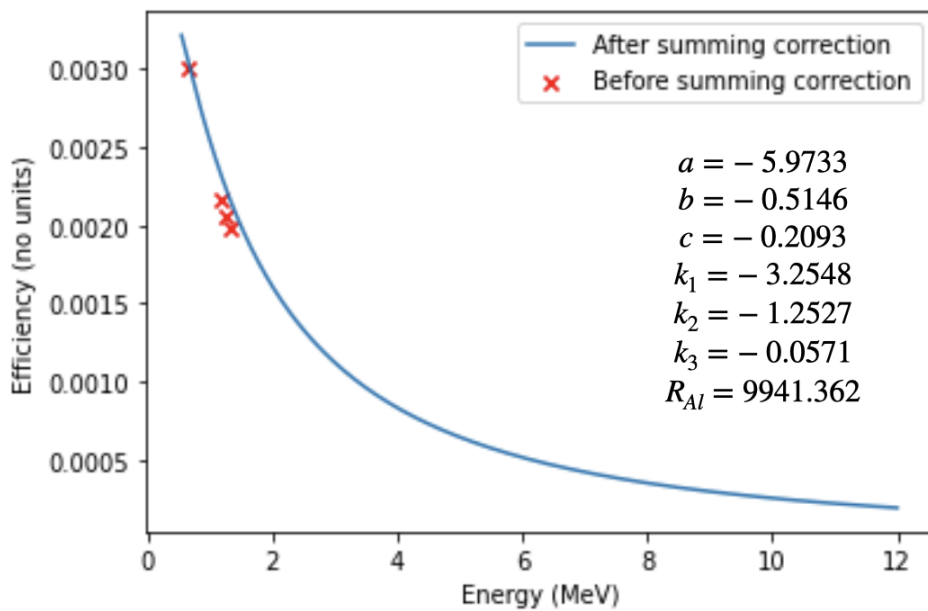


Figure 4.13: Efficiency curve for Ron100 (143.5°) detector.

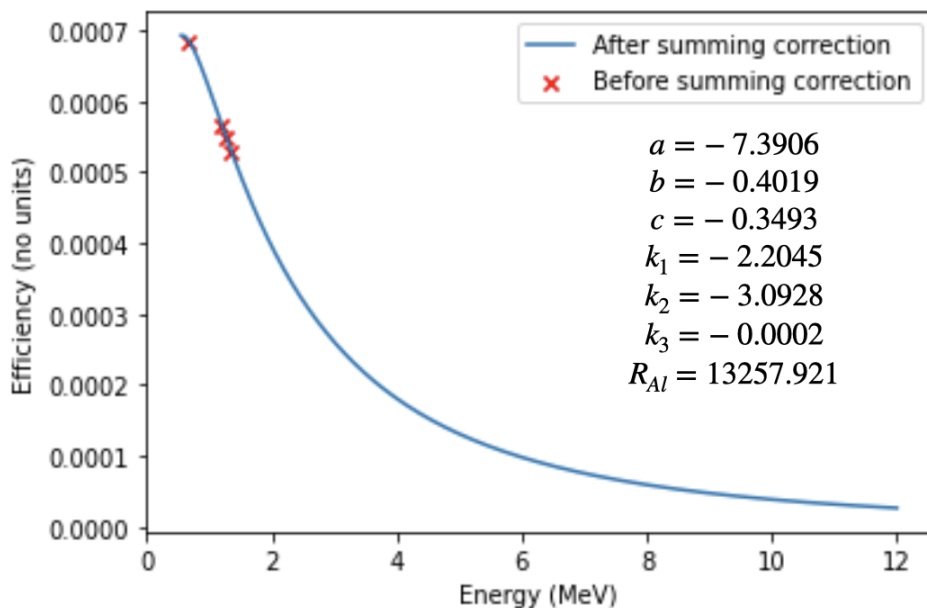


Figure 4.14: Efficiency curve for EB17G (39°) detector.

### 4.1.9 Doppler and Recoil Correction

The energy of the  $\gamma$ -ray released from the  ${}^2\text{H}(\text{p}, \gamma){}^3\text{He}$  is given by

$$E_\gamma = Q + \frac{m_D}{m_{He}} E + \Delta E_{doppler} - \Delta E_{recoil} \quad (4.8)$$

where  $Q = 5.493$  MeV,  $m_D$  and  $m_{He}$  are the masses of Deuterium and  ${}^3\text{He}$  respectively,  $E$  is the energy of the proton beam in the centre of mass frame,  $\Delta E_{doppler}$  is the change in energy due to the Doppler effect and  $\Delta E_{recoil}$  is the correction factor due to the recoil of the nucleus. The relativistic expression for the energy of the  $\gamma$  is given by

$$E_\gamma = \frac{Q(m_Hc^2 + m_Dc^2 + m_{He}c^2)/2 + m_Dc^2E}{m_Hc^2 + m_Dc^2 - E - \cos\theta\sqrt{E(2m_Hc^2 + E)}} \quad (4.9)$$

where  $\theta$  is the angle between the direction of the beam and the detector. For our arrangement of detectors, the expected energy,  $E_\gamma$  is reported below in table 4.4.

Table 4.4: Expected  $\gamma$ -peaks for the different detectors in units of keV.

$E_{lab}$ (keV)	$E_\gamma$ at $90^\circ$	$E_\gamma$ at $89^\circ$	$E_\gamma$ at $118^\circ$	$E_\gamma$ at $36^\circ$	$E_\gamma$ at $143.5^\circ$	$E_\gamma$ at $39^\circ$
300	5687.0	5687.8	5664.6	5726.1	5648.7	5724.5
350	5720.2	5721.1	5695.9	5762.7	5678.6	5760.0
400	5753.4	5754.4	5727.3	5799.1	5708.8	5797.3
500	5819.9	5821.0	5790.3	5871.6	5769.4	5869.5
608	5891.6	5892.9	5858.6	5949.4	5835.3	5947.1
700	5952.8	5954.1	5917.0	6015.4	5891.8	6012.9
800	6019.2	6020.6	5980.5	6087.0	5953.3	6084.3

## 4.2 Target Analysis

In the calculations performed to obtain the astrophysical S Factor (see section 4.3), the target thickness is an important parameter. The loss of energy within the target  $\Delta E$  (see section 4.3.3) is dependent on the target thickness. Therefore, an accurate estimation of the thickness is of paramount importance.

In this study, the target analysis of LNL\_125\_1 is performed using Elastic Recoil Detection Analysis (ERDA). The principle of ERDA is based on the elastic scattering of incident ions on a sample surface and detecting the recoiling sample atoms[45], typically in reflection geometry, as shown in figure 4.15. The stopper foil acts as a forward scatter veto, allowing only the recoiling light nuclei through which are then detected.

In the ERDA of LNL\_125\_1, a 35 MeV beam of  $\text{Cl}^{7+}$  ions is used to analyse the solid deuterium target. The angle between the sample normal and the incoming beam is  $70^\circ$ , and the scattering angle is  $30^\circ$ . The analysed area is about  $1.5 \times 2 \text{ mm}^2$ . The recoil atoms and scattered ions have

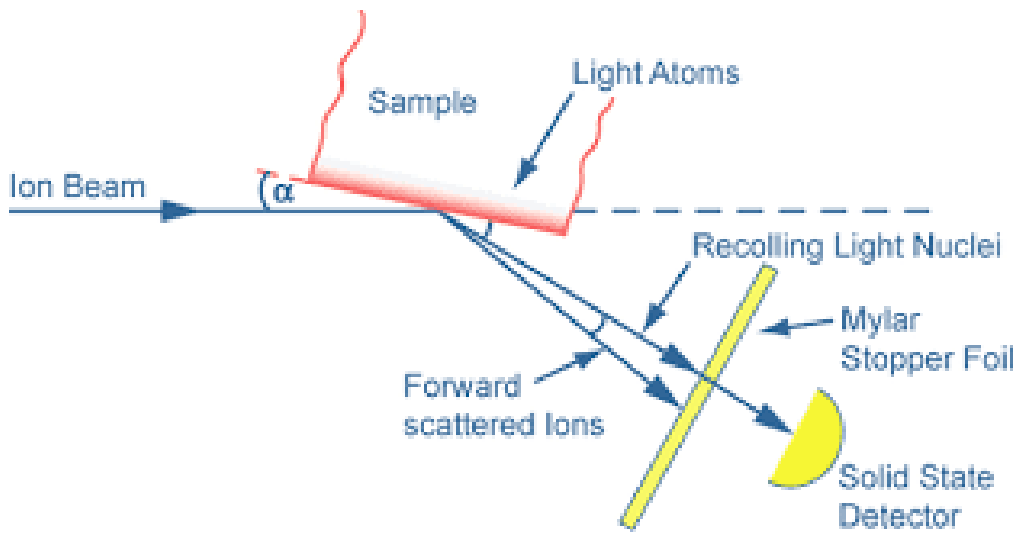


Figure 4.15: Schematic diagram of the ERDA geometry.

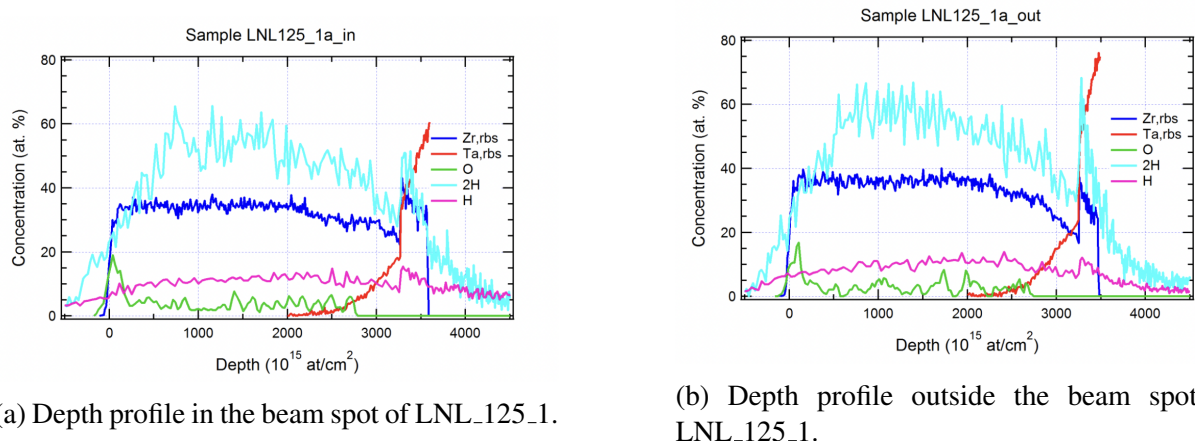


Figure 4.16: Depth profiles extracted from the measurements.

been detected with a Bragg Ionisation Chamber, which enables energy measurement and Z identification of the particles.  $^1\text{H}$  and  $^2\text{H}$  recoils have been detected with a separate solid-state detector at a scattering angle of  $40^\circ$ . This detector is preceded by a  $25\ \mu\text{m}$  Kapton foil to stop scattered ions and heavy recoil ions.

The depth profiles of the target are shown in figure 4.16. LNL\_125\_1a.in refers to the beam spot, while LNL\_125\_1a.out is 2 mm away from the beam spot. Table 4.5 displays the results of the ERDA of LNL\_125\_1. The thickness of deuterium is obtained by integrating the depth profiles.

Table 4.5: Depth Profile of and Deuterium thickness of LNL\_125\_1a.

Sample	Zr (%)	O (%)	D (%)	H (%)	D (in $10^{15}$ at/cm $^2$ )	H (in $10^{15}$ at/cm $^2$ )
LNL_125_1a_in	33.2	4.26	51.2	11.3	1810	484
LNL_125_1a_out	35.2	2.46	52.3	10.1	1850	384

## 4.3 S Factor

In the next step of the analysis, the astrophysical S-factor of the  ${}^2\text{H}(\text{p}, \gamma){}^3\text{He}$  reaction is calculated.

### 4.3.1 Calculation of Net Area

Similar to the calculations of the net peak area of the  $\gamma$  peaks in section 4.1.6, the areas for the  $\gamma$  peak for  ${}^2\text{H}(\text{p}, \gamma){}^3\text{He}$  is calculated. For the experiment, the proton beam energy was varied from 300 to 800 keV, while 608 keV was chosen as the reference energy run. This reference run was performed before and after each of the energy runs to understand the possible degradation of the targets by comparing the acquired yield.

An example for the  $\gamma$  spectra of  ${}^2\text{H}(\text{p}, \gamma){}^3\text{He}$  for EB18G detector ( $90^\circ$ ) and proton beam energy of 800 keV is shown in figure 4.17. While the Q value of the reaction is at  $Q = 5.493$  MeV, the photopeak in this spectra is shifted to higher energy due to the energy of the proton beam and Doppler and Recoil corrections mentioned in equation 4.9.

Additionally, the main sources of background besides the radioactive and muon background, are the beam-induced background produced by  ${}^{19}\text{F}(\text{p}, \alpha\gamma){}^{16}\text{O}$  reaction and other contaminants in the target or in the beamline path.  ${}^{19}\text{F}$  is present in the Tantalum backings used to prepare the deuterated targets and the  ${}^{19}\text{F}(\text{p}, \alpha\gamma){}^{16}\text{O}$  reaction has a resonance at 340 keV, producing the  $\gamma$  peak at 6.130 MeV along with the single and double escape peak. The escape peaks are also clearly visible in the spectrum.

Figure 4.17a also shows the peak of the  ${}^2\text{H}(\text{p}, \gamma){}^3\text{He}$  reaction in the EB18G ( $90^\circ$ ) detector. The peak area is calculated using the equation 4.1, considering the peak region as shown in figure 4.17b and the average background on either side of the peaks for 'm' channels.

This process is repeated for all the detectors, and each of the proton beam energies, ranging from 300 to 800 keV. Once all the net areas are obtained, we proceed to the next step which is the calculation of the yield.

### 4.3.2 Yield of ${}^2\text{H}(\text{p}, \gamma){}^3\text{He}$

Thermonuclear reaction cross-sections are not usually directly measured in the laboratory. Instead, we measure the reaction yield, defined as the ratio of the total number of reactions that occurred to the total number of incident beam particles.

$$Y = \frac{N_R}{N_b} \quad (4.10)$$

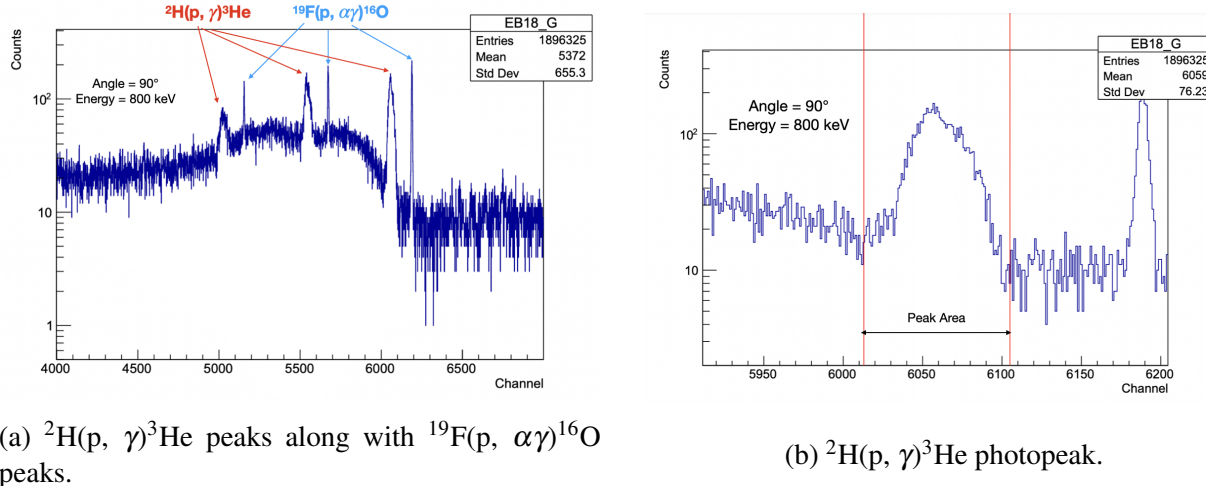


Figure 4.17: Two zoom in the region of interest for the gamma spectrum acquired at 800 keV with the EB18G ( $90^\circ$ ) detector. The region of interest is shown delimited in panel (b) and the fluorine peaks are underlined in panel (a).

Experimentally, we obtain the number of counts as explained in section 4.3.1. Thus, the experimental yield is given by:

$$Y = \frac{N_\gamma}{\eta q} \cdot q_e \quad (4.11)$$

where  $q_e = 1.6 \times 10^{-19}$  C is the elementary charge,  $N_\gamma$  is the number of counts in the peak,  $\eta$  is the efficiency of the EB18G detector and  $q$  is the accumulated charge expressed in coulombs (C).

Using 4.11 for all the detectors and the energy range of the proton beam, the reaction yield is calculated and they are shown for each of the detectors in figures 4.18 to 4.23. For a detailed discussion of the results, see chapter 5.

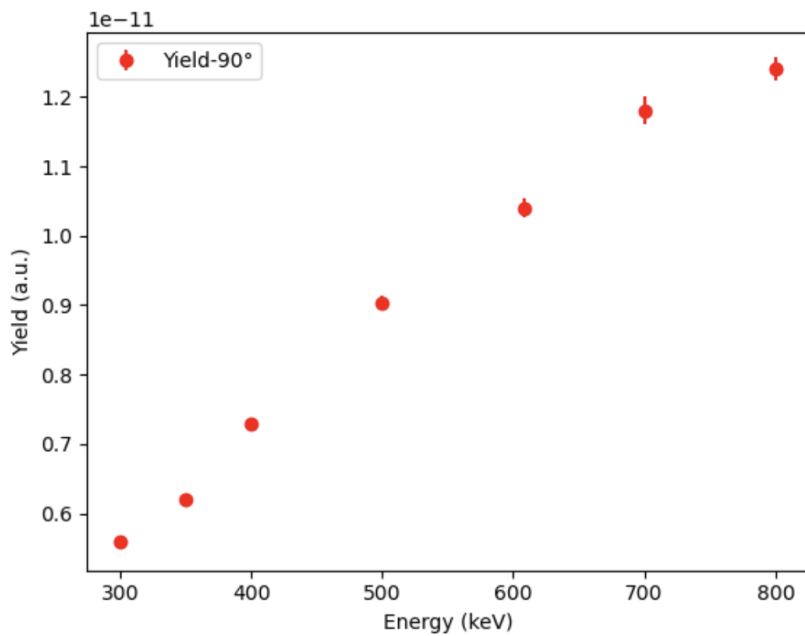


Figure 4.18: Yield for EB18G detector at  $90^\circ$ .

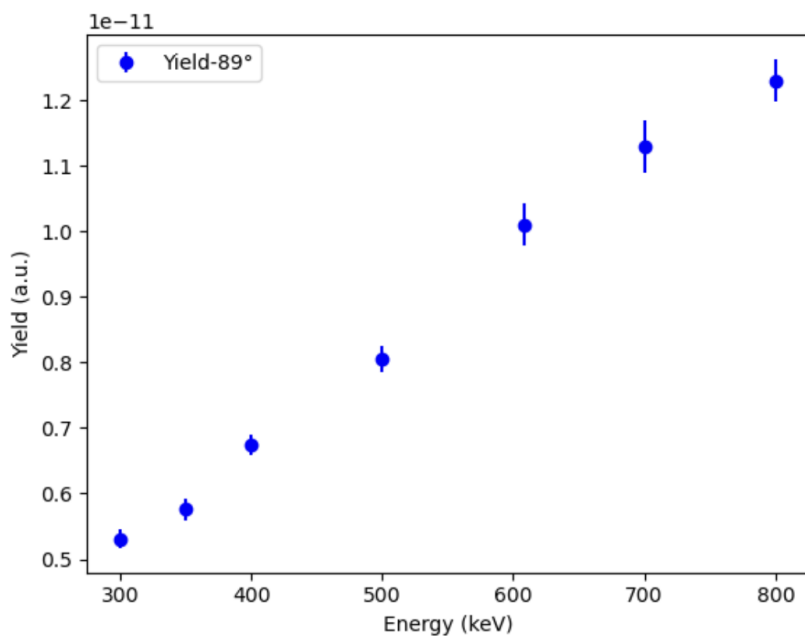


Figure 4.19: Yield for Can60 detector at  $89^\circ$ .

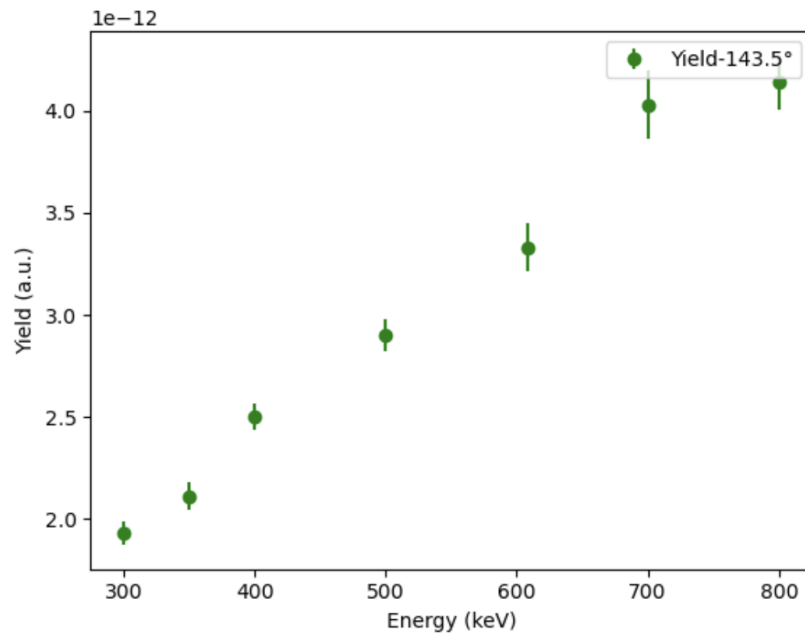


Figure 4.20: Yield for Ron100 detector at  $143.5^\circ$ .

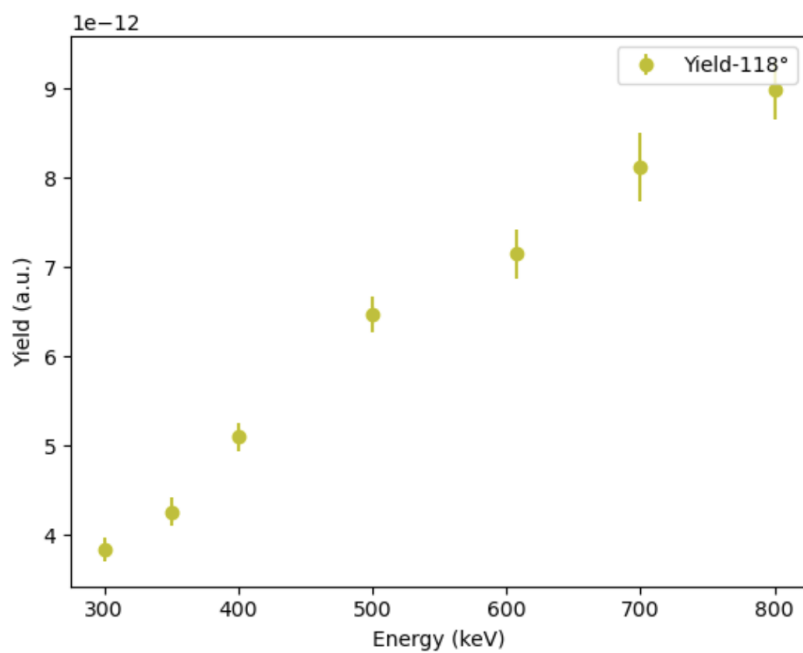
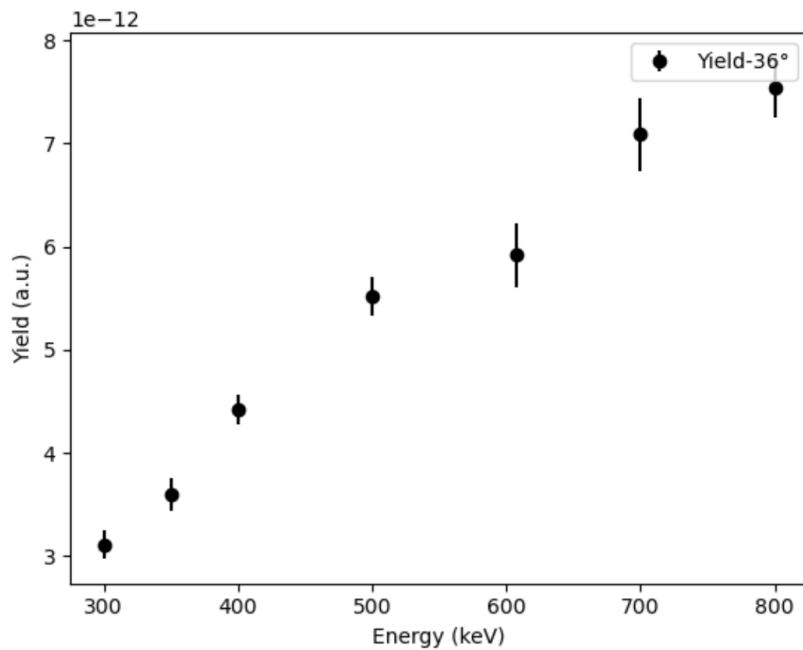
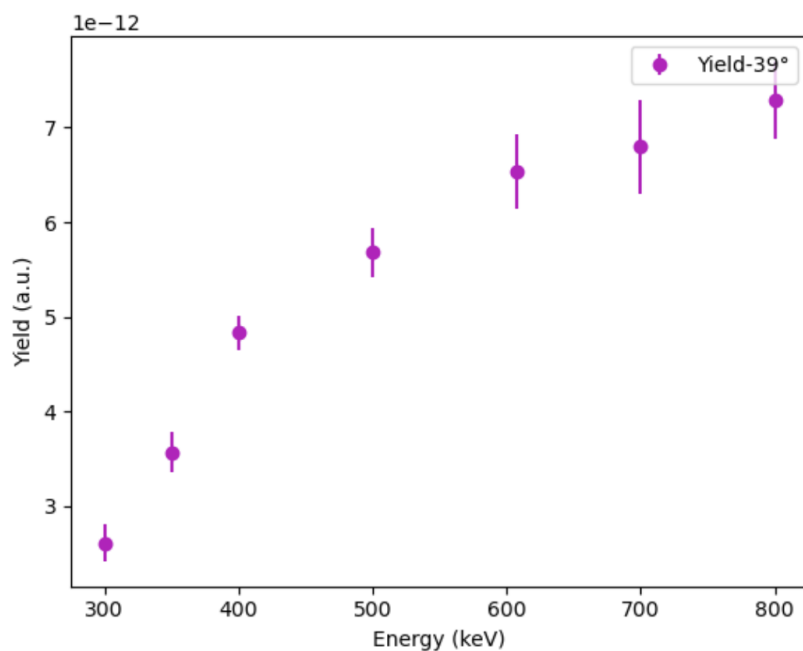


Figure 4.21: Yield for MB13 detector at  $118^\circ$ .

Figure 4.22: Yield for MB23 detector at  $36^\circ$ .Figure 4.23: Yield for EB17G detector at  $39^\circ$ .

### 4.3.3 Angular Correction of Yield

Although the detectors are placed at different angles, they still cover only a part of the total solid angle. Therefore, the yield needs to be corrected for the angular distribution. The angular correction term,  $W(\theta)$  is a function of the sum of Legendre Polynomials[46] and is given by

$$W(\theta) = 1 + \frac{1}{a_0} \sum_l a_l P_l(\cos\theta_{CM}) \quad (4.12)$$

where  $P_l$  is the  $l^{th}$  Legendre polynomial. In this work we assumed values from the theory and the  $a_i$  are the best-fit coefficients obtained from theoretical calculations of the  ${}^2\text{H}(p, \gamma){}^3\text{He}$  reaction by Marcucci et al[38].

$\theta_{CM}$  is defined as follows

$$\cos\theta_{CM} = \frac{\cos\theta_{lab} - \beta}{1 - \beta\cos\theta_{lab}} \quad (4.13)$$

where  $\beta = v/c$  and  $\theta_{lab}$  is the position of the detectors in the laboratory frame. The velocity of the beam is obtained from the energy of the proton beam used. To compute  $W(\theta)$ , the first 5 Legendre polynomials are used here and are defined as follows

$$P_l(\cos\theta_{CM}) = \begin{cases} 1 & l = 0 \\ \cos\theta_{CM} & l = 1 \\ \frac{1}{2}(3\cos^2\theta_{CM} - 1) & l = 2 \\ \frac{1}{2}(5\cos^3\theta_{CM} - 3\cos\theta_{CM}) & l = 3 \\ \frac{1}{8}(35\cos^4\theta_{CM} - 30\cos^2\theta_{CM} + 3) & l = 4 \end{cases} \quad (4.14)$$

The coefficients  $a_i$  in equation 4.16 obtained from [38] are listed below in table 4.6.

Table 4.6: Coefficients for Legendre Polynomials  $a_i$ .

E (keV)	$a_0$	$a_1$	$a_2$	$a_3$	$a_4$
300	116.235	6.402	-109.619	-5.949	-0.075
350	132.923	7.934	-126.335	-7.465	-0.119
400	149.147	9.472	-142.462	-8.983	-0.141
500	176.949	12.576	-170.363	-12.121	-0.213
608	204.877	16.22	-198.501	-15.704	-0.285
700	227.357	21.187	-220.936	-20.644	-0.51
800	249.451	25.142	-243.009	-24.614	-0.666

Using equation 4.14, the angular correction  $W(\theta)$  is computed and summarised in table 4.7. Finally, the yield obtained in section 4.3.2 is corrected for the angular distribution by

$$Y_{corr}(E, \theta) = \frac{Y(E, \theta)}{W(\theta)} \quad (4.15)$$

Table 4.7: Angular Correction factor  $W(\theta)$  for all energies for each detector.

Energy (keV)	W(90°)	W(89°)	W(143.5°)	W(118°)	W(36°)	W(39°)
300	1.4685	1.4713	0.5062	1.0934	0.5992	0.6756
350	1.4716	1.4747	0.4984	1.0886	0.6003	0.6778
400	1.4735	1.4769	0.4925	1.0842	0.6020	0.6802
500	1.4762	1.4801	0.4819	1.0753	0.6060	0.6857
608	1.4781	1.4825	0.4716	1.0661	0.6112	0.6920
700	1.4777	1.4829	0.4593	1.0515	0.6218	0.7041
800	1.4776	1.4832	0.4516	1.0427	0.6280	0.7112

### 4.3.4 Calculation of S Factor

The Yield of the reaction and the cross-section are related by the equation,

$$Y_{corr} = \int_{E_0 - \Delta E}^{E_0} \frac{\sigma(E)}{\epsilon_{eff}(E)} dE \quad (4.16)$$

where  $\epsilon_{eff}(E)$  is the effective stopping power of the target material. Stopping power is used to describe the slowing down of the projectile through the target as a result of collisions. Since this is quite small, it is described as an average energy loss in the target. For this study, the target used is LNL\\_125\\_1 ( $ZrD_2$ ). The effective stopping power is defined as

$$\epsilon_{eff} = \epsilon_H + \frac{1}{2}\epsilon_{Zr} \quad (4.17)$$

where  $^2H$  is the active nuclei while  $Zr$  is the inactive nuclei that do not participate in the reaction. The term  $\Delta E$  is the loss of energy through the target and is a function of the target thickness and the total stopping power

$$\Delta E = t * \epsilon_{tot}(E) \quad (4.18)$$

where  $t$  is the thickness and the total stopping power  $\epsilon_{tot}(E)$ , is defined as

$$\epsilon_{tot}(E) = \frac{2\epsilon_H + \epsilon_{Zr}}{3} \quad (4.19)$$

It is important to note that the yield in equation 4.16 is the angular corrected yield defined in equation 4.15 and for the remainder of this work, the angular corrected yield will be denoted by  $Y_{corr}$ . Recalling 1.20, equation 4.16 can be rewritten in terms of S Factor as

$$Y_{corr} = \int_{E_0 - \Delta E}^{E_0} \frac{1}{E} \frac{S(E)e^{-2\pi\eta}}{\epsilon_{eff}(E)} dE \quad (4.20)$$

Since the loss of energy within the target is small ( $\sim$  few keV), and the astrophysical S Factor for a non-resonant process is a weak function of energy, the S Factor can be approximated as a constant

in the energy range  $E_0 - \Delta E$  to  $E_0$ . It can be taken out of the integral. Now, rearranging equation 4.20 for the S Factor,

$$S(E) = \frac{Y_{corr}}{\int_{E_0 - \Delta E}^{E_0} \frac{1}{E} \frac{e^{-2\pi\eta}}{\epsilon_{eff}(E)} dE} \quad (4.21)$$

But, there is a loss of energy of the proton beam amounting to  $\Delta E$ . The energy  $E_0$  corresponds to the energy of the beam at the surface of the target while  $E_0 - \Delta E$  is the energy at the full depth of the target. Therefore, for an accurate estimation, the effective energy  $E_{eff}$  is defined [47]. Figure 4.24, shows the variation of the cross-section  $\sigma(E)$  with the energy. The shaded part represents the target at various depths, with  $E_p$  corresponding to the surface and  $E_p - \Delta E_p$  corresponding to the maximum depth, which is also the thickness of the target. Defining the corresponding cross-sections, we have  $\sigma(E_p)$  and  $\sigma(E_p - \Delta E_p)$  at both the respective energies. Effective energy,  $E_{eff}$  is defined as the energy at which the cross-section becomes

$$\sigma_{eff} = \left( \frac{\sigma(E_p) + \sigma(E_p - \Delta E_p)}{2} \right) \quad (4.22)$$

The expression of  $E_{eff}$  is defined as

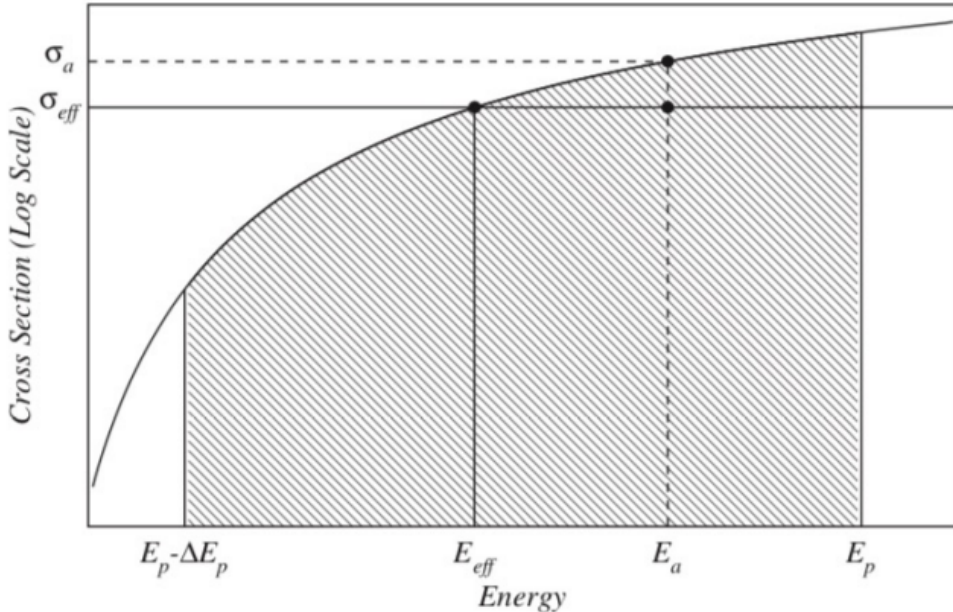


Figure 4.24: Variation of  $\sigma(E)$  w.r.t. the energy.

$$E_{eff} = \frac{\int_{E_p - \Delta E_p}^{E_p} \sigma(E) E dE}{\int_{E_p - \Delta E_p}^{E_p} \sigma(E) dE} \quad (4.23)$$

Substituting 1.20, we get

$$E_{eff} = \frac{\int_{E_p - \Delta E_p}^{E_p} e^{-2\pi\eta} dE}{\int_{E_p - \Delta E_p}^{E_p} \frac{e^{-2\pi\eta}}{E} dE} \quad (4.24)$$

The S Factor terms cancel out based on the assumption that it is a constant over the small energy range  $E_p - \Delta E_p$  to  $E_p$ . The results obtained for the S Factor for the different detectors are shown in figures 4.25 to 4.30 and summarised in table 4.8.

Table 4.8: Astrophysical S Factor all energies for each detector. Uncertainties are also shown (systematic + statistical).

$E$ (keV)	$S(90^\circ)$ (eV b)	$S(89^\circ)$ (eV b)	$S(143.5^\circ)$ (eV b)	$S(118^\circ)$ (eV b)	$S(36^\circ)$ (eV b)	$S(39^\circ)$ (eV b)
191.5	3.10 (4)	2.94 (8)	3.11 (9)	2.86 (10)	4.26 (18)	3.16 (23)
225.6	3.52 (10)	3.27 (10)	3.52 (12)	3.27 (12)	5.00 (22)	4.40 (27)
259.5	4.19 (10)	3.87 (9)	4.29 (11)	3.99 (12)	6.21 (21)	6.01 (22)
327.0	5.46 (14)	4.86 (12)	5.34 (15)	5.36 (17)	8.10 (28)	7.37 (34)
399.7	6.66 (21)	6.48 (20)	6.72 (24)	6.37 (24)	9.22 (48)	8.98 (54)
461.4	7.92 (28)	7.57 (27)	8.76 (36)	7.70 (37)	11.37 (56)	9.64 (70)
528.4	8.86 (24)	8.79 (23)	9.71 (31)	9.11 (33)	12.69 (49)	10.89 (61)

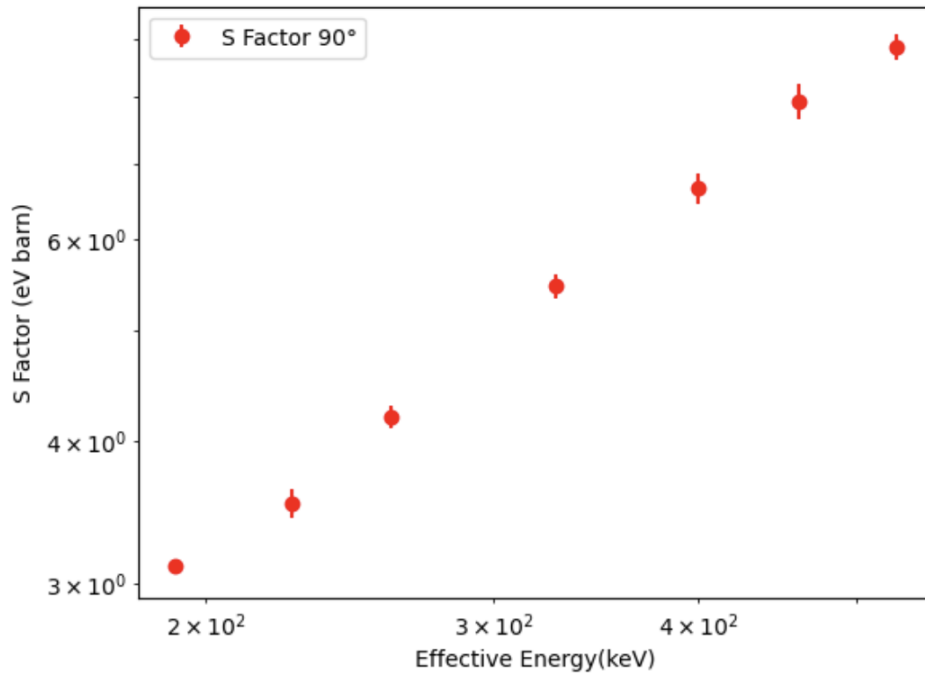


Figure 4.25: S Factor for EB18G detector at  $90^\circ$ . Uncertainty of 1 to 3.5% for the energy range.

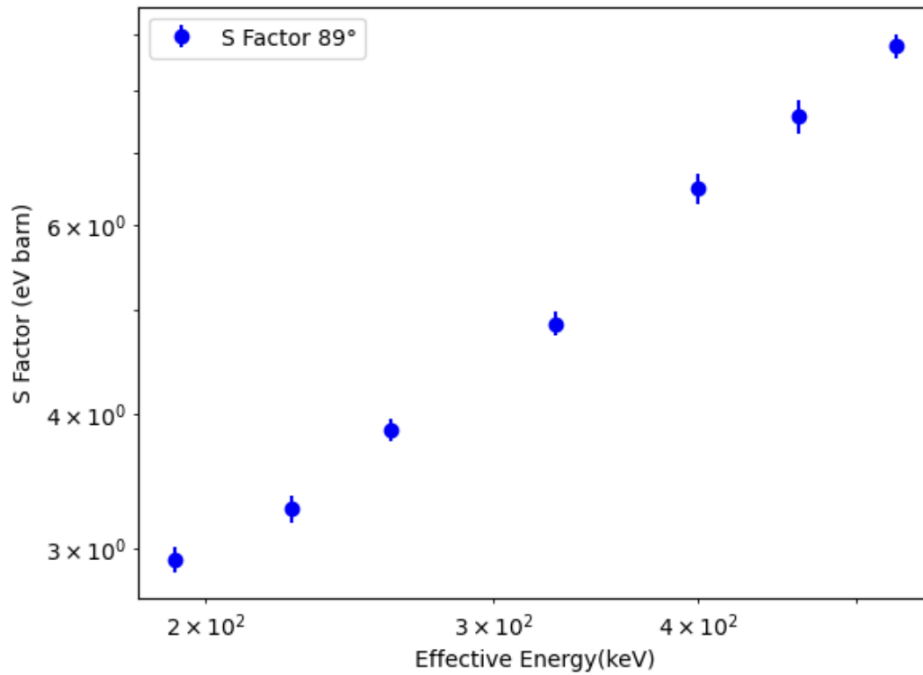


Figure 4.26: S Factor for Can60 detector at 89°. Uncertainty of 2 to 3.5% for the energy range.

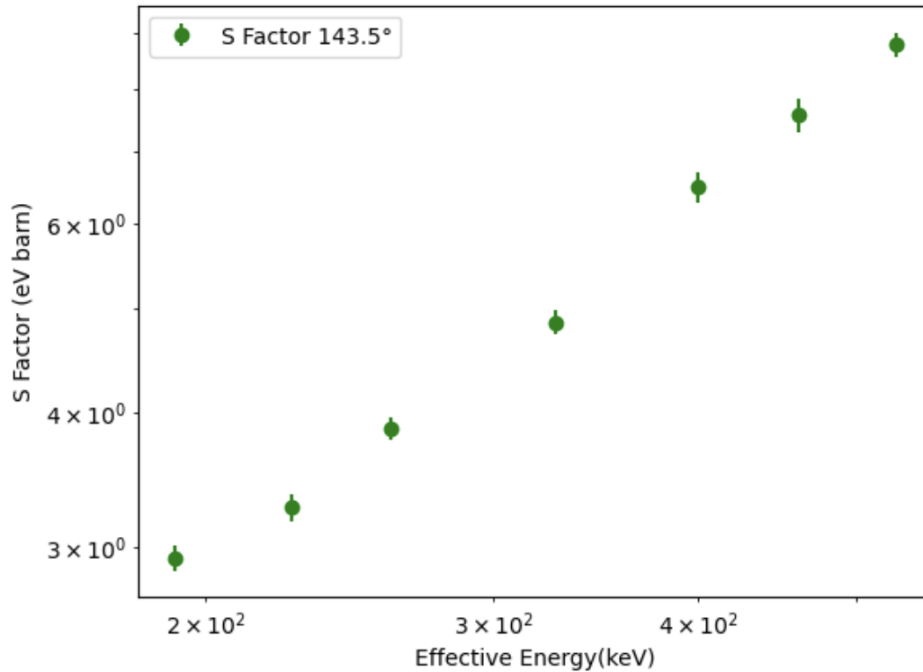


Figure 4.27: S Factor for Ron100 detector at 143.5°. Uncertainty of 3 to 4% for the energy range.

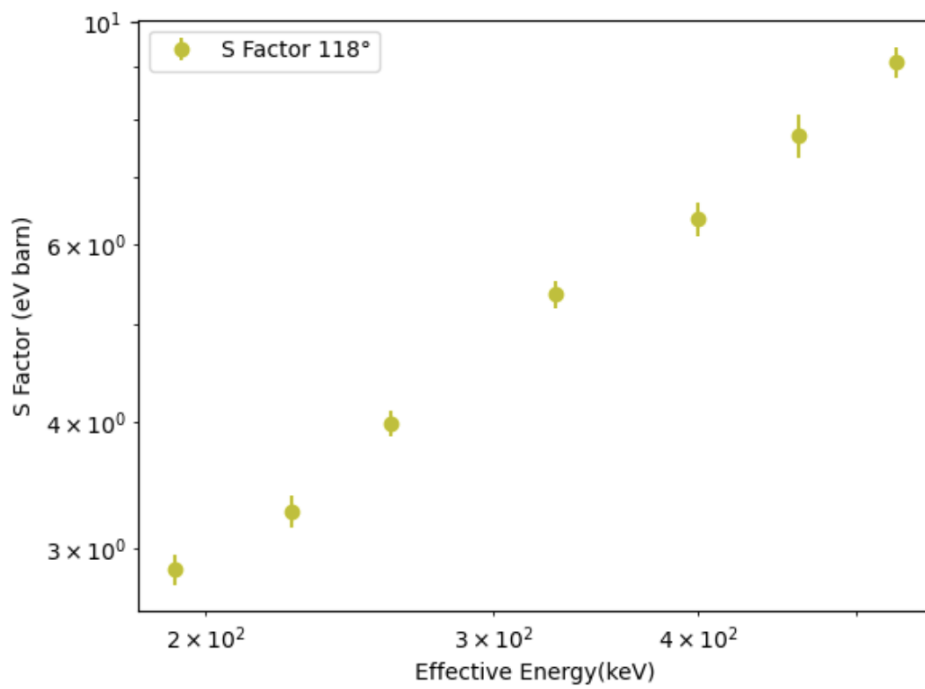


Figure 4.28: S Factor for MB13 detector at  $118^\circ$ . Uncertainty of 3 to 5% for the energy range.

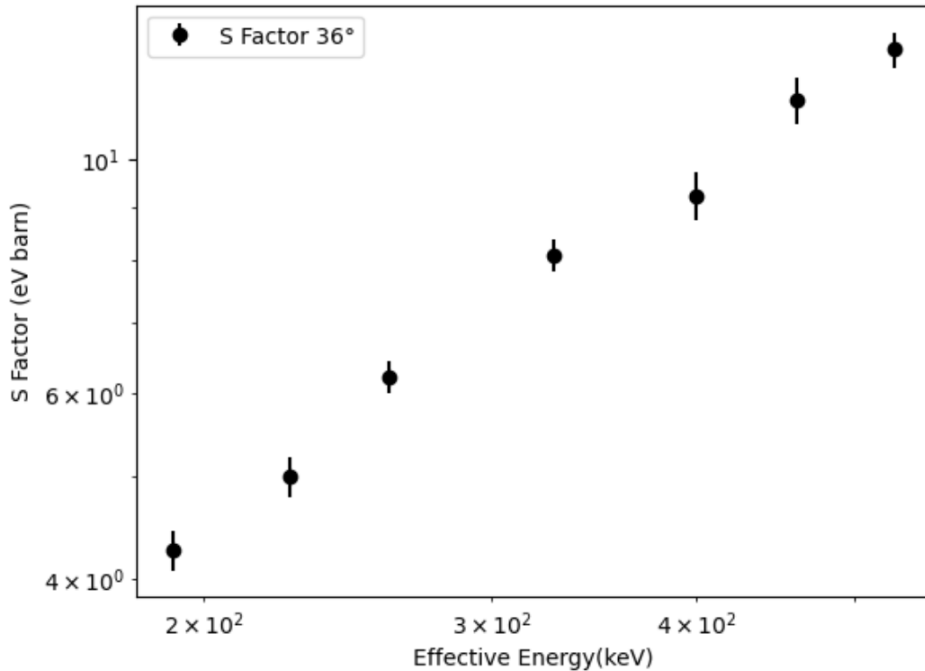


Figure 4.29: S Factor for MB23 detector at  $36^\circ$ . Uncertainty of 3 to 5% for the energy range.

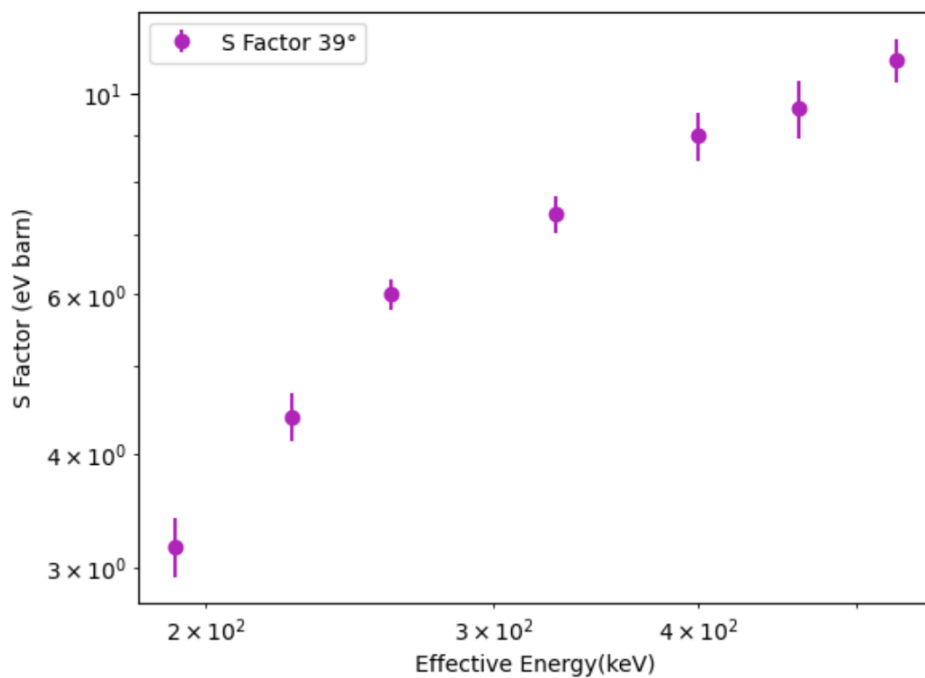


Figure 4.30: S Factor for EB17G detector at  $39^\circ$ . Uncertainty of 3 to 7.5% for the energy range.

# Chapter 5

## Results and Discussion

In this chapter the results of the  $^2\text{H}(\text{p}, \gamma)^3\text{He}$  campaign at Felsenkeller will be summarized. First, the detector characterization will be discussed, followed by the S Factor calculation with the target LNL\_125\_1. The results will also be compared with LUNA data[39] in the BBN range and the high-energy extrapolation, as well as with the high-energy measurement at HZDR[40].

### 5.1 Efficiency

A combined plot of the efficiencies for all the detectors is shown in figure 5.1. EB18G at 90° shows the highest efficiency as expected since the detector is also the closest to the target chamber.

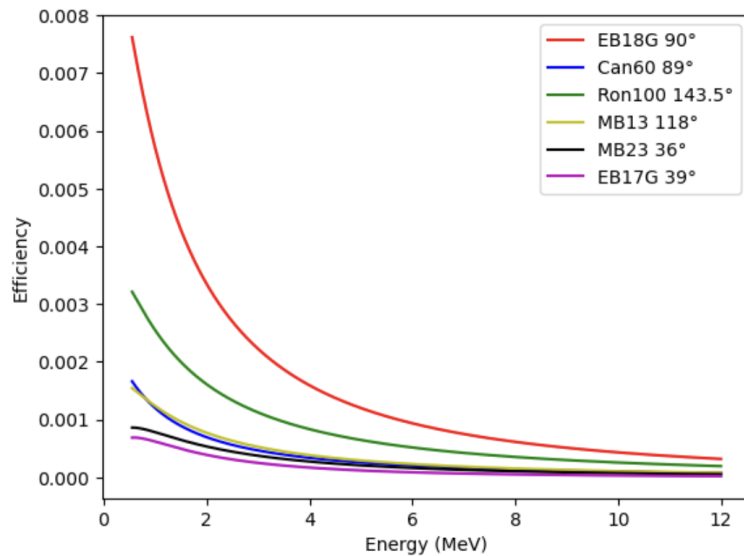


Figure 5.1: Summary of efficiency plots for all detectors.

The contribution to the systematic error during the detector characterization step is  $\approx 2 - 5\%$ .

## 5.2 Angular Distribution of Yield

Here, the angular distribution of the yield for the reference energy of 608 keV is shown in figure 5.2 using all the detectors.

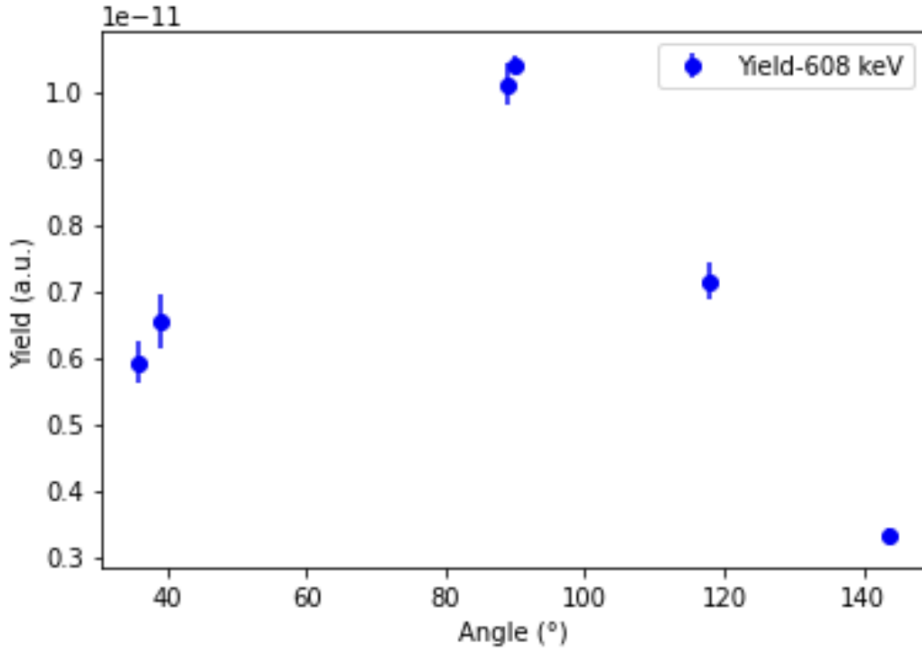


Figure 5.2: Angular distribution of yield at 608 keV.

The results obtained for the angular distribution for the Felsenkeller  ${}^2\text{H}(\text{p}, \gamma){}^3\text{He}$  campaign is concurrent with results from literature[48]. As expected, the highest yield is obtained at  $90^\circ$  while the values decrease rapidly at lower angles.

## 5.3 S Factor

The S factor obtained for the  ${}^2\text{H}(\text{p}, \gamma){}^3\text{He}$  reaction is shown in figure 5.3 for all the detectors.

The values for the S Factor are summarized in table 4.8 along with the uncertainties. EB17G ( $39^\circ$ ) has the highest uncertainty (max error  $\approx 7 - 8\%$ ), which is predominantly statistical (error in counts). With the exception of EB18G at 300 keV lab energy (uncertainty  $\approx 1.2\%$ ), EB18G ( $90^\circ$ ), Can60 ( $89^\circ$ ) and Ron100 ( $143.5^\circ$ ) have similar uncertainties in the range 2 to 4% over the energy range. MB13 ( $118^\circ$ ) and MB23 ( $36^\circ$ ) show a slightly higher uncertainty in the range of 3 to 5%. The main contributors to the uncertainty are

- Counts (statistical)
- Efficiency of detectors (systematic)

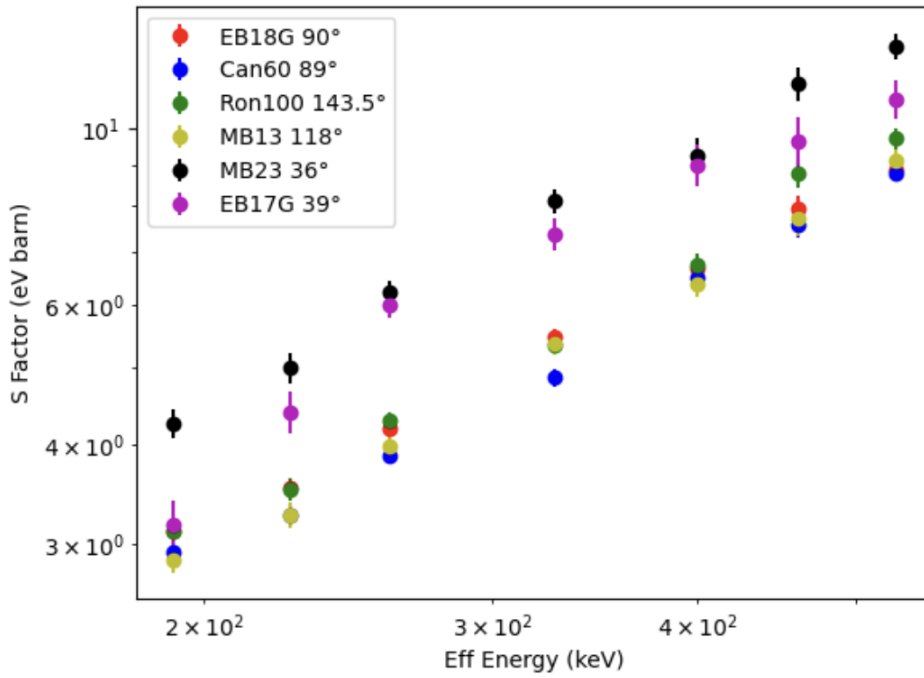


Figure 5.3: Summary of S Factors for all detectors.

- Beam current (systematic)

The uncertainty in the target density is not considered for the preliminary data analysis presented in this thesis. In addition, there are minor contributions to the statistical uncertainty from the calculation of the angular correction coefficients ( $W$ ) and numerical integration for the S Factor, but these are too small and therefore ignored in this analysis.

In summary, the S Factor values obtained for EB18G ( $90^\circ$ ), Can60 ( $89^\circ$ ), Ron100 ( $143.5^\circ$ ) and MB13 ( $118^\circ$ ) are in good agreement with each other. MB23 ( $36^\circ$ ) has an S Factor value higher by a factor of  $\approx 1.5$ , which could be a result of the mispositioning of the detector which could cause an error in the detector characterization. The experimental setup is implemented in Geant4 and checks with simulations are ongoing which is beyond the scope of this thesis. EB17G shows an erratic trend due to the high statistical uncertainty (7%) caused by the counting error. Further analysis considering all 6 crystals of the EB17 is ongoing and this will surely decrease the statistical uncertainty.

### 5.3.1 Comparison with LUNA and HZDR

For the comparison, the S Factor of EB18G ( $90^\circ$ ), Can60 ( $89^\circ$ ), Ron100 ( $143.5^\circ$ ) and MB13 ( $118^\circ$ ) are considered. The S Factors for each of the 4 detectors are compared with LUNA and HZDR results in figures 5.4 to 5.7. The discrepancies for the detectors are summarised in tables 5.1 to 5.3.

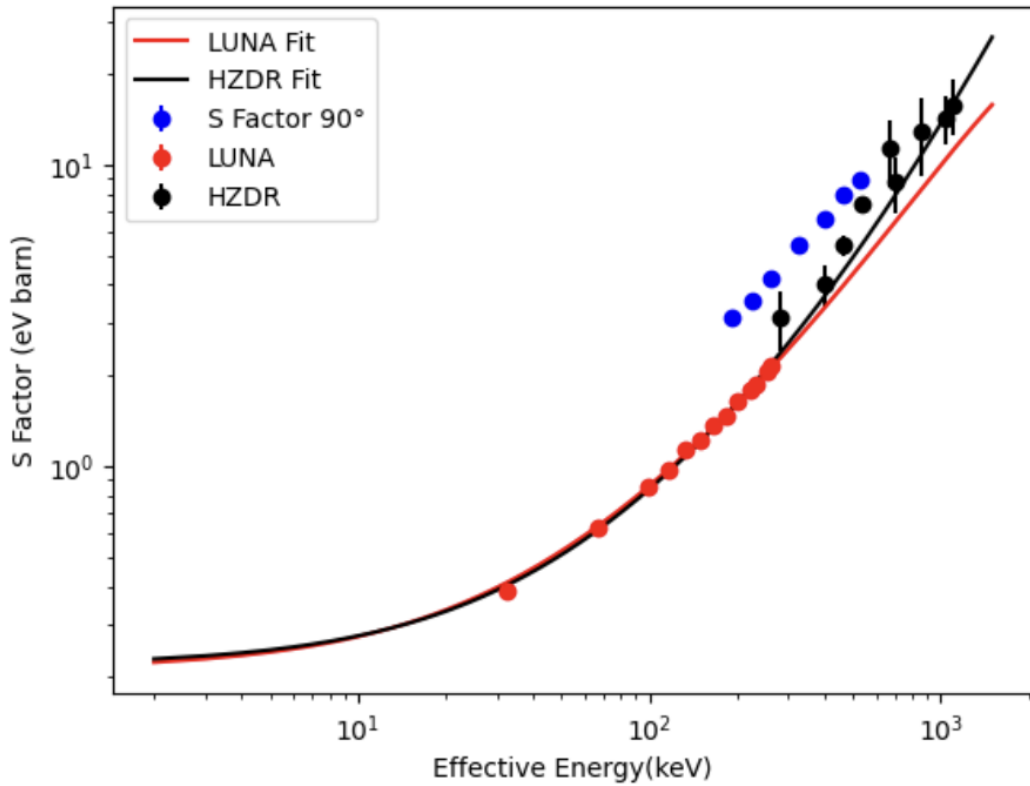


Figure 5.4: S Factor obtained for EB18G ( $90^\circ$ ) detector in comparison to LUNA and HZDR data and fit.

Table 5.1: EB18G detector ( $90^\circ$ ): S factor and discrepancy with LUNA and HZDR S factor fits.

$E_{eff}(\text{keV})$	$S(90^\circ)(\text{b})$	$\frac{\Delta S}{S_{LUNA}}$	$\frac{\Delta S}{S_{HZDR}}$
191.5	3.10 (4)	1.01	1.00
225.6	3.52 (10)	0.94	0.91
259.5	4.19 (10)	1.00	0.94
327.0	5.46 (14)	1.03	0.92
399.7	6.66 (21)	0.98	0.81
461.4	7.93 (28)	1.00	0.79
528.4	8.86 (24)	0.91	0.66

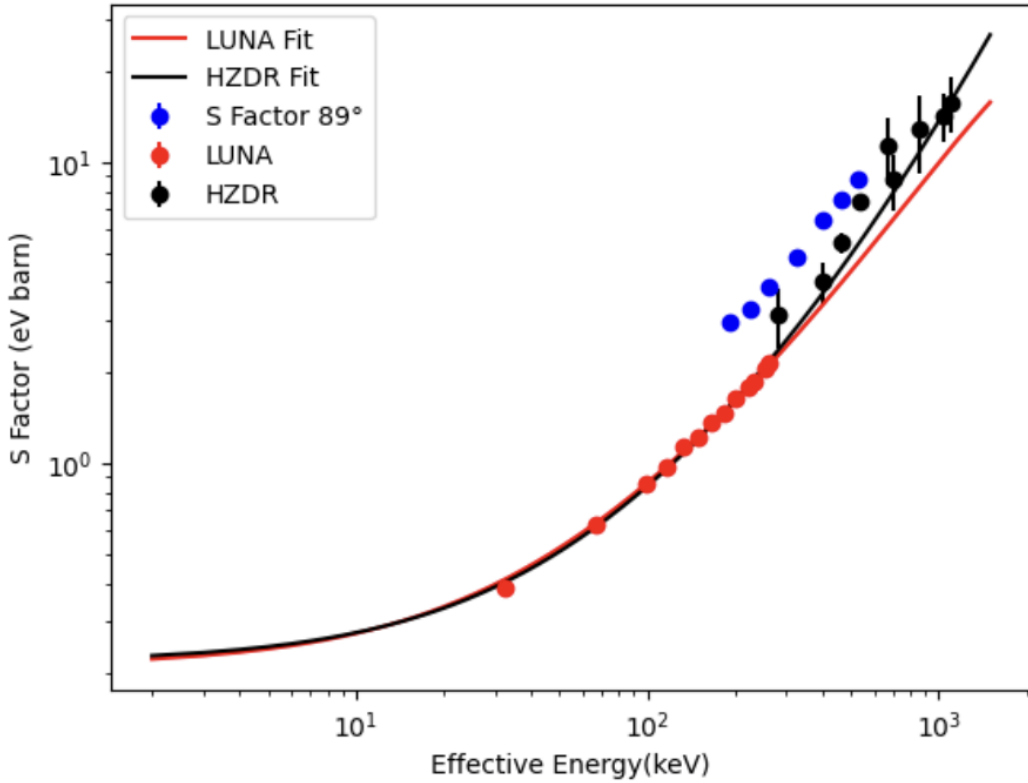


Figure 5.5: S Factor obtained for Can60 ( $89^\circ$ ) detector in comparison to LUNA and HZDR data and fit.

Table 5.2: Can60 detector ( $89^\circ$ ): S factor and discrepancy with LUNA and HZDR S factor fits.

$E_{eff}(\text{keV})$	$S(89^\circ)(\text{b})$	$\frac{\Delta S}{S_{LUNA}}$	$\frac{\Delta S}{S_{HZDR}}$
191.5	2.94 (8)	0.90	0.89
225.6	3.27 (10)	0.80	0.77
259.5	3.87 (9)	0.84	0.79
327.0	4.86 (12)	0.80	0.70
399.7	6.48 (20)	0.92	0.76
461.4	7.57 (27)	0.91	0.71
528.4	8.79 (23)	0.89	0.65

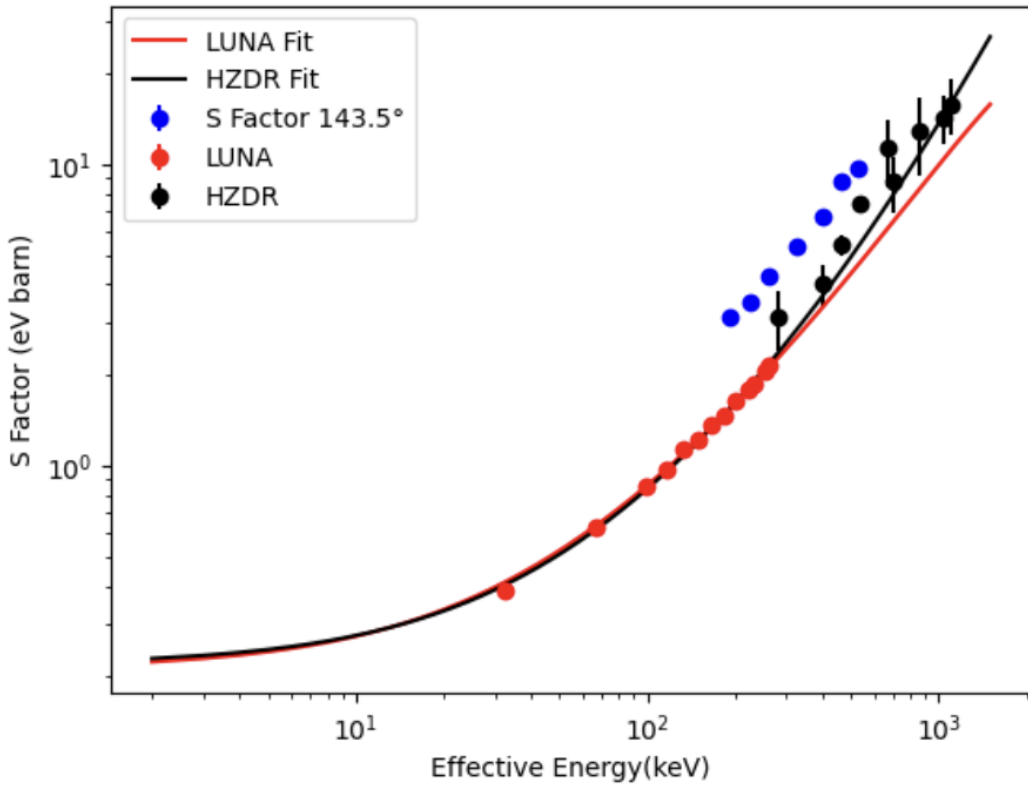


Figure 5.6: S Factor obtained for Ron100 ( $143.5^\circ$ ) detector in comparison to LUNA and HZDR data and fit.

Table 5.3: Ron100 detector ( $143.5^\circ$ ): S factor and discrepancy with LUNA and HZDR S factor fits.

$E_{eff}(\text{keV})$	$S(143.5^\circ)(\text{b})$	$\frac{\Delta S}{S_{LUNA}}$	$\frac{\Delta S}{S_{HZDR}}$
191.5	3.11 (9)	1.02	1.01
225.6	3.52 (12)	0.93	0.90
259.5	4.29 (11)	1.04	0.98
327.0	5.34 (15)	0.99	0.88
399.7	6.72 (24)	1.00	0.83
461.4	8.76 (36)	1.21	0.98
528.4	9.71 (31)	1.09	0.82

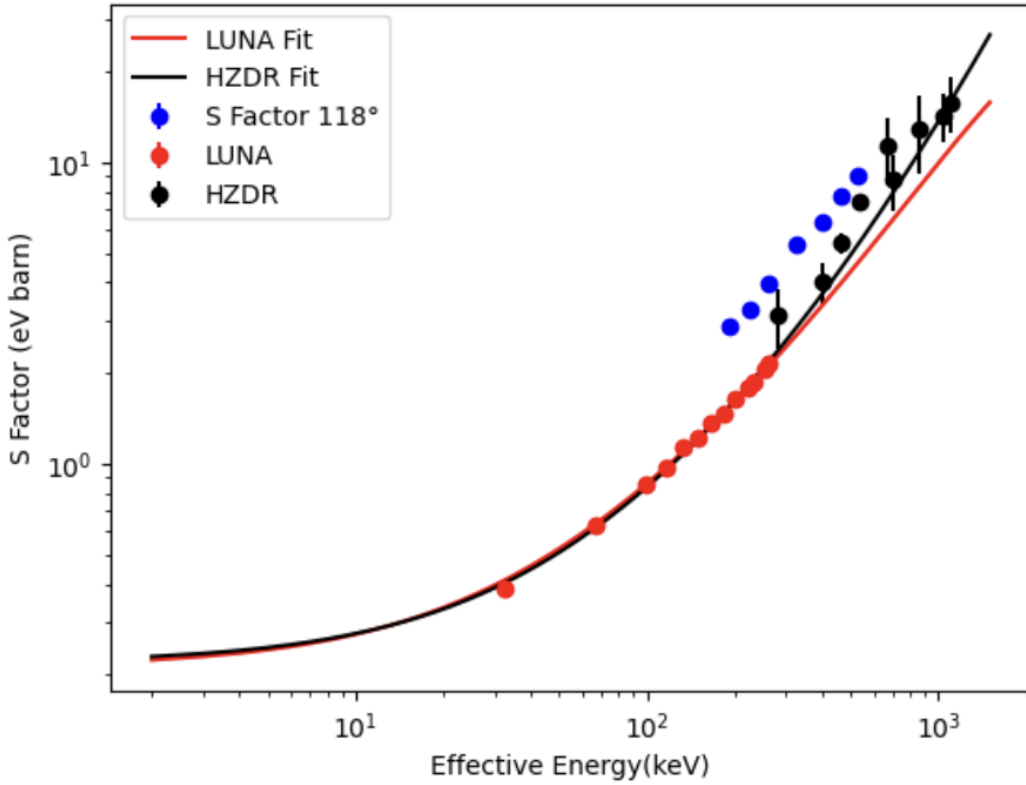


Figure 5.7: S Factor obtained for MB13 ( $118^\circ$ ) detector in comparison to LUNA and HZDR data and fit.

Table 5.4: MB13 detector ( $118^\circ$ ): S factor and discrepancy with LUNA and HZDR S factor fits.

$E_{eff}(\text{keV})$	$S(118^\circ)(\mathbf{b})$	$\frac{\Delta S}{S_{LUNA}}$	$\frac{\Delta S}{S_{HZDR}}$
191.5	2.86 (10)	0.85	0.84
225.6	3.27 (12)	0.80	0.77
259.5	3.99 (12)	0.90	0.84
327.0	5.36 (17)	0.99	0.88
399.7	6.37 (24)	0.89	0.74
461.4	7.70 (37)	0.94	0.74
528.4	9.11 (33)	0.96	0.71

Except for a few outlier points, the discrepancies with the LUNA fit data are constant in the range of 0.8 to 1, for each of the 4 detectors in the energy range of interest. This could result from the miscalibration of the targets which would affect the target thickness obtained from ERDA. Compared to the HZDR data points, the results obtained at Felsenkeller are less scattered and the trend of the preliminary S factor obtained is quite uniform, in spite of the normalisation factor. The

errors obtained are also quite low when compared to the HZDR measurement. This suggests a possible systematic discrepancy with the target. Additional analysis on target comparing different ERDA and other techniques is ongoing and this should clarify the discrepancies on the S Factor presented in this preliminary analysis.

# Conclusions

The  $^2\text{H}(\text{p},\gamma)^3\text{He}$  reaction plays an important role in the BBN. For several years this reaction has been studied in different energy ranges. Very recently the reaction has been studied directly in the BBN energy range at LUNA and later at higher energies at HZDR.

The S factor fits from these two data sets are in agreement at lower energies while a 10% discrepancy at higher energies is shown. Therefore, new experimental data on the  $^2\text{H}(\text{p},\gamma)^3\text{He}$  reaction in a wide energy range able to overlap with both data sets would be crucial.

Here the  $^2\text{H}(\text{p},\gamma)^3\text{He}$  reaction was studied at Felsenkeller laboratory, Dresden in the energy range from 300 to 800 keV using a solid target setup. The product of the reaction was measured with 22 crystals mounted at different positions around the target.

The efficiency calibration of the setup was done using standard sources and the well-known resonance of the  $^{27}\text{Al}(\text{p},\gamma)^{28}\text{Si}$  reaction was used to extend the calibration to higher energies.

The preliminary astrophysical S factor with a statistical uncertainty of 2-8% depending on the detector was presented.

A preliminary comparison with the literature data shows a higher S factor data. This is mostly due to the target density which is still under analysis and here only preliminary data are used.

Furthermore, the use of different detectors at different angles allows for the first time to measure the angular distribution of this reaction which can affect the microphysics of the reaction.

The updated values of the S factor for the  $^2\text{H}(\text{p},\gamma)^3\text{He}$  reaction will help to improve the determination of the primordial deuterium abundance. Further studies can be conducted to constrain the baryon density at higher precision using BBN theory, independent of CMB calculations.

# Bibliography

- [1] C. E. Rolfs and W. S. Rodney, Cauldrons in the Cosmos (The University of Chicago Press, 1988).
- [2] A. Finn, Fundamental University Physics (Addison-Wesley Publishing Company, 1968).
- [3] P. Marigo, Lectures of Advanced Astrophysics, University of Padova, 2021.
- [4] E. Masha, Big Bang Nucleosynthesis and the deuterium abundance: study of the  $^2\text{H}(\text{p},\gamma)^3\text{He}$  reaction in the energy range 400-800 keV, MSc Thesis, Uinversità degli studio di Milano, 2018.
- [5] F. Iocco et al., Phys. Rep. 472, 1 (2009). <https://doi.org/10.48550/arXiv.0809.0631>
- [6] S. Weinberg, Gravitation and Cosmology, John Wiley and Sons (1972).
- [7] W. Yao et al., J. Phys. 33, 1232 (2006). <https://iopscience.iop.org/article/10.1088/0954-3899/33/1/001>
- [8] S. Materrese, Lectures on Fundamentals of Astrophysics and Cosmology, University of Padova (2021).
- [9] Planck Collaboration (2020). "Planck 2018 results. VI. Cosmological parameters". Astronomy Astrophysics. 641 (2020). <https://doi.org/10.1051%2F0004-6361%2F201833910>
- [10] G. Steigman, Annu. Rev. Nucl. Part. Sci. 57, 463 (2007). <https://doi.org/10.48550/arXiv.0712.1100>
- [11] B. Ryden, Introduction to cosmology (Addison-Wesley, 2003).
- [12] M. Roos, Introduction to Cosmology (John Wiley & Sons, Ltd, 2003).
- [13] Evan Grohs and George M. Fuller, Big Bang Nucleosynthesis (2023). <https://doi.org/10.48550/arXiv.2301.12299>
- [14] G. Steigman et al., Phys. Lett. B 66, 202 (1977). [https://doi.org/10.1016/0370-2693\(77\)90176-9](https://doi.org/10.1016/0370-2693(77)90176-9)
- [15] F.M. Gonzalez et al. (UCN  $\tau$  Collaboration), Improved Neutron Lifetime Measurement with UCN  $\tau$  (2021). <https://doi.org/10.1103/PhysRevLett.127.162501>

- [16] S. Weinberg, Cosmology (Oxford University Press, 2008).
- [17] J. Lesgourges et al., Adv. High Energy Phys. 2012, 608515 (2012). <https://doi.org/10.1155/2012/608515>
- [18] V. Mossa, Study of the  $^2\text{H}(\text{p},\gamma)^3\text{He}$  reaction in the Big Bang nucleosynthesis energy range, PhD dissertation, Università degli studi di Bari Aldo Moro, 2018.
- [19] E.O. Zavarygin and A.V. Ivanchik, J. Phys.: Conf. Ser. 661 012016 (2015). <https://doi.org/10.1088/1742-6596/661/1/012016>
- [20] J. Willis, University of Victoria, Lectures on Big Bang Nucleosynthesis.
- [21] C.A. Bertulani et al., Cosmological Lithium Problems (2018). <https://doi.org/10.48550/arXiv.1802.03469>
- [22] S. Gariazzo et al., PArthENoPE Revolutions (2021). <https://doi.org/10.48550/arXiv.2103.05027>
- [23] R.J. Cooke et al., One Percent Determination of the Primordial Deuterium Abundance (2018). <https://doi.org/10.48550/arXiv.1710.11129>
- [24] B.L. Berman et al., Phys. Rev 133, B117-B129 (1964). <https://doi.org/10.1103/PhysRevC.10.2221>
- [25] J.R. Stewart et al., Phys. Rev 138, B372 (1965). <https://doi.org/10.1103/PhysRev.138.B372>
- [26] V.N. Fetisov et al., Nucl. Phys. 71, 305-342 (1965). [https://doi.org/10.1016/0029-5582\(65\)90720-0](https://doi.org/10.1016/0029-5582(65)90720-0)
- [27] G. Griffiths et al., Can. J. Phys. 40, 402 (1962). <https://doi.org/10.1139/p62-045>
- [28] G. Griffiths et al., Can. J. Phys. 40, 402 (1963). <https://doi.org/10.1139/p63-077>
- [29] G. Bailey et al., Can. J. Phys. 48, 3059 (1970). <https://doi.org/10.1139/p70-379>
- [30] J. Schmid et al., Phys. Rev. C 56, 2565 (1997). <https://doi.org/10.1103/PhysRevC.56.2565>
- [31] L. Ma et al., Phys. Rev. C 55, 588 (1997). <https://doi.org/10.1103/PhysRevC.55.588>
- [32] C. Casella et al., Nucl. Phys. A 706, 203 (2002). [https://doi.org/10.1016/S0375-9474\(02\)00749-2](https://doi.org/10.1016/S0375-9474(02)00749-2)
- [33] C. Angulo et al., Nucl. Phys. A 656, 3 (1999). [https://doi.org/10.1016/S0375-9474\(99\)00030-5](https://doi.org/10.1016/S0375-9474(99)00030-5)

- [34] Y. Xu et al., Nucl. Phys. A 918, 61 (2013). <https://doi.org/10.1016/j.nuclphysa.2013.09.007>
- [35] V. M. Bystritsky et al., Nucl. Inst. Meth. A 595, 543 (2008). <https://doi.org/10.1016/j.nima.2008.07.152>
- [36] E. G. Adelberger et al., Rev. Mod. Phys 83, 195 (2011). <https://doi.org/10.1103/RevModPhys.83.195>
- [37] P. Descouvemont et al., At. Data Nucl. Data Tab. 88, 203 (2004). <https://doi.org/10.1016/j.adt.2004.08.001>
- [38] L. E. Marcucci et al., Phys. Rev. Lett. 116, 102501 (2016). <https://doi.org/10.1103/PhysRevLett.116.102501>
- [39] Mossa, V., Stöckel, K., Cavanna, F. et al., The baryon density of the universe from an improved rate of deuterium burning. Nature 587, 210–213 (2020). <https://doi.org/10.1038/s41586-020-2878-4>
- [40] S. Turkat, S. Hammer, E. Masha, et al., Measurement of the  $^2\text{H}(\text{p}, \gamma)^3\text{He}$  S factor at 265–1094 keV (2021). <https://doi.org/10.1103/PhysRevC.103.045805>
- [41] M. Grieger, Full Background Characterization of Felsenkeller Underground Laboratory (2020). <https://doi.org/10.1088/1742-6596/1468/1/012246>
- [42] D.K. Haines, T.M. Semkow, A.J. Khan et al., Muon and neutron-induced background in gamma-ray spectrometry <https://doi.org/10.1016/j.nima.2011.01.137>
- [43] A. Anttila et al., Use of the  $^{27}\text{Al}(\text{p}, \gamma)^{28}\text{Si}$ ,  $E_p = 992$  keV resonance as gamma-ray intensity standard (1977). [https://doi.org/10.1016/0029-554X\(77\)90393-7](https://doi.org/10.1016/0029-554X(77)90393-7)
- [44] Gordon R. Gilmore, Practical Gamma-ray Spectrometry – 2nd Edition, Chapter 4, page 108.
- [45] W. Assmann, H. Huber, Ch. Steinhausen et al., Elastic recoil detection analysis with heavy ions (1994). [https://doi.org/10.1016/0168-583X\(94\)95159-4](https://doi.org/10.1016/0168-583X(94)95159-4)
- [46] K. Stockel, N. Mozumdar, S. Zavatarelli et al., A novel approach to measure the  $\text{D}(\text{p}, \gamma)^3\text{He}$  differential cross section: Experimental results and comparison with theoretical calculations (2023). <https://doi.org/10.1088/0004-637X/708/1/796>
- [47] A. Lemut, The definition of the effective interaction energy for astrophysical relevant reactions (2008). <https://doi.org/10.1140/epja/i2008-10585-6>
- [48] I. Tisma et al., Astrophysical S-factor for the  $^2\text{H}(\text{p}, \gamma)^3\text{He}$  reaction at big bang nucleosynthesis energies (2020). <https://doi.org/10.1051/epjconf/202022702015>